UC Berkeley
UC Berkeley Electronic Theses and Dissertations

Title

Investigating the Spectroscopic Properties of Lead-Halide Perovskite Nanocrystals for Advancements in Solid-State Laser Cooling

Permalink

https://escholarship.org/uc/item/3qr63464

Author

Abbas, Abdullah Saud

Publication Date

2024

Peer reviewed|Thesis/dissertation

eScholarship.org Powered by the California Digital Library
University of California

Investigating the Spectroscopic Properties of Lead-Halide Perovskite Nanocrystals for Advancements in Solid-State Laser Cooling

By

Abdullah S. Abbas

A dissertation submitted in partial satisfaction of the

requirements for the degree of

Doctor of Philosophy

in

Engineering – Materials Science and Engineering

in the

Graduate Division

of the

University of California, Berkeley

Committee in charge:

Professor A. Paul Alivisatos, Chair
Professor Peidong Yang
Professor James Analytis

Spring 2024

Investigating the Spectroscopic Properties of Lead-Halide Perovskite Nanocrystals for Advancements in Solid-State Laser Cooling

Copyright 2024
By
Abdullah S. Abbas

Abstract

Investigating the Spectroscopic Properties of Lead-Halide Perovskite Nanocrystals for

Advancements in Solid-State Laser Cooling

By

Abdullah S. Abbas

Doctor of Philosophy in Engineering – Materials Science and Engineering

University of California, Berkeley

Professor A. Paul Alivisatos, Chair

This dissertation will delve into the concept laser cooling in solid-state semiconductors, showcasing a remarkable application of photonics operating at the thermodynamic limits. Originally conceptualized by Pringsheim in 1929, laser cooling has attracted significant attention ever since. While its success has been demonstrated in atomic systems, enabling groundbreaking insights into quantum mechanics, it was not until 1995 that the first successful of solid-state laser cooling was realized in rare-earth-based materials. This achievement paved the way to explore a broader range of solid-state materials. In solid-state laser cooling, the process involves the absorption of sub-bandgap photons, coupled with the absorption of phonon energy, to excite a valence electron to the conduction band. An anti-Stokes photoluminescence (ASPL) emission is followed sequentially, which completes the cycle of phonon annihilation. This cycle leads to a reduction in the material's temperature. Despite extensive research, confirmed instances of laser cooling in semiconductor materials remain elusive.

Here, our exploration will begin with a thorough examination of semiconductor nanomaterial candidates. Among extensively researched nanomaterials, lead-halide perovskite nanocrystals in particular exhibit exceptional optoelectronic properties owing to their efficient up-conversion and near-unity photoluminescence quantum yield, both essential factors for realizing laser cooling, positioning them as a prime material for advancing the field of solid-state laser cooling.

The investigation will start with examination of the sequential processes crucial for solid-state laser cooling. Initially, the up-conversion efficiency will be quantified, followed by a comprehensive comparative analysis of different halide perovskite nanocrystals. Then rigorous investigations of phonon modes in pure and mixed halides will be followed to reveal the dynamics in steady-state and excited states. After up-conversion efficiency quantification and electron-phonon dynamics investigation, we will study the quantum confinement effect on the radiative lifetimes in perovskite nanocrystals. The ASPL process relies on the emission of photons upon exciton radiative recombination. Thus, it is essential to shorten the radiative lifetime to reduce the likelihood of non-radiative pathways, which results in undesired heating.

After demonstrating the promising potential of lead-halide perovskite nanocrystals for solid-state laser cooling applications, we will conduct experimental laser cool trials. We will develop a special setup that will directly and precisely measure any temperature changes. The setup will incorporate a highly sensitive infrared camera, enabling direct monitoring of temperature variations upon photoexcitation of the nanocrystals with sub-bandgap photons. We then will document our laser cooling attempts and analyze the outcomes. This analysis will include a comparison of different sample preparation methods and their impact on achieve a net laser cooling. Through this comprehensive thesis, we aim to contribute invaluable insights into the practical realization of laser cooling using lead-halide perovskite nanocrystals.

Acknowledgements

I would like to first thank my immediate family for supporting me throughout my doctoral journey. Specifically, I want to thank you mother for her constant presence, prayers, and pride in me through both the challenging and easy times. I am grateful to my late father who instilled in me the values of dedication, hardworking, honesty and good moral from my earliest years. Many thanks to my oldest sister, Dr. Abbas, who opened my eyes to the world of nanotechnology, which was the main reason I chose to pursue my undergraduate career in nanotechnology engineering and later my master and PhD in materials science and engineering with focus on nanomaterials. I want to thank my two older brothers for tirelessly taking care of the family while I am studying abroad. I also want to thank my second oldest sister for her constant words of encouragement and for her belief in me. And I want to thank my two younger sisters who look up to me with admirations, which was a constant source of motivation.

I would like to give special thanks to Negest Williams for her selfless support during my turbulent move to Berkeley and during my time in Berkeley and before my move to Chicago. I will always be grateful to my advisor, Paul Alivisatos, for welcoming me into his research group. His constant and insightful guidance and advice has been effective in shaping me to become a great scientist. I would like to thank my lab mates and friends Priscilla Pieters and Rafaela Brinn for our great subgroup meetings and for making working in the lab fun. I would like to thank Vida Jamali for her help with the publication of my first authored paper. I would also like to thank Alondra Perez who I took classes and worked on assignments with. I would like to thank Anthony Salazar for discussing department exams including prelim and qualification exams. I would also like to thank Ariana Castro for her kind support and guidance whenever I needed assistance with my department requirements.

Since our Berkeley lab moved from UCBerkeley to UChicago, it was quite the change. I would like to thank Kamran Forghani for his help in arranging my move and making my transition smooth. As rebuilding the lab takes time and my research direction shifted, it took a toll on me, but I resisted and believed it all happened for a reason. I built great connections at UChicago. So, I would like to thank my great collaborators who contributed to the success of some my projects. First, I would like to thank Richard Schaller and Beiye (Coco) Li for their effort in conducting time-resolved measurements and helping with laser cooling experiments at Argonne National Lab. I would like to thank Karen M. Watters for her help with scientific editing of the submitted manuscript (chapter 2). I would also like to thank Daniel Chabeda for his work on the radiative lifetime project. I also would like to thank my mentee, Daqian (Dylan) Bian, who will carry on my ongoing projects as I transition to my next endeavour.

Moving to Chicago was intimidating at first as most of my out-of-school connections were based in the bay area. Luckily, I have met great friends in Chicago who made me like the city more than I expected. Specifically, I would like to express my gratitude to Jennifer Tello who made exploring Chicago joyful. I would also like thank my friend, Lucas Zeer, who I have had countless calls with to talk about life and future plans. I would also like to thank my undergraduate friend group, known as The Buffalos. And I would like to thank my four close cousins who would always wait for me to visit back home so we can catch up. I would also like to thank my uncle and aunts from my mother side for keeping in contact with me and for always praying for me.

I would like to thank the Saudi ministry of education, Saudi Arabian cultural mission (SACM), and King Abdulaziz City for Science and Technology (KACST) for the funding they have provided. I would like to specifically thank prince Turki Bin Saud Bin Mohammed Al Saud for his help in conveying my message to the Saudi ministry of education in 2018 to accept the Materials Science and Engineering – Doctoral program as a desirable field of study at UCBerkeley.

Words certainly are not enough to express my gratitude to all the aforementioned people. Specially for my family and close friends, I will always be grateful for their love and support for what I do in life.

Contents

Contents iii
List of Figures v
List of Tables viii
Chapter 1. Introduction 1
1.1 Motivation 3
1.2 Current State of the Art 3
1.2.1 Rare-earth Solids 3
1.2.2 Semiconductors Solids 4
1.2.2.1 Bulk Semiconductors 4
1.2.2.2 Colloidal Nanocrystals and Nanostructures 5
1.3 Lead-Halide Perovskite Nanocrystals 7
1.3.1 Defects in Perovskite Nanocrystals 8
1.4 Experimental Methods 10
1.4.1 Chemicals 10
1.4.2 Synthesis 10
1.4.3 Critical Quantum Yield 10
1.4.4 Measurement Techniques 11
1.4.4.1 Photoluminescence Quantum Yield (PLQY) 11
1.4.4.2 Laser Cooling Apparatus 11
1.5 Thesis Organization 12
Chapter 2. Efficient Up-Conversion in $CsPbBr_3$ Nanocrystals via Phonon-Driven Exciton-Polaron Formation 14
2.1 Introduction 14
2.2 Results & Discussion 15
2.2.1 Steady-State Dynamics 15
2.2.2 Excited State Dynamics 19
2.3 Conclusion 23
Chapter 3. Phonon-Driven Up-Conversion Dynamics in Pure Halide Perovskite Nanocrystals 24
3.1 Introduction 24
3.2 Results & Discussion 26
3.2.1 Steady-State Characterizations 26
3.2.2 Phonon-Driven Up-Conversion in $CsPbX_3$ Nanocrystals 27

3.2.3 Transient Absorption (TA) and Pump Fluence Dependence 29
3.2.4 Excited States Dynamics in Pure Halide Perovskite Nanocrystals 29
3.3 Conclusion 32
Chapter 4. Phonon-Driven Up-Conversion Dynamics in Mixed Halide Perovskite Nanocrystals 34
4.1 Introduction 34
4.2 Results & Discussion 35
4.3 Conclusion 39
Chapter 5. Non-Monotonic Size-Dependent Exciton Radiative Lifetime in CsPbBr3 Nanocrystals 41
5.1 Introduction 41
5.2 Results & Discussion 42
5.3 Conclusion 49
Chapter 6. Can Semiconductor Nanocrystals Be Laser Cooled? 51
6.1 Introduction 51
6.2 Results & Discussion 53
6.3 Conclusion & Future Recommendations 67
Appendix A 68
A.1 Urbach Energy 68
A.2 Temperature Dependency of Up-Conversion Efficiency 68
Appendix B 76
B.1 Up-Conversion Efficiency Analysis 76
B.2 Urbach Energy 76
Appendix C 84
C.1 Up-Conversion Efficiency Analysis 84
C.2 Urbach Energy 84
Appendix D 93
References 98

List of Figures

Figure 1.1: Doppler cooling mechanism. 1
Figure 1.2: Phonon annihilation through anti-stock luminescence. 2
Figure 1.3: Potential applications to utilize laser cooling. 3
Figure 1.4: Laser cooling in rare-earth materials. 4
Figure 1.5. Bulk semiconductor. 5
Figure 1.6. Laser cooling measurement on CdS nanobelts. 6
Figure 1.8. Colloidal perovskite nanocrystals[15]. 8
Figure 1.9. Defects in perovskite nanocrystals[18]. 9
Figure 1.10. Perovskites surface etching[22]. 9
Figure 1.11: Direct laser cooling measurement setup. 12
Scheme 2.1: Energy band diagram of $CsPbBr_3$ nanocrystals[26] illustrating the up-conversion process and anti-Stokes photoluminescence (ASPL). 14
Figure 2.1: Optical and structural characterizations of $CsPbBr_3$ nanocrystals. 16
Figure 2.2: Below gap photoexcitation of $CsPbBr_3$ nanocrystals. 17
Figure 2.3: Steady-state time-resolved PL for above- and below-gap excitations. 19
Figure 2.4: Transient absorption (TA) versus excitation power at two different timescales reveals linear and superlinear regimes. 20
Figure 2.5: a, d, Time-resolved TA spectral map 21
Figure 2.6: Beating frequency in $CsPbBr_3$ nanocrystals. 23
Scheme 3.1: Molecular picture of energy levels illustrating the up-conversion process and anti-Stokes photoluminescence (ASPL) in perovskite nanocrystals. 24
Figure 3.1: Steady-state characterizations of pure-halide perovskite nanocrystals. 27
Figure 3.2: Up-conversion efficiency and phonon identification. 28
Figure 3.3: Transient absorption (TA) and pump fluence dependence. 29
Figure 3.4: Above gap excitation time-resolved transient absorption (TA) measurement. 30
Figure 3.5: Below gap excitation time-resolved transient absorption (TA) measurement. 32
Figure 3.6: Beatmaps analysis. 32
Figure 4.1: Steady-state characterizations of mixed halide perovskite nanocrystals. 36
Figure 4.2: Up-conversion efficiency in mixed halide perovskites. 37
Figure 4.3: Non-monotonic up-conversion process in mixed halide perovskites. 38
Figure 4.4: Size-dependent up-conversion efficiency in mixed halide perovskites. 39
Figure 5.1: Optical and structural characterizations of $CsPbBr_3$ nanocrystals with varying sizes. 43
Figure 5.2: Time-resolved photoluminescence (TRPL) characterization. 44
Figure 5.3: Size-dependent exciton radiative lifetimes and rates of $CsPbBr_3$ nanocrystals. 45
Figure 5.4: X-ray diffraction (XRD) and molecular dynamics (MD) of varying $CsPbBr_3$ nanocrystal sizes. 47
Figure 5.5: Size-dependent radiative lifetimes calculation. 49
Figure 6.1: Direct laser cooling measurement setup. 53
Figure 6.2: Optical and structural characterizations of $CsPbBr_3$ nanocrystals. 54
Figure 6.3: Laser cooling measurement with thermal camera and 532 nm sub-bandgap laser. 55
Figure 6.4: Pure toluene solvent. 56
Figure 6.5: An encapsulated thin film. 56

Figure 6.6: Bare coverslip. 57
Figure 6.7: Nanocrystals thin film sandwiched by two glass coverslips. 58
Figure 6.8: Polystyrene film. 59
Figure 6.9: Polymer-nanocrystals matrix film. 60
Figure 6.10: Sub-bandgap excitation over time. 61
Figure 6.11: Laser cooling measurement with thermal camera and 520 nm sub-bandgap diode laser. 62
Figure 6.12: Bare aerogel film for laser cooling measurement. 63
Figure 6.13: Nanocrystals in aerogel film. 64
Figure 6.14: Laser cooling measurements in cryostat using coverslip. 65
Figure 6.15: Laser cooling measurements in cryostat using thin glass cuvette. 65
Figure A1: Anti-Stokes laser excitations with a 515 nm long pass filter. 70
Figure A2: Raman spectroscopy. 71
Figure A3: Comparative Analysis of Up-Conversion Efficiency at Room Temperature (RT) and Liquid Nitrogen (LN) Temperature. 72
Figure A4: The up-conversion efficiency 73
Figure A5: Low power below gap transient absorption. 74
Figure A6: Illustration of decay traces that exhibit overlapping behavior in the long-time limit, both for resonant and non-resonant excitations. 74
Figure A7: Time traces taken from 75
Figure B1: Absolute Photoluminescence Quantum Yield (PLQY). 77
Figure B2: Transmission Electron Microscopy (TEM) images. 78
Figure B3: X-Ray Diffraction (XRD) Patterns. 78
Figure B4: Below gap photoexcitation of $CsPbCl_3$ nanocrystals. 79
Figure B5: Below gap photoexcitation of $CsPbBr_3$ nanocrystals. 80
Figure B6: Below gap photoexcitation of $CsPbI_3$ nanocrystals. 81
Figure B7: Raman spectroscopy. 82
Figure B8: Beating frequency. 83
Figure B9: Long-time limit transient absorption (TA) bleach decays under above and below gap excitation. 83
Figure C1: Elemental analysis. 85
Figure C2: X-Ray Diffraction (XRD) Patterns. 85
Figure C3: Absolute Photoluminescence Quantum Yield (PLQY). 86
Figure C4: Above and below gap photoluminescence emission and excitation scans. 86
Figure C5: Below gap photoexcitation of $CsPbCl_{0.75}Br_{2.25}$ nanocrystals. 87
Figure C6: Below gap photoexcitation of $CsPbI_{0.75}Br_{2.25}$ nanocrystals. 88
Figure C7: Below gap photoexcitation of $CsPbBr_{0.75}I_{2.25}$ nanocrystals. 89
Figure C8: Below gap photoexcitation of strongly confined $CsPbI_{0.75}Br_{2.25}$ nanocrystals. 90
Figure C9: Below gap photoexcitation of intermediately confined $CsPbI_{0.75}Br_{2.25}$ nanocrystals. 91
Figure C10: $CsPbI_{0.75}Br_{2.25}$ nanocrystals with varying sizes. 91
Figure D1: Transmission electron microscopy (TEM) characterization of $CsPbBr_3$ nanocrystals. 93
Figure D2: Time-resolved photoluminescence (TRPL) characterization. 93
Figure D3: Size-dependent radiative lifetimes and rates of $CsPbBr_3$ nanocrystals. 94
Figure D4: Cubic vs orthorhombic $CsPbBr_3$ structure. 94
Figure D5: Order parameter. 95

Figure D6: Size Dependent Radiative Lifetime Across Different Temperatures.....96
Figure D7: Size-dependent radiative lifetimes calculation of wurtzite CdSe nanocrystals. 97
Figure D8: Size-dependent radiative lifetimes calculation of zincblende InP nanocrystals. 97

List of Tables

Table 1.1: Critical quantum yield[5].....11
Table 6.1: Summary of laser cooling measurements on perovskite nanocrystals with photoluminescence emission of 509 nm and photoluminescence quantum yield of ~100%. 65

Chapter 1. Introduction

Since it was proposed in 1929 by Pringsheim[1], optical refrigeration, also known as laser cooling, has drawn significant attention due to its advantages and cost effectiveness over traditional mechanical refrigeration. Initial work since the proposal was focused on cooling atoms in gaseous phase in which radiation pressure from light could reduce the translational motion of the gases causing their temperature to drop[2,3]. This type of cooling gases is known as Doppler cooling in which randomly moving atoms in the gas phase is exposed to off-resonance radiations from all directions (Figure 1.1a). When a moving atom encounter a photon travelling in the opposite direction, the photon undergoes a wavelength shortening due to Doppler effect and becomes in resonance with atom's absorption transition energy. (Figure 1.1b). The atom then emits the photon in a random direction, thus, reducing its average velocity which in turns reduces its temperature.

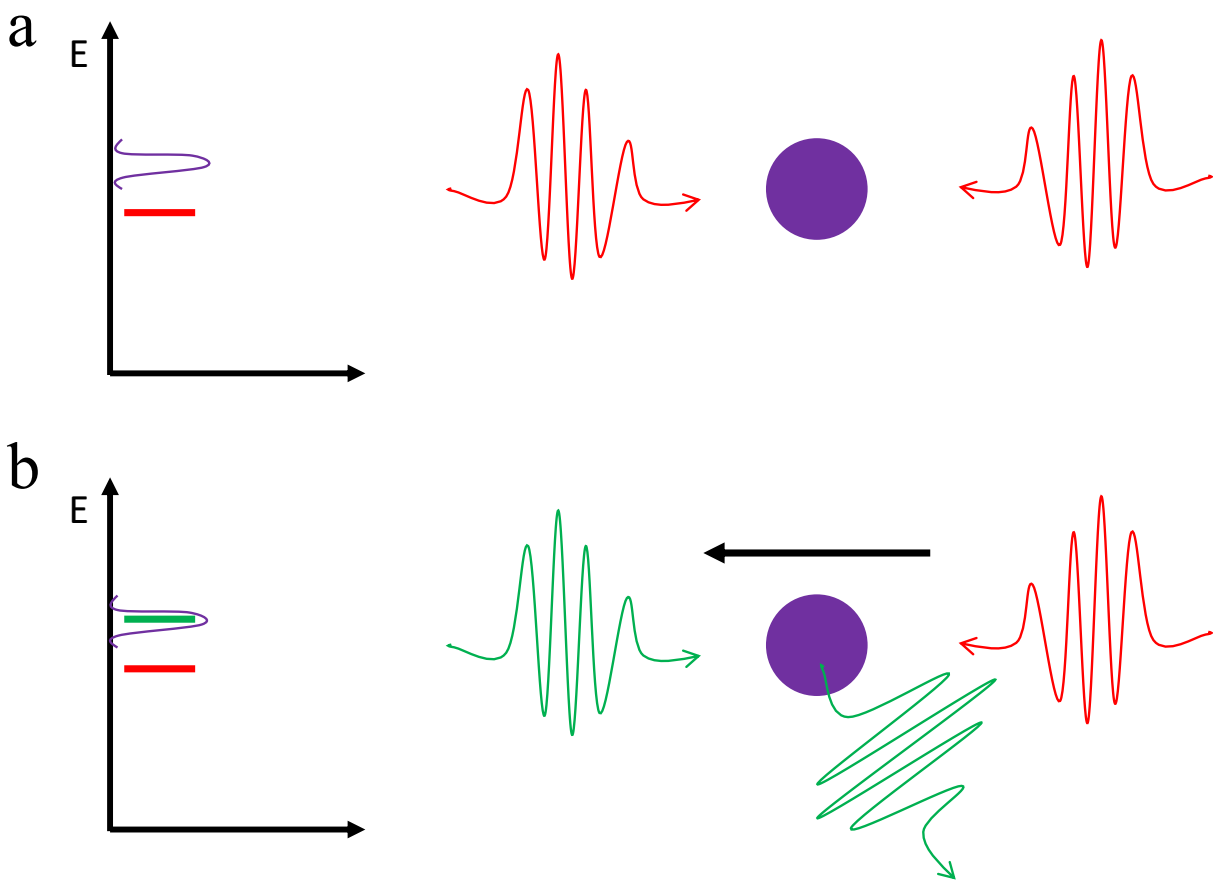


Figure 1.1: Doppler cooling mechanism. Doppler cooling mechanism where an atom in gas phase with a specific transition state is exposed to (a) off-resonance radiations from all directions, and (b) when the atom moves and meets a photon that is moving in the opposite direction, it appears of in-resonance due to Doppler effect and an absorption occurs. Upon photon emission from the atom in a random direction, the atom average velocity is reduced, thus reducing its temperature.

Although Doppler cooling has enabled numerous quantum mechanical investigations, it is limited to moving atoms in gaseous phase and does not allow its integration, for instance, into optoelectronic devices.

Another cooling mechanism that allows solid-state materials to be cooled is through the annihilation of lattice vibrations, also known as phonon, through anti-stock luminescence[4,5]. The mechanism simply relies on laser excitation of an electron with sub-bandgap photon to a shallow defect state, then the electron absorbs phonon from the materials to transition to the minimum of the conduction band. Once the electron is at the minimum of the conduction band, a radiative decay to the maximum of the valence band will produce photon with higher energy (i.e. anti-stock luminescence) that is the sum of the sub-bandgap photon and phonon, thus annihilating the lattice vibration and reducing the temperature of the material. Figure 1.2 illustrates the anti-stock processes. One must note that it is possible for the electron to thermally decay to the trap state and either gets excited back to the minimum of the conduction band through phonon absorption, or decay non-radiatively causing heat emission, which is undesirable. This radiative and non-radiative competition is the bottleneck for observing net cooling in solid-state semiconductor materials and significant work has been done to prevent non-radiative processes through chemical and engineering techniques as well be discussed in the coming sections. It is worth noting that this schematic in Figure 1.2 is simplified and not accurate; more accurate schematic and description of the up-conversion processes are described in later chapters.

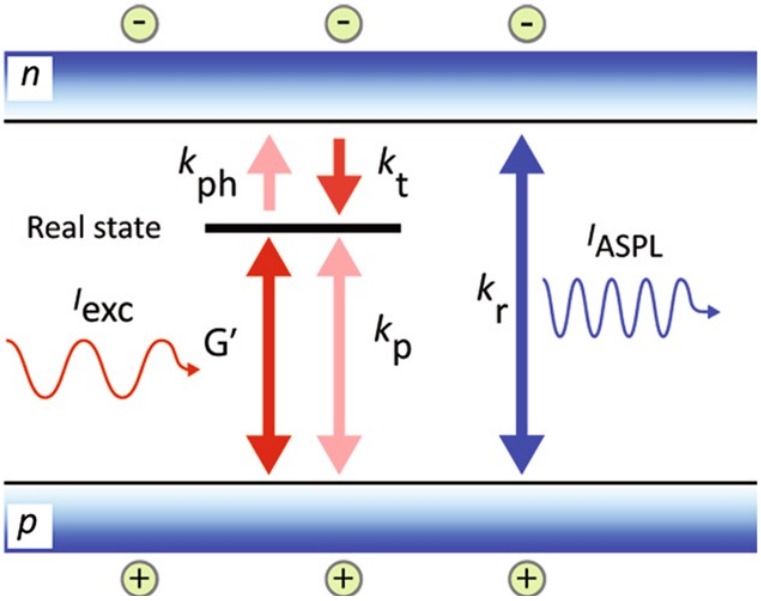


Figure 1.2: Phonon annihilation through anti-stock luminescence. An electron absorbs sub-bandgap photon and transitions to a shallow trap state, then an extra absorption of phonon kicks the electron to the minimum of the conduction band where the electron can radiatively recombine and produce anti-stock emission with energy that is the sum of the absorbed photon and phonon, thus removing some lattice vibration and thus reducing the temperature. Possible non-radiative route is through the re-trapping of the electron back to the defect state and then down to the maximum of the valence band with a decay rate, k_r.

1.1 Motivation

Although other techniques for cooling already exists, such as mechanical refrigerator and thermoelectric cryostat, they are either difficult to integrate into other devices or limited to how cold of temperature they can reach. Solid state optical refrigeration overcomes both challenges by their ability to cool below 100 K and can be processed and integrated with other devices. Some current and potential applications of optical refrigeration is shown in Figure 1.3. Figure 1.3a illustrates a quantum material in which each energy level is very temperature sensitive; thus, a constant temperature, usually very low temperature, is needed[6]. Figure 1.3b shows a high-power laser that generate excessive heat, and when coupled with materials that can laser cool, it potentially can have no internal heating[7]. Thus, it is very imperative to always ensure a constant temperature for these applications, and that's where optical refrigeration can play a major role.

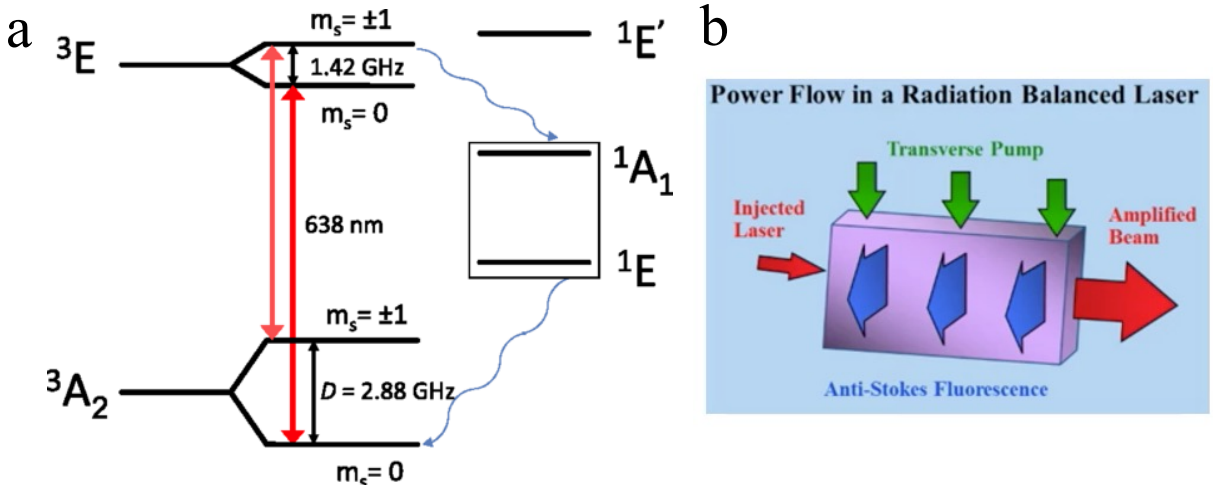


Figure 1.3: Potential applications to utilize laser cooling. (a) Temperature sensitive energy levels schematic of the nitrogen vacancy center[6]. (b) High-power laser internal cooling[7].

1.2 Current State of the Art

1.2.1 Rare-earth Solids

All solid-state materials for laser cooling has been sought for several years since the proposal of reducing the temperature through anti-stock emission in 1929, and not until 1995, Epstein and co-workers has demonstrated the first solid state laser cooling with rare-earth solid, namely Yb^{3+} dopants in a fluorozirconate glass (ZBLANP:Yb^{3+})[8]. Since then, successful solid state laser cooling was achieved as shown in Figure 1.4a[5], and a different system was developed made of Yb^{3+}-doped yttrium lithium fluoride (YLF) crystals that ultimately allowed reaching a cryogenic temperature of 89 K in 2013 (Figure 1.4b)[9]. This 89 K is essentially the minimum achievable temperature (MAT) for rare-earth doped materials, and this limit stems from the fact that the rare-earth element's electron populations at the top of the ground state follows Boltzmann statistics and decreases drastically when temperature is below 100 K[10]. Therefore, considerable attention has been shifted to semiconductors since their electronic population in the valence band remains populated even at absolute zero, as semiconductors follow Fermi-Dirac statistics[10].

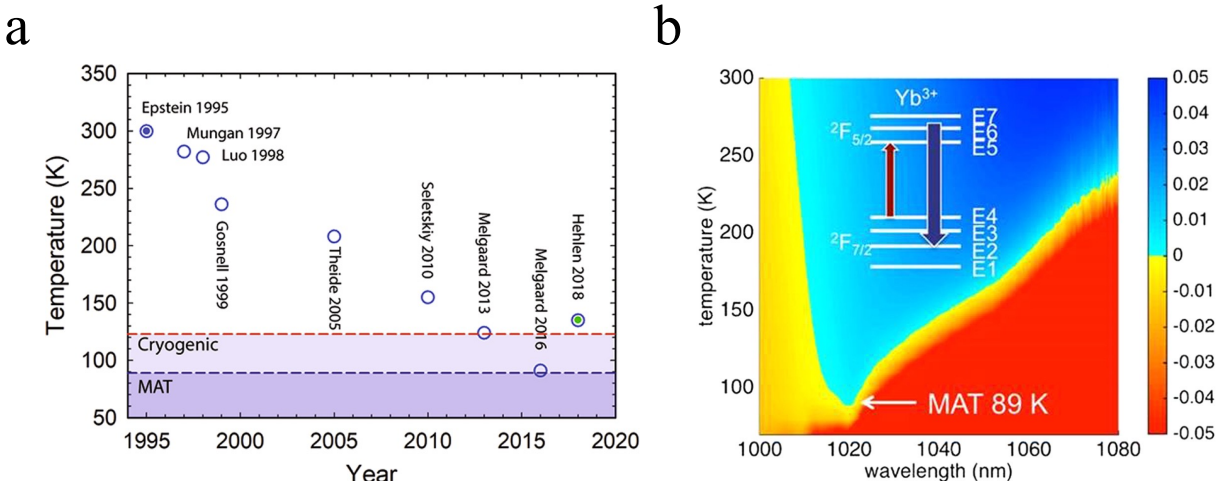


Figure 1.4: Laser cooling in rare-earth materials. (a) Rare-earth doped glass/crystal laser cooling milestone[5]. (b) Cooling efficiency contour map where cooling and heating are indicated by the blue and red regions, respectively. The 89 K temperature signify the minimum achievable temperature (MAT)[9].

1.2.2 Semiconductors Solids

Despite rare-earth solids reaching cryogenic temperature, their MAT as well as their complicated processing to integrate them to potential optoelectronic devices make them not ideal. Semiconductors, on the other hand, is known to reach temperatures of ~10 K or below[10], and they can easily be integrated into optoelectronic devices. Also, semiconductor solids have large absorption coefficient, making them ideal for the phonon annihilation through anti-stock luminescence[11].

1.2.2.1 Bulk Semiconductors

Initial work on semiconductors to realize laser cooling was done on bulk GaAs[12,13]. To observe net cooling, the non-radiative pathways must be suppressed to prevent any undesirable heating. GaAs thin film tend to suffer from low overall internal quantum yield (IQY) due to the presence of surface recombination[5]. Significant optimizations were done to remove any surface recombination sites through different growth and surface chemical treatment, and that helped improve the quantum efficiency to 96%[12]. Another issue of GaAs is the large refractive index that if interfaced with air, emitted photons can be trapped and can't easily be extracted; thus, refractive index matching, and structure engineering is required. Figure 1.5a shows the GaAs in an LED structure in which a layer of GaInP is added to form a heterostructure with GaAs to help with refractive index matching, and a ZnSe hemisphere is added to assist in light extraction. Despite all the surface treatment and refractive index matching, no net cooling was observed for GaAs thin film[12]. Additional work that followed where the quantum efficiency was improved to 99.5% after further optimization of the structure, but as shown in Figure 1.5b, no net cooling was observed, and it was concluded that the reason behind that could be due to some parasitic sub-bandgap absorption that led to heating[5,13].

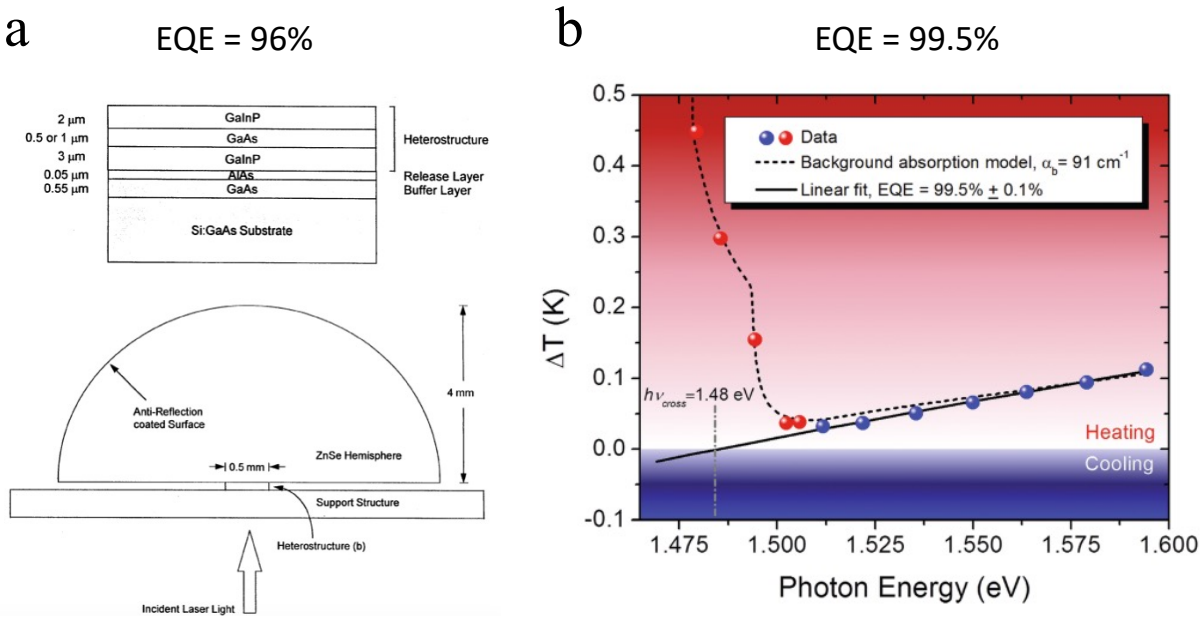


Figure 1.5. Bulk semiconductor. (a) Schematic of index matching layers for GaAs and the hemisphere that is added to help extract light[12]. (b) Optical scanning calorimetry measurement done at 100 K for GaAs/GaInP double heterostructure showing no net cooling for various excitation wavelengths[13].

1.2.2.2 Colloidal Nanocrystals and Nanostructures

To avoid the need for refractive index matching as well as complicated structure engineering, colloidal nanocrystals and nanostructures possess superior quantum efficiency, ease of synthesis, and due to their small size, photons can easily escape. An example of a semiconductor nanomaterial that has shown a net cooling is the CdS nanobelts[4]. Key characteristics of CdS nanobelts that make them a good candidate for laser cooling are: "low carrier mobilities, low associated surface recombination velocities, smaller Auger coefficient, and strong exciton–LOP coupling"[4,5]. Figure 1.6a and b show temperature change over time when the sample initially started at 290 K and 100 K, respectively. The sample was excited with sub-bandgap and over-bandgap. Figure 1.6a shows net cooling when the sample is excited with sub-bandgap laser, especially the 514 nm excitation source. When the sample is started at 100 K, the 514 nm excitation became off-resonance with the sub-bandgap state and resulted in net heating instead (Figure 1.6b). Additionally, the excitation laser power needs to be low to avoid: (1) two-photon absorption that would bypass the needed phonon absorption, and (2) the non-radiative auger recombination. Figure 1.6c shows the power dependence anti-stock emission at 290 K where we can see two regime: first linear region indicating single photon absorption, and second region adopts a power-law behaviour indicating two-photon-absorption-induced emission[4]. Overall, Figure 1.6 shows net cooling of $\Delta T = 40$ K for CdS nanobelts[4].

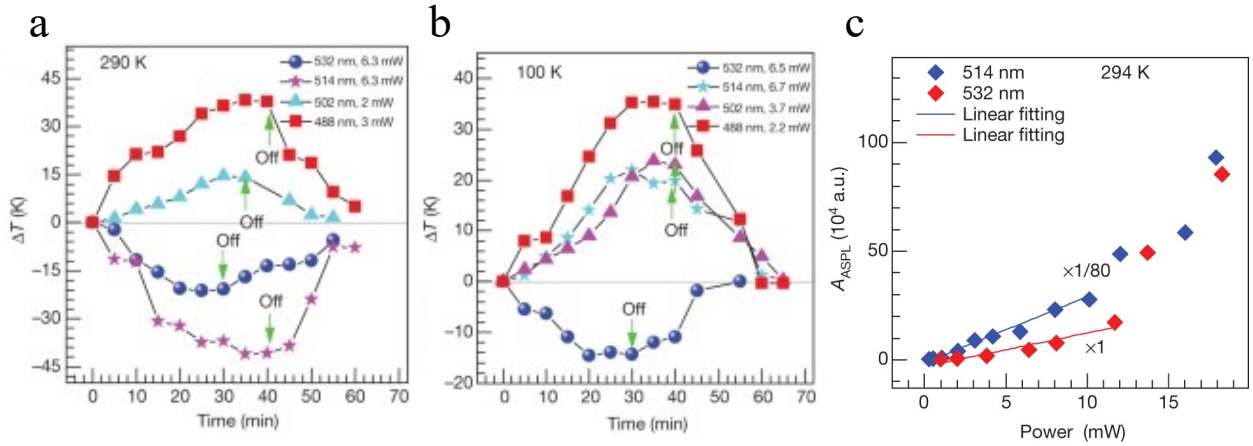


Figure 1.6. Laser cooling measurement on CdS nanobelts. Temperature change over time under off-resonance excitations when the sample is at (a) 290 K and (b) 100 K[4]. Power dependence of the anti-stock emission for off-resonance excitation showing linear regime for low power and power-law behavior at higher power[4].

Other semiconductor nanomaterials that have showed net cooling are 2D and 3D organic-based perovskite platelets. With similar experimental setup as the CdS nanobelts, Figure 1.7 shows the temperature change over time when the samples are under off-resonance excitation (both sub- and over-bandgap)[11]. Figure 1.7a shows the 3D perovskite showing a net cooling of 23 K when excited with about 10-15 nm off-resonance, while Figure 1.7b shows the 2D perovskite showing a net cooling of 58.7 K when excited with 15 to 35 nm off-resonance[11].

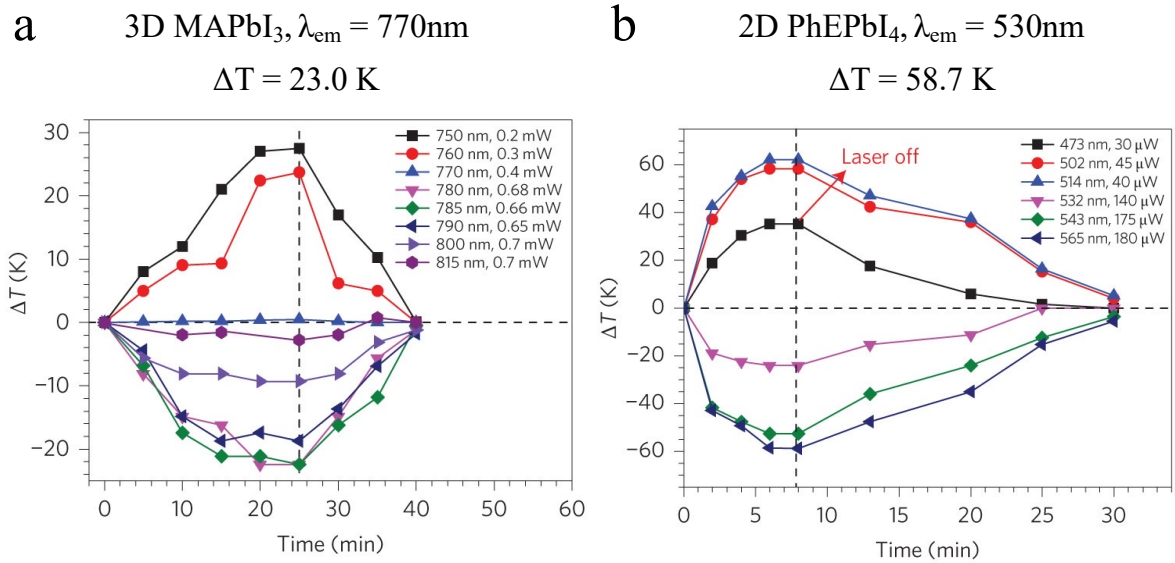


Figure 1.7. Laser cooling measurement on perovskites. Temperature change over time for (a) 3D $MAPbI_3$ with emission peak at 770nm (b) and 2D $PhEPbI_4$ with emission peak at 530nm, excited with off-resonance and net cooling was observe for only sub-bandgap excitations.

Even though the previous two semiconductor nanomaterial examples showed net cooling, a debate is still ongoing on whether the measurements of the temperature changes were done correctly. The CdS nanobelts and the perovskite platelets samples showed net cooling and heating within minutes

timeframe while the expected rates, which was also computationally confirmed, are within milliseconds[5,14]. This discrepancy certainly has caused a confusion whether it is possible to observe net cooling in semiconductor nanomaterials; nonetheless, it has made the community more intrigued to work toward observing net cooling in semiconductors.

1.3 Lead-Halide Perovskite Nanocrystals

All inorganic cubic perovskite nanocrystals with the formula of ABX_3, where A is typically Cesium, B is a metal such as Lead and X for halide ions (Figure 1.8a), was first made in colloidal form in 2015, and has drawn significant attention ever since due to its ease of synthesis, narrow emission, and high as-synthesized photoluminescence quantum yield (PLQY), along with the ability to tune the bandgap through composition engineering (Figure 1.8b-d)[15]. The PLQY and lifetime of these colloidal nanocrystals are shown in Figure 1.8e, which are considerably remarkable considering them being as-synthesized without post-synthetic surface treatments[16]. Additionally, it has been shown that perovskite nanocrystals exhibit efficient up-conversion[5,17]. Therefore, perovskite nanocrystals have the potential for laser cooling application. However, due to the ionic nature of the crystal structure, perovskite suffers from stability against oxygen and moisture that tends to drastically decrease their PLQY. Aside from stability, perovskite nanocrystals tend to have surface defects, usually halide vacancy. The following section discusses the defects in lead-based perovskite nanocrystals.

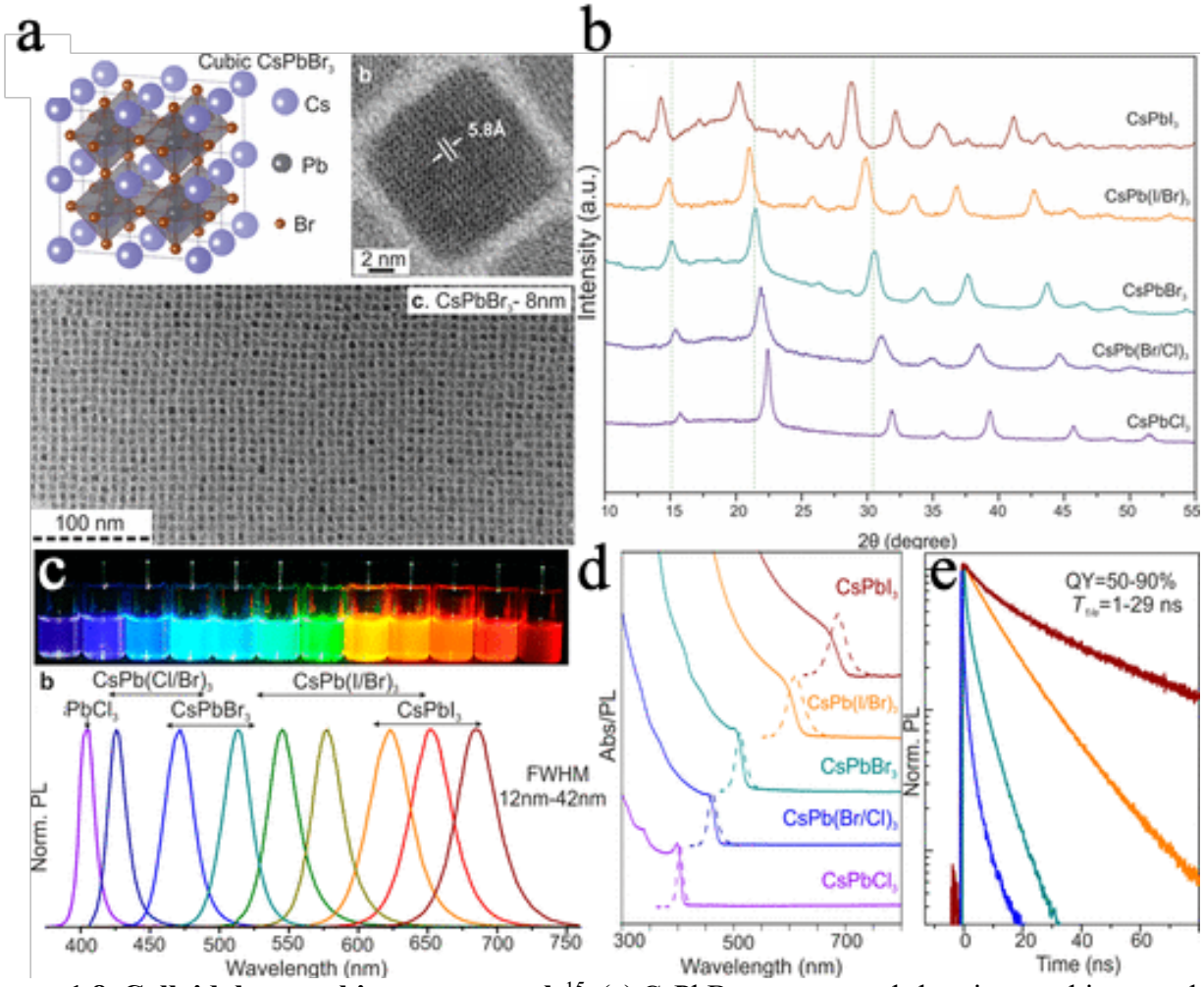


Figure 1.8. Colloidal perovskite nanocrystals[15]**.** (a) $CsPbBr_3$ nanocrystal showing a cubic crystal structure with a TEM image of one nanocrystal and a superlattice of cubes. (b-d) XRD, photoluminescence, and absorption overlapped with photoluminescence spectra of different halide compositions showing the bandgap tunability. (e) Time-resolved photoluminescence decay of perovskite nanocrystals with different compositions.

1.3.1 Defects in Perovskite Nanocrystals

These as-synthesized perovskite nanocrystals tend to have significant surface defects due to its ionic nature and small sizes[18]. Different perovskite composition tends to be more sensitive to the surface defects than the others. Figure 1.9a illustrates the effect of Cl^-, Br^-, and I^- halide vacancies on the quantum yield, where we can see the perovskite made with iodine is insensitive to the vacancy concentrations[18]. Also, from the Density Functional Theory (DFT) calculations in Figure 1.9b, we can see that the perovskite with I^- vacancy has a much shallower trap states, which could result in less trapping and reduce the non-radiative pathway. Additionally, we can see that the bandgap of the iodine based is much smaller, reducing the possible heat energy that could be produced in the case of an inevitable non-radiative recombination. Therefore, with the higher

tolerance to surface defects, the iodine-based perovskite seems to be a better candidate for laser cooling. However, iodine, due to its large ionic radius, tends to migrate and that could result in ionic defects that potentially could be detrimental[19], so a locking shell mechanism might be needed to avoid any ion migrations[20,21].

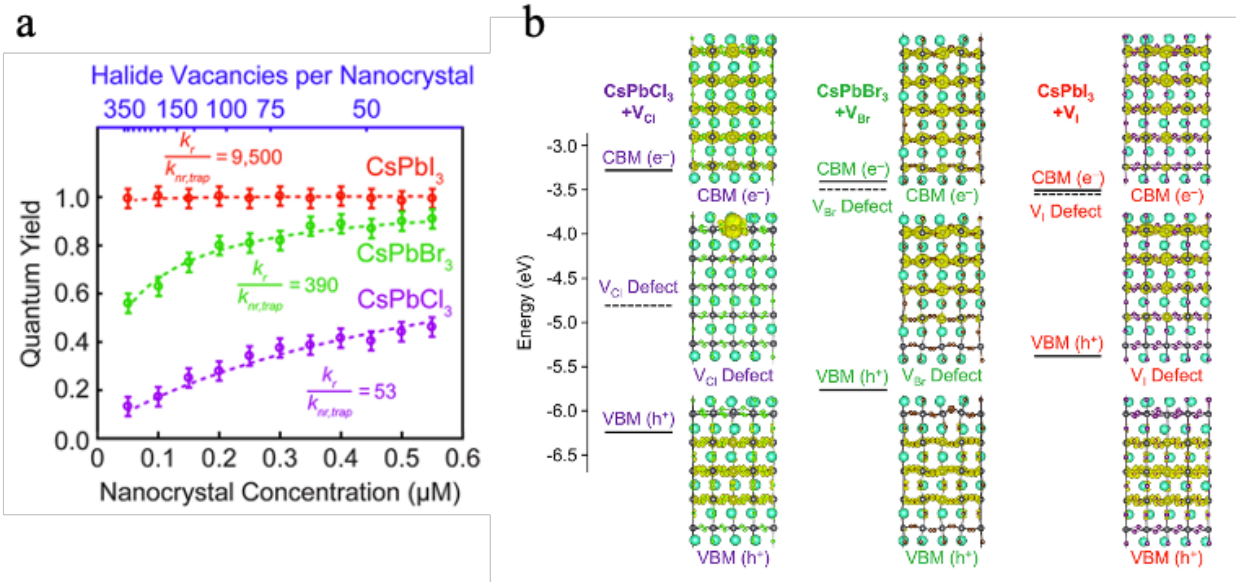


Figure 1.9. Defects in perovskite nanocrystals[18]. (a) Defect effects on the quantum yield for perovskite nanocrystals with different halide compositions. (b) Density functional theory (DFT) calculations for different halides vacancies showing their relative position within the bandgap.

Significant work has been done to prepare perovskite nanocrystals with near-unity PLQY. Since most of the defects in perovskite nanocrystal are surface defects, different surface treatments have been applied. An example of a surface treatment that showed significant improvement in PLQY is through chemically etching nanocrystal surface[22]. Figure 1.10a-b shows drastic improvement in PLQY and lifetime after etching the surface of the $CsPbBr_3$ with thiocyanate[22]. Figure 1.10c is a photothermal deflection spectroscopy (PDS) measurement, in which very shallow traps can be resolved, showing the elimination of the trap states after etching[22].

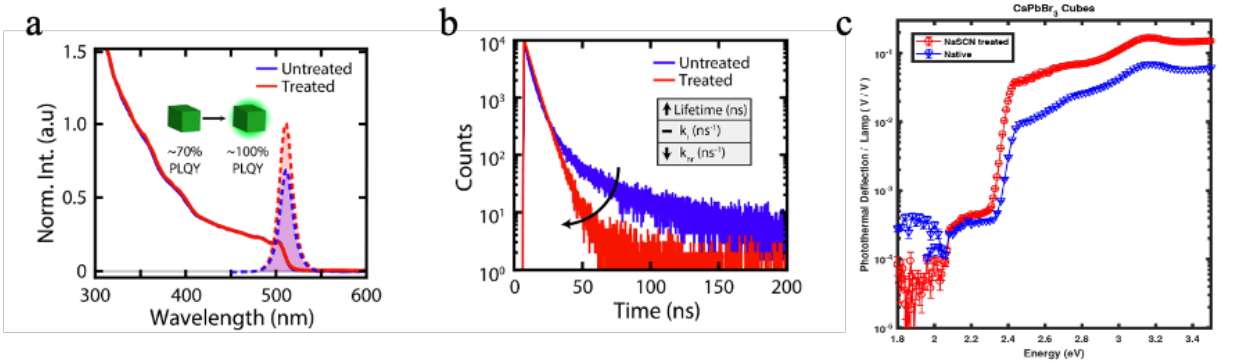


Figure 1.10. Perovskites surface etching[22]. Perovskite nanocrystals before and after chemical etching showing improvement in (a) emission and PLQY, (b) reduction in the non-radiative decay, and (c) the elimination of surface defects as shown in the PDS measurements.

Despite the great improvements with the chemical etching route, it requires a tedious and precise control over the etchant agents. Therefore, other approaches have been investigated to increase the halide content to reduce surface halide vacancies and ensure lead atoms are fully coordinated. The original colloidal synthesis of perovskite nanocrystals relies on using lead halide salts, such as $PbBr_2$, which makes it hard to increase only the halide content. One way is to decouple every element into their own source so that we can have a better control over the stoichiometric ratios. An experimental method has been developed where halide ions were introduced through benzoyl molecules (i.e., benzoyl halides)[23].

1.4 Experimental Methods

1.4.1 Chemicals

Lead (II) acetate trihydrate (PbOAc2•3H2O, 99.999%), oleylamine (OAm, 70%), 1-octadecene (ODE, 90%), and benzoyl bromide (BzBr, 97%) were purchased from Sigma-Aldrich. Cesium carbonate (Cs2CO3, 99.9%, Metal basis) and oleic acid (OA, 90%) were purchased from Thermo Scientific Chemicals. Other chemicals used include anhydrous toluene (99.8%) and hexane.

1.4.2 Synthesis

$CsPbBr_3$ nanocrystals were synthesized following a slightly modified version of previously published procedures[15,23]. Briefly, ODE (10 ml), oleic acid (0.6 ml), oleylamine (2 ml), $PbOAc_2$ (0.4 mmol) and Cs_2CO_3 (0.06 mmol) were loaded in a 50 ml round-bottom flask, degassed, and heated at 120 ^oC for 1 hr. Then, under nitrogen, the temperature was raised to 140 ^oC for 15 min followed by degassing at 120 ^oC for 10 min. The injection temperature was then set at 200 ^oC, under nitrogen, and BzBr (1.7 mmol) solution was injected swiftly. $CsPbBr_3$ nanocrystals formed almost instantly but were allowed to grow for 30-40 seconds before quenching in an ice-water bath. The nanocrystals were cleaned in an inert environment via successive precipitation at 10 k rpm without antisolvents and dissolution using toluene. Nanocrystals were stored in 5 ml toluene.

1.4.3 Critical Quantum Yield

To observe net cooling in solid state, the non-radiative pathways must be eliminated. These non-radiative pathways are usually a result of undesirable defects. A key parameter for assessing the quality of the material is through measuring the photoluminescence quantum yield (PLQY) coupled with lifetime measurements. PLQY is a measure of how much light is absorbed compared to how much is emitted, and we can relate it to the decay rates of both radiative and non-radiative as follow:

$$PLQY = \frac{Photon\ out}{Photon\ in} = \frac{k_r}{k_r + k_{nr}}$$

where k_r and k_{nr} are the radiative and non-radiative decay rate, respectively. With the competition between cooling and heating energies, a critical quantum yield exists in which a material must be equal to or be greater. This critical quantum yield relation is as follow:

$$QY_{crit} = \left(\frac{E_g - \Delta E}{E_g}\right)\left[\frac{\eta_{ASPL} + (1 - \eta_{ASPL})f}{\eta_{ASPL}}\right]$$

where E_g is the bandgap energy, ΔE is the detuning energy of the laser away from the resonance frequency, η_{ASPL} is the up-conversion efficiency, and f is the fraction of excitations that was not upconverted or recombined nonradiatively[5]. Table 1.1 below lists different semiconductor nanomaterials and their critical quantum yield with different laser detuning energy.

Table 1.1: Critical quantum yield[5]. Critical quantum yield for different nanocrystal systems under laser excitation detuned to 25 meV and 100 meV. The longitudinal optical phonon energy is shown to illustrate the relative energy that can be absorbed from the phonon for the up-conversion.

System	Diameter or edge length (nm)	E_g (eV)	$\hbar\omega_{LO}$ (meV)	QY_{crit} (%) ΔE = 25 meV = 1	QY_{crit} (%) ΔE = 100 meV = 1	Sizing, E_g, and $\hbar\omega_{LO}$ refs.
CdS NC	1.3–5.5	4.74–2.81	37.8	99.5–99.1	97.9–96.4	32,125
CdSe NC	1.0–8.5	3.57–1.91	26.3	99.3–98.7	97.2–94.8	32,125
CdTe NC	3.5–9.0	2.15–1.67	20.8	98.8–98.5	95.3–94.0	32,125
PbS NC	4.0–8.5	1.23–0.67	25.4	98.0–96.3	91.9–85.1	32,126
PbSe NC	3.0–5.5	1.26–0.73	16.5	98.0–96.6	92.1–86.3	32,127
$CsPbBr_3$ NC	4.0–12.5	2.70–2.41	20.5	99.1–99.0	96.3–96.0	128,129
$CsPbI_3$ NC	3.4–12.5	2.13–1.85	NA	98.8–98.6	95.3–94.6	130

1.4.4 Measurement Techniques

1.4.4.1 Photoluminescence Quantum Yield (PLQY)

One of the earlier common PLQY measuring methods is the relative quantum yield measurement by which an organic dye with a known quantum yield is compared against a sample with unknown quantum yield[24]. Although the relative quantum yield measurement is easily done, there are many ways of introducing human errors, for example, inconsistent concentrations and contamination in the organic dye.

Another common method is the integrated sphere, in which the sample is placed in a non-absorbing sphere that also scatters light in random direction and has an exit coupled to a fiber optic to the detector. The photon counts that were was absorbed by the sample solution is compared with the reference solvent. Even though the integrated sphere method is more accurate than the relative quantum yield measurement, it introduces, on average, and error of about 2%, which is acceptable for most applications, but not for laser cooling[25]. As shown in Table 1, being off from near-unity by 2% puts the quantum yield well below the critical quantum yield[25].

1.4.4.2 Laser Cooling Apparatus

To avoid relying on any indirect measurements of temperature change such as through the use of thermocouple or Raman signal shifts, we set up an apparatus that can detect a change in temperature directly in a contactless manner. Sample is placed in a thermally insulating cuvette or film and a sensitive infrared (thermal) camera is placed in close proximity to detect any change in temperature within ± 0.1 ℃. Figure 1.11 shows the setup.

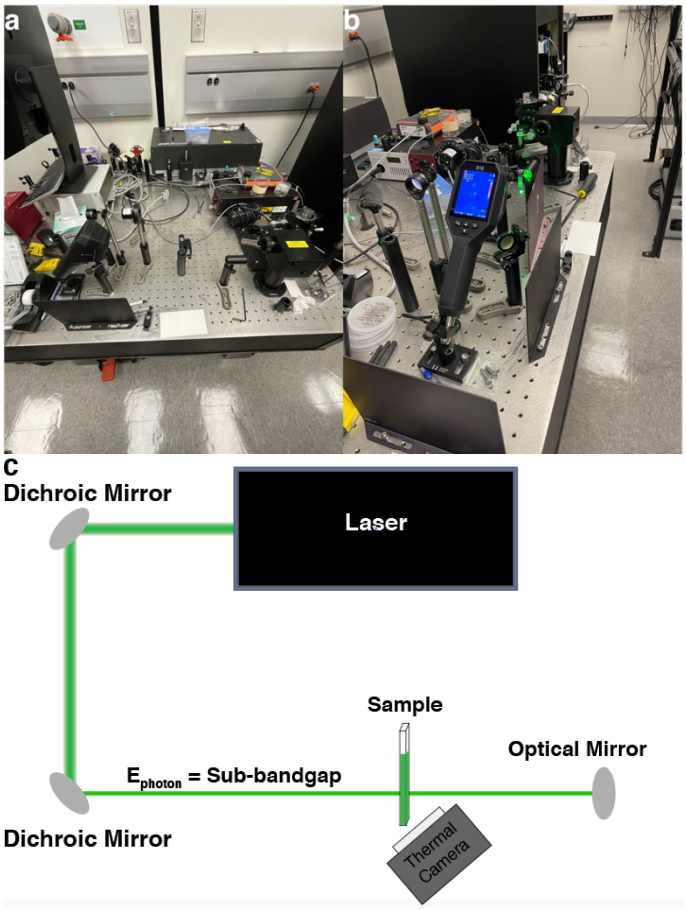


Figure 1.11: Direct laser cooling measurement setup. (a) Front and (b) side views of the optical table where the laser cooling measurements are conducted. (c) Schematic showing the laser path to the sample that is also getting back reflected by an optical mirror along with a sensitive thermal camera in close proximity to the sample to detect any temperature change.

1.5 Thesis Organization

This thesis uses a systematic approach at tackling a multidecade problem regarding laser cooling in solid-state semiconductor materials. This work seeks to fill a gap in knowledge relating essential sequential processes to observing net laser cooling, specifically, in nanocrystals, commonly known as quantum dots. These sequential processes involve phonon-driven up-conversion of valence electrons followed by anti-Stokes photoluminescence (ASPL). The ASPL has a radiative lifetime and is an important parameter. We use size-dependent quantum confinement effect to tune the radiative lifetimes. We couple the up-to-date advances with the work addressed in the chapters of this thesis to attempt laser cooling in nanocrystals.

In chapter 2, we will discuss the efficient up-conversion in $CsPbBr_3$ perovskite nanocrystals, investigate the responsible phonon modes, and study the electron-phonon coupling. We will deploy steady-state and time-resolved techniques to quantify the up-conversion efficiency as well as extract the phonon mode.

In chapter 3, we extend the work in chapter 2 to encompass other pure halide perovskites, namely, $CsPbCl_3$ and $CsPbI_3$ perovskite nanocrystals. Along quantifying the up-conversion efficiency, we will extract the different phonon modes for each halide system.

In chapter 4, we further study the effect of mixing halides on the up-conversion efficiency and quantify the phonon energies coupled to the up-conversion process.

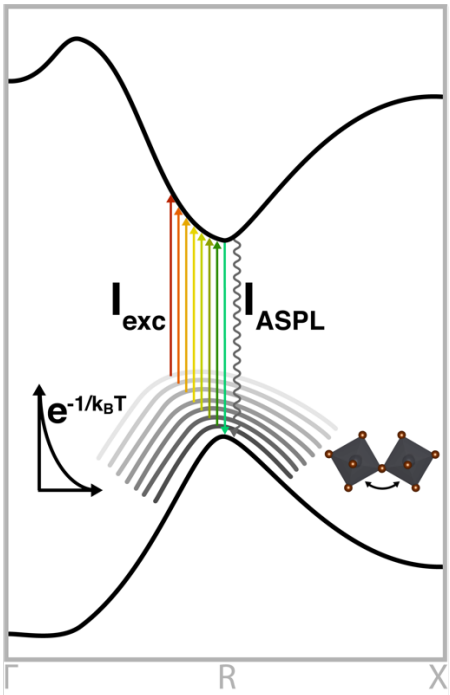
In chapter 5, we rigorously study the effect of nanocrystal size on radiative lifetime. We utilize steady-state, time-resolved, molecular dynamics, and electronic structure calculations to understand the origin of size-dependent radiative lifetime in perovskite nanocrystals. We will showcase this size-dependent radiative lifetime to occur in other common nanocrystals system, such as III-V (e.g. indium phosphide, InP) and II-VI (e.g. cadmium selenide, CdSe) nanocrystals.

Finally, in chapter 6, we will report attempts at laser cooling perovskite nanocrystals with a new measurement setup. We will also provide insight on future work.

Chapter 2. Efficient Up-Conversion in $CsPbBr_3$ Nanocrystals via Phonon-Driven Exciton-Polaron Formation

2.1 Introduction

Lead halide perovskite nanocrystals have emerged as a highly promising semiconducting nanomaterial for phonon-driven up-conversion, owing to their ease of synthesis and near-unity photoluminescence quantum yield (PLQY) [5,15,17,18,22]. In phonon-driven up-conversion, a phonon is annihilated upon sub-bandgap light absorption to arrive at an excited state population followed by anti-Stokes photoluminescence (ASPL), where the emitted photon energy is higher than that of the excitation photon (Scheme 2.1). Once an electron undergoes up-conversion to arrive at the conduction band edge, radiative emission without generation of a phonon leads to an overall reduction in phonon population, while non-radiative recombination results in phonon generation.



Scheme 2.1: Energy band diagram of $CsPbBr_3$ nanocrystals[26] illustrating the up-conversion process and anti-Stokes photoluminescence (ASPL). Electronic states form due to lattice vibrations and are thermally populated, for example with bending mode phonons[27]. Sub-bandgap phonon-assisted light absorption promotes a valence electron to the conduction band and subsequent ASPL decreases the phonon population.

Among promising semiconducting nanomaterials candidates for up-conversion[5], cesium lead tribromide ($CsPbBr_3$) perovskite nanocrystals exhibit substantial up-conversion

efficiencies[5,15,17], as well as a remarkably low trap density and high tolerance for shallow surface defects, which contribute to their near-unity PLQY[19,28,29]. On an ensemble and single-particle level, $CsPbBr_3$ nanocrystals can up-convert with efficiencies up to 75% when the excitation source is detuned below the gap by 23 meV[17]. However, the phonon-assisted up-conversion process is particularly delicate and complex because more vibrational degrees of freedom create a larger hot thermal population to excite, but these same degrees of freedom tend to abrogate photoluminescence in favor of non-radiative relaxation. Additionally, coherent phonon oscillations have been directly observed in layered perovskites[30,31], and a recent report on quasi-two-dimensional perovskites showed that the coherent oscillations are involved in the up-conversion process of carriers[32].

Here, we deploy a combination of steady-state and excited-state measurements to resolve the specific phonons involved in the efficient up-conversion process within $CsPbBr_3$ nanocrystals, determine up-conversion efficiency at different detuning energies, and investigate how electron-phonon coupling changes in nanocrystals undergoing up-conversion. Using a tunable laser, we leverage the exponential relationship between the excitation wavelengths and the ratio of laser intensity to ASPL intensity to extract the phonon energy related to the up-conversion process. We identify the Pb-Br-Pb bending mode, with energy ~ 7 meV[27,33–35], as the phonon involved in up-conversion within $CsPbBr_3$ nanocrystals. In excited-state measurements, the above-gap excitation results in the expected intraband cooling characteristics. However, with below-gap excitation, an unexpected coherent phonon oscillations emerges at early times as exciton-polarons form within the subset of nanocrystals undergoing up-conversion. These coherent lattice vibrations are synchronized to the frequency of the Pb-Br-Pb bending phonon mode, which implies that the up-conversion and subsequent relaxation is accompanied by a synchronized and phased lattice motion. In all, this work provides invaluable insight into how the intricate interplay between the soft lattice structure, phonons, and excited states dynamics contributes to efficient up-conversion in $CsPbBr_3$ nanocrystals.

2.2 Results & Discussion

2.2.1 Steady-State Dynamics

We first set out to identify the specific phonon modes involved in up-conversion in $CsPbBr_3$ nanocrystals. We use high-quality nanocrystals to avoid non-radiative pathways that might otherwise obscure the sub-bandgap dynamics involved in the up-conversion process[36]. $CsPbBr_3$ nanocrystals were synthesized following a modified version of previous reports[15,23]. Figure 2.1a shows the steady-state absorption and photoluminescence (PL) spectra with band edge emission peak at ~ 2.435 eV and a full width at half maximum (FWHM) of 81.38 meV. The as-synthesized (no-post synthetic treatment) $CsPbBr_3$ nanocrystals exhibit very high absolute PLQY, approaching ~100% unity within 2.0% uncertainty, as shown in Figure 2.1b. This near-unity PLQY, an attribute of lead-halide perovskite nanocrystals[18,22,37], highlights their suitability for our study. The nanocrystals are highly monodispersed, Figure 2.1c, which is also indicated by the narrow linewidth in the PL spectrum.

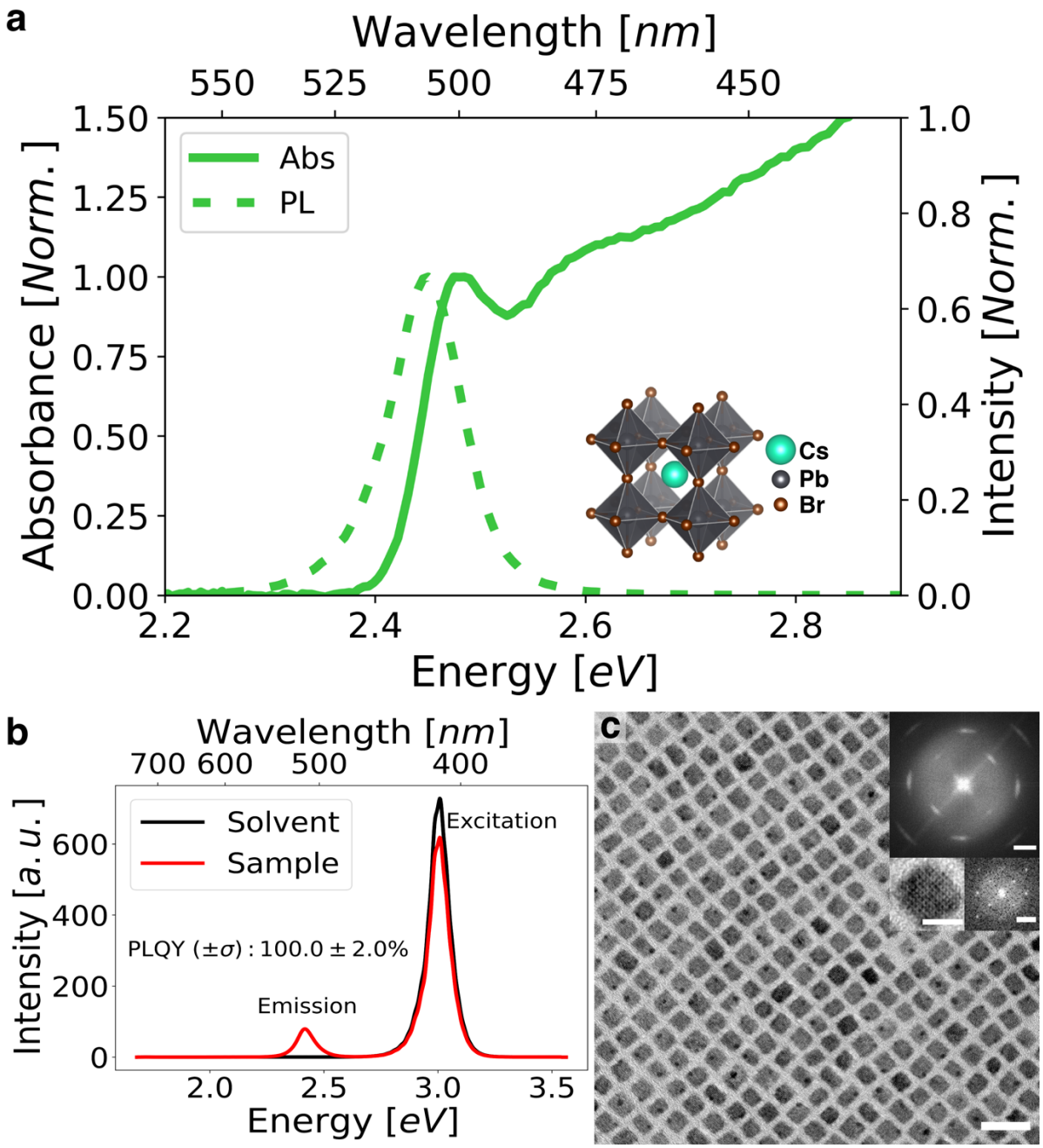


Figure 2.1: Optical and structural characterizations of $CsPbBr_3$ nanocrystals. a, steady-state absorption and photoluminescence (PL) spectra, with inset illustrating the crystal structure made with Vesta[38]. **b**, Near-unity photoluminescence quantum yield (PLQY) measurement. **c**, Transmission electron microscopy (TEM) image shows highly monodispersed nanocrystals and top inset shows the Fast Fourier Transform (FFT) (scale bars 20 nm and 1 nm^{-1}, respectively). Bottom insets show high-resolution TEM image of a single nanocrystal with FFT (scale bars 5 nm and 2 nm^{-1}, respectively).

We employed a tunable laser with a narrow bandwidth of 3 nm to photoexcite the high-quality nanocrystals below the band edge at different wavelengths. A long-pass filter with a wavelength of 515 nm was employed to prevent any unexpected broad bandwidth in the laser spectrum from

exciting the sample, as depicted in Figure A1. Figure 2.2a (and inset) shows the ASPL as a result of excitation below the band edge at room temperature over a wavelength range of 515 to 550 nm. The ASPL in $CsPbBr_3$ is expected[17], and we find that with increasing excitation wavelengths, the ratio of laser intensity to the ASPL intensity follows an exponential form (Figure 2.2b, see also log plot in the inset). We fit the data to an Arrhenius equation to extract a characteristic energy (E_{ch}) as follows:

$$\frac{I_{exc}}{I_{aspl}} \propto e^{-\left(\frac{E_g - h\nu}{E_{ch}}\right)}$$

where E_g is the bandgap energy, $h\nu$ is the excitation energy, and E_{ch} is a characteristic energy. This characteristic energy involves both $\kappa_B T$ at room temperature (RT) and the phonon energy (E_p) responsible for the up-conversion process. From the fit shown in Figure 2.2b, we retrieve $E_p = 7.28$ meV ($58.68\ \mathrm{cm}^{-1}$) which corresponds to the Pb-Br-Pb bending mode in $CsPbBr_3$ nanocrystals[34,39]. The presence of this low frequency is confirmed by Raman spectroscopy (peak $62.98\ \mathrm{cm}^{-1}$), as shown in Figure 2.2c (see Figure A2 for raw data and background fit). The lowest observed frequency ($25.42\ \mathrm{cm}^{-1}$) corresponds to the octahedral twist[40,41]. The 104.66 and $127.38\ \mathrm{cm}^{-1}$ frequencies are assigned to the longitudinal optical (LO) phonon modes associated with the stretching of the Pb-Br bonds in the $[PbX_3]^-$ sublattice, while the 309.88 and $317.62\ \mathrm{cm}^{-1}$ modes are assigned to higher order scattering based on previous reports[27,34,35,39].

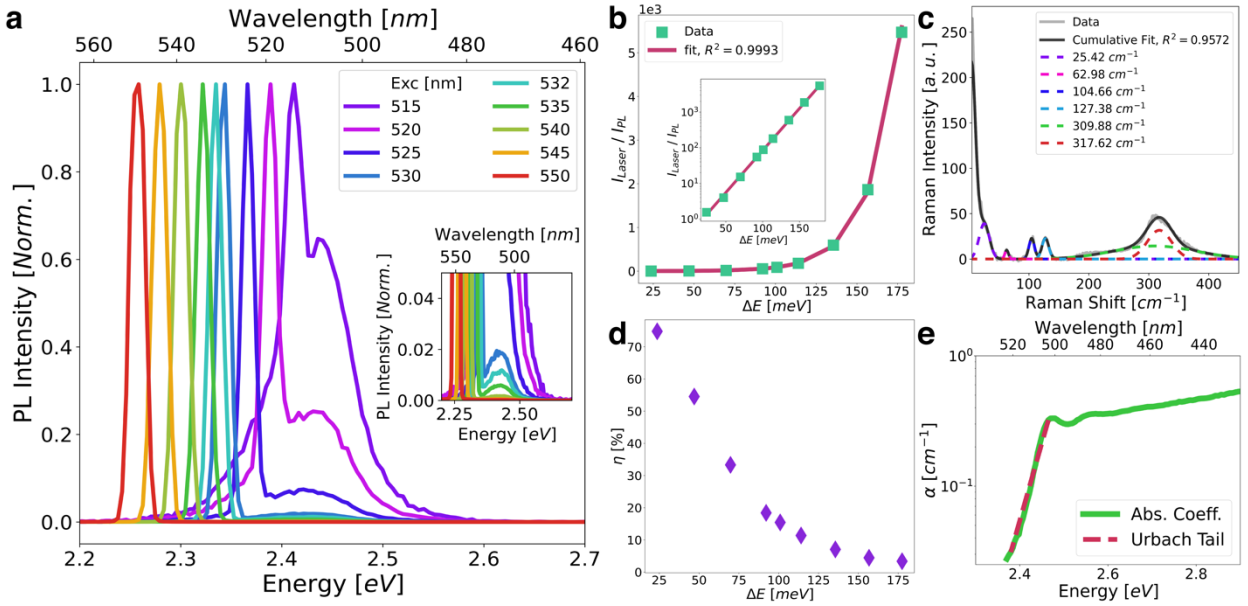


Figure 2.2: Below gap photoexcitation of $CsPbBr_3$ nanocrystals. a, Below gap photoexcitation shows distinct band edge emission characteristics. **b**, Analysis of the laser to PL intensity ratio reveals an exponential relationship. Inset, presented on a logarithmic scale, confirms a linear trend. **c**, Raman spectrum of $CsPbBr_3$ nanocrystals deposited as a thin film on a silicon substrate using drop-casting. Using a Lorentzian fit, the spectral data is reproduced, allowing identification of peaks linked to distinct vibrational modes within $CsPbBr_3$ nanocrystals. **d**, Quantification of up-conversion efficiency as a function of the detuning energy within the band gap. **e**, Absorption coefficient is fitted along the band tail to extract the Urbach energy, essential for anti-Stokes absorption calculations, detailed in Appendix A.

To quantify the up-conversion efficiency, the ASPL is compared to the Stokes PL which is the cap efficiency (i.e., all excitons excited above band gap that reached the band edge). Following the work of Zhang *et al*[5], the relation between Stokes PL, ASPL, and up-conversion efficiency (η) is formulated as follows:

$$I_{spl} = I_s\, A_s\, PLQY \tag{1}$$

$$I_{aspl} = I_{as}\, A_{as}\, \eta\, PLQY \tag{2}$$

where I_{spl} and I_{aspl} are the Stokes PL and ASPL intensities, $I_s$and I_{as} are the Stokes and anti-Stokes excitation intensities, A_s and A_{as} are the Stokes and anti-Stokes absorption, and η is the up-conversion efficiency. Measurement of the up-conversion efficiency (Figure 2.2a) is performed such that I_{spl} and I_{aspl} are similar in value. This allows us to re-arrange equation (1) and (2) to solve for η as follows:

$$\eta \approx \frac{I_s\, A_s}{I_{as}\, A_{as}} \tag{3}$$

Equation (3) requires A_{as} to be known for every excitation wavelength detuned into the $CsPbBr_3$ nanocrystals energy gap. Due to the low sensitivity of a typical spectrophotometer at the absorption band tail, we relied on the fact that absorption is related to the Urbach energy through the absorption coefficient. We fit the slope of the absorption coefficient from the band edge (Figure 2.2e, more details in Appendix A), extracted the Urbach energy, 30.95 meV, and calculated the absorption at the anti-Stokes position, A_{as}, at different excitation wavelengths. The Urbach energy of 30.95 meV falls within the lower range of typical Br vacancy levels, as theoretically calculated (within 100 meV), for Br-deficient $CsPbBr_3$ nanocrystals[18]. This observation is also consistent with other experimental findings, which have reported Urbach energy values ranging from 40 to 48 meV[42,43]. This suggests that our nanocrystals exhibit significantly reduced defect states. Using this Stokes and anti-Stokes data, we calculated the up-conversion efficiency for every excitation wavelength (Figure 2.2d). These measurements yielded values for η from 74.80% down to 3.38% for $\lambda_{exc} = 515$ nm ($\Delta E = 28.4$ meV) and $\lambda_{exc} = 550$ nm ($\Delta E = 181.6$ meV), respectively. Our results are in good agreement with previously reported values for $CsPbBr_3$ nanocrystals[17].

To further assess the role of phonons in the up-conversion process, we conducted a comparative analysis of up-conversion efficiency under two different temperature conditions: RT and liquid nitrogen (LN) temperature (~77 K). This analysis was performed on a freshly prepared sample with a PL emission peak at 2.4503 meV (as shown in Figure A3). In both cases, we observed that the ratio of laser intensity to ASPL intensity exhibited an exponential relationship. Based on this relationship, we determined the phonon energy associated with the up-conversion process as ~ 8 meV (corresponding to 64.712 cm^{-1}) at RT and 6 meV (corresponding to 48.17 cm^{-1}) at LN temperature. Notably, these phonon energies fall within the range of the Pb-Br-Pb bending mode[27,34,35,39].

We used the Urbach energy of the new sample, 24.655 meV, to calculate up-conversion efficiencies as above. As depicted in Figure A3f, our results clearly illustrate a significant reduction in up-conversion efficiency (~1.97-fold reduction on average) when the sample is cooled to cryogenic temperatures. Phonon population follows a Boltzmann distribution that is dependent on both energy and temperature factors. Therefore, we compared the ratio of the number of phonons (N_P) at RT and LN as follows:

$$\frac{N_P(RT)}{N_p(LN)} \propto \frac{e^{-\left(\frac{E_p(RT)}{\kappa_B T(RT)}\right)}}{e^{-\left(\frac{E_p(LN)}{\kappa_B T(LN)}\right)}}$$

yielding a value of 1.801. Remarkably, this value closely corresponds to the ratio of up-conversion efficiencies at the two temperature conditions (see Figure A3f inset). We also determined that room temperature falls within the optimal temperature range for maximizing up-conversion efficiency (depicted in Figure A4; detailed further in the Appendix A).

To further confirm that the ASPL is coming from the band edge emission, we measured steady-state time-resolved PL at RT for above- and below-gap excitations. Figure 2.3 illustrates that the decays follow a mono-exponential form with similar lifetimes. This result suggests that, regardless of whether the electron is excited above the band edge or up-converted to the band edge, decay originates from the band edge.

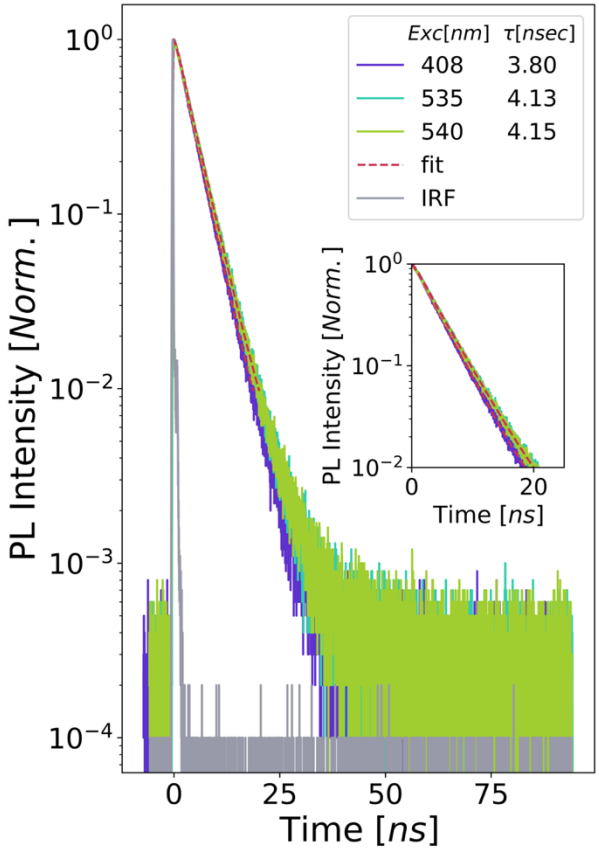


Figure 2.3: Steady-state time-resolved PL for above- and below-gap excitations. Both excitations exhibit closely matched mono-exponential decay patterns with comparable lifetimes.

2.2.2 Excited State Dynamics

To investigate how up-conversion affects electron-lattice vibration (electron-phonon coupling) in the nanocrystals, we next employed ultra-fast time-resolved spectroscopic measurements. We

performed transient absorption spectroscopy (TA) to elucidate the initial dynamics of excited states within the colloidal $CsPbBr_3$ nanocrystals with above- and below-gap excitation. Above-gap excitation was achieved by delivering 31.7 $[\frac{\mu J}{cm^2}]$ of pumping pulse power with 35 fs pulses centered at 440 nm. Since intense pumping below gap can electronically excite semiconductors via two-photon absorption, we first investigated the pump fluence dependence of our below-gap excitation (at 540 nm) and followed band edge bleach signals that corresponded to electron-hole pair excitation. As presented in Figure 2.4, a linear dependence on pump fluence clearly exists at 2 ps and 10 ps pump-probe time delays (both subsequent to typical carrier cooling timescales). We discern a linear scaling of bleach amplitude with pump power up to ~300 $[\frac{\mu J}{cm^2}]$. This linear regime indicates that signals below this power originate from a one-photon process consistent with up-conversion, helps us to avoid higher intensity regimes that would convolve up-conversion and two-photon pumping, and also allows us to judiciously select a power level that provides an optimal signal-to-noise ratio. Consequently, we set the below-gap pump power at 217.3 $[\frac{\mu J}{cm^2}]$ for this investigation (notably, Figure A5 also demonstrates similar effects with 163 $[\frac{\mu J}{cm^2}]$).

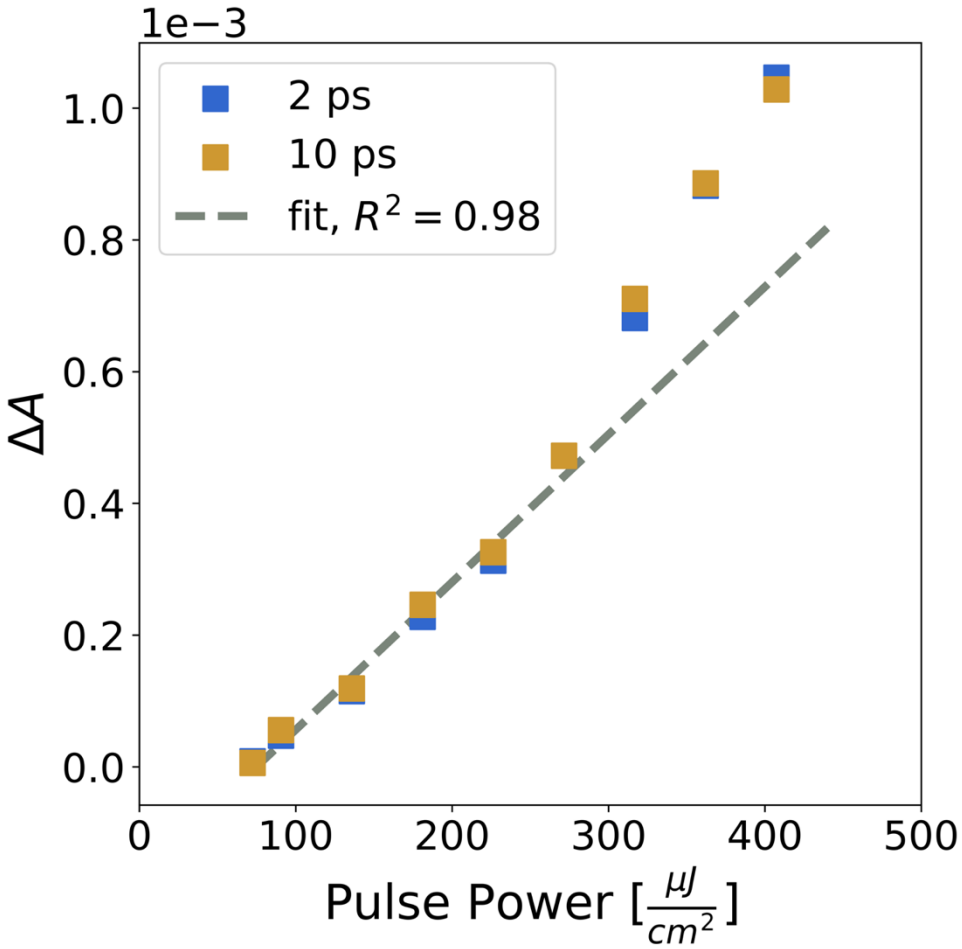


Figure 2.4: Transient absorption (TA) versus excitation power at two different timescales reveals linear and superlinear regimes. This allows to select an excitation power within the linear regime that is strong enough to yield a high signal-to-noise ratio.

For above-gap excitation (440 nm), the TA spectral map exhibits several distinct characteristics. Immediately following excitation, a pronounced induced absorption is observed near 512 nm that decays within 1 ps (Figure 2.5a, 2.5b). A band-edge bleach feature also appears and completes rising within this timeframe. The red-shifted induced absorption feature is conventionally linked to the presence and relaxation of a hot exciton state where intraband cooling of electron and holes to band-edge states occurs upon phonon generation[44,45]. Within the first 1 ps, the measurements reveal a slight red-shift (~1 nm) in the exciton transition, consistent with exciton-exciton Coulomb interactions[44,46]. It is worth noting that the cooling of a hot exciton sometimes results in the generation of coherent phonons if cooling is fast compared to the phonon period, which can induce oscillatory behavior in the TA signal. Under this excitation condition here, the composition does not exhibit such a phenomenon. Upon integrating the area under the TA curve versus pump-probe time delay (Figure 2.5b inset), a distinct plateau in the values becomes evident after 0.7 ps. This timescale aligns with polaron formation in $CsPbBr_3$ nanocrystals[27], which can also lead to induced absorption near 486 nm with a similar timescale[47] (Figure 2.5c).

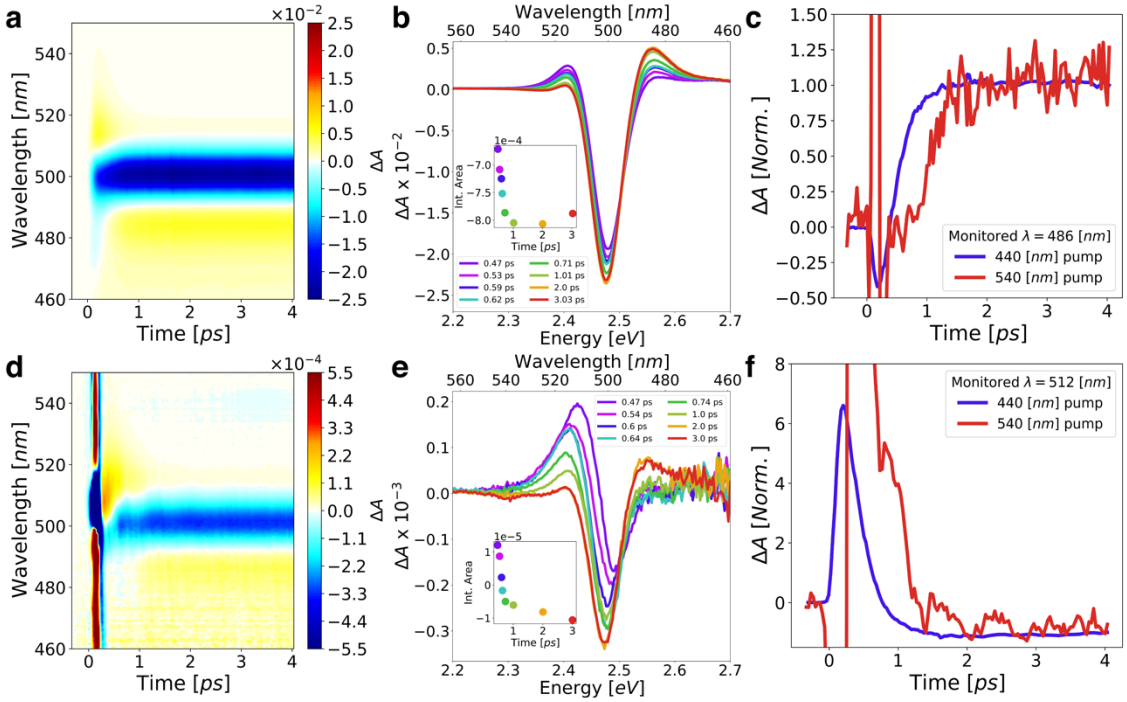


Figure 2.5: a, d, Time-resolved TA spectral map with (**a**) above-gap and (**d**) below-gap excitation (early time artifacts from excitation source)**. b**, **e**, Selected time-traces for (**b**) above-gap and (**e**) below-gap excitation. The behavior comparison between above- and below-gap excitations reveals interesting dynamics. In the case of below-gap excitation, an initial second-derivative pattern transitions into a symmetric pattern, differing from the above-gap excitation case. Notably, within the first picosecond, the integrated area for the below-gap excitation shows a zero crossing. **c**, **f**, Wavelengths (**c**) above and (**f**) below the ground-state bleach are tracked over time and normalized at the final picosecond (due to the convergence of both excitations, also shown in Figure A6). A distinct delay in the (**c**) rise and (**f**) decay of the below-gap excitation becomes evident.

For below-gap excitation (540 nm) conducted in the linear regime, distinct features appear in the TA spectra. Notwithstanding the coherent signal near time zero, a photoinduced absorption signal again emerges near 512 nm upon excitation (Figure 2.5d, 2.5e) and decays on a similar timescale to the above-gap condition. Note, however, that the 512 nm induced absorption signal nominally should not appear owing to an absence of hot excitons and band-edge bleach formation should approach the instrument response function, as intraband relaxation does not occur under this condition. Time-resolved spectra also appear appreciably distinct, which we elaborate on below. Remarkably, we also observe oscillatory spectral signals emerging below the band edge in the TA spectrum in Figure 2.5d (along the border of ground-state bleach and the photoinduced absorption), where the oscillation frequency can be quantified by performing fast Fourier transform (FFT) along the time axis. We obtained a characteristic frequency value of approximately 50 cm^{-1} (illustrated in Figure 2.6a), which corresponds to the frequency of the Pb-Br-Pb bending phonon mode. The observation of coherent phonons in this scenario implies phonons are involved in the ultrafast up-conversion and relaxation processes, which may seem counterintuitive since below-gap excitation conditions generate neither a hot electron nor a hot hole and presumably remove phonons from any excited nanocrystal. Thus, nanocrystals undergoing up-conversion contain a quantum of the specific phonon that impulsively gets removed upon absorption, and the observed oscillation reveals a dominant relaxation mechanism on the path to polaron formation. This outcome reinforces the assertion that the efficient up-conversion in $CsPbBr_3$ nanocrystals is associated with the Pb-Br-Pb bending mode, as visually represented in Figure 2.6b.

The distinctive line shapes observed in the below-gap excitation TA spectra (Figure 2.5d) are also worth discussing. During the initial period (<1 ps), the TA spectra exhibit characteristics of a second derivative, which subsequently transform into a symmetric above-gap-excitation-like pattern. It is important to highlight that, unlike typical above-gap excitation scenarios, the integrated area of the TA curves crosses zero as time advances. This intriguing observation suggests that the polaron generated during the early stages plays a crucial role in facilitating electron-phonon coupling for up-conversion by inducing charge redistribution and lattice distortion due to the soft lattice of $CsPbBr_3$[27,48]. The charge redistribution is marked by the noticeable red-shift (~3 nm) in the TA spectra, which can be attributed to the intricate interplay of many-body Coulomb interactions[27]. This transition in line shape occurs within a short interval of 0.7 ps, which serves as additional confirmation of the critical involvement of polarons in the up-conversion process[27]. We also observe a noticeable delay in the rise and decay of the time traces when monitoring below the band edge, as opposed to above the gap, for both above- and below-gap excitations (Figure 2.5c, 2.5f).

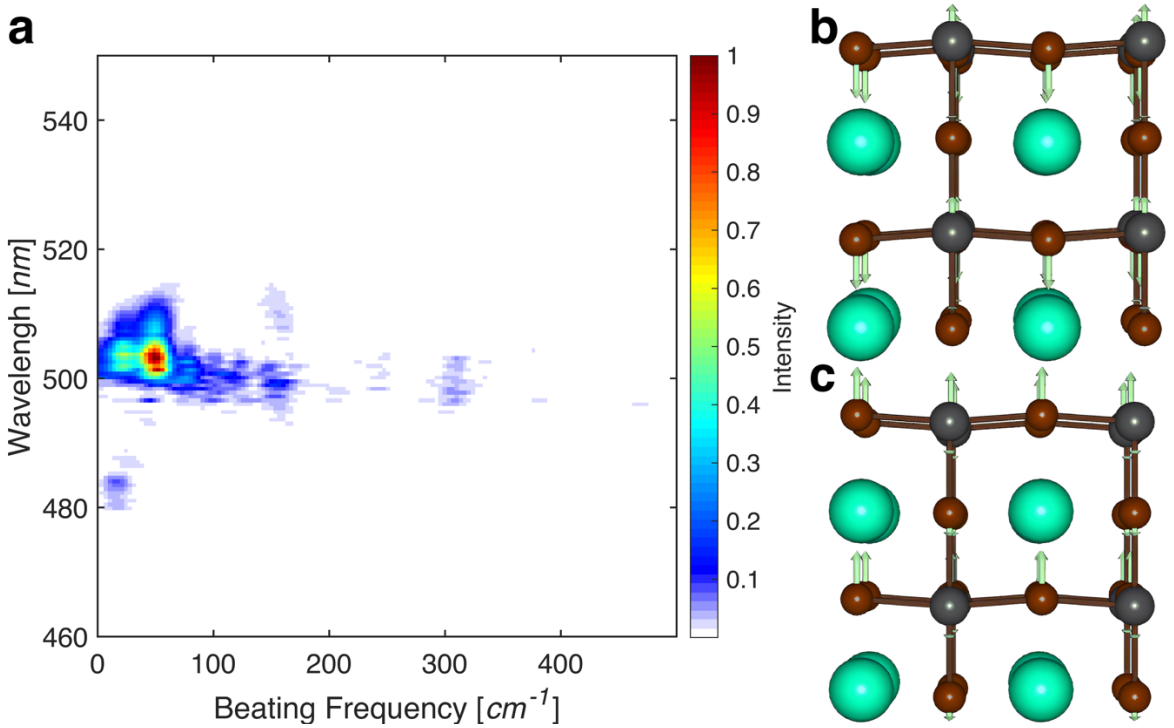


Figure 2.6: Beating frequency in $CsPbBr_3$ nanocrystals. a, Beating frequency, from the oscillation components, acquired through subtraction of the exponential decay (depicted in Figure A7). **b**, **c**, The bending mode of Pb-Br-Pb is illustrated, presenting two distinct time snapshots in panels (**b**) and (**c**).

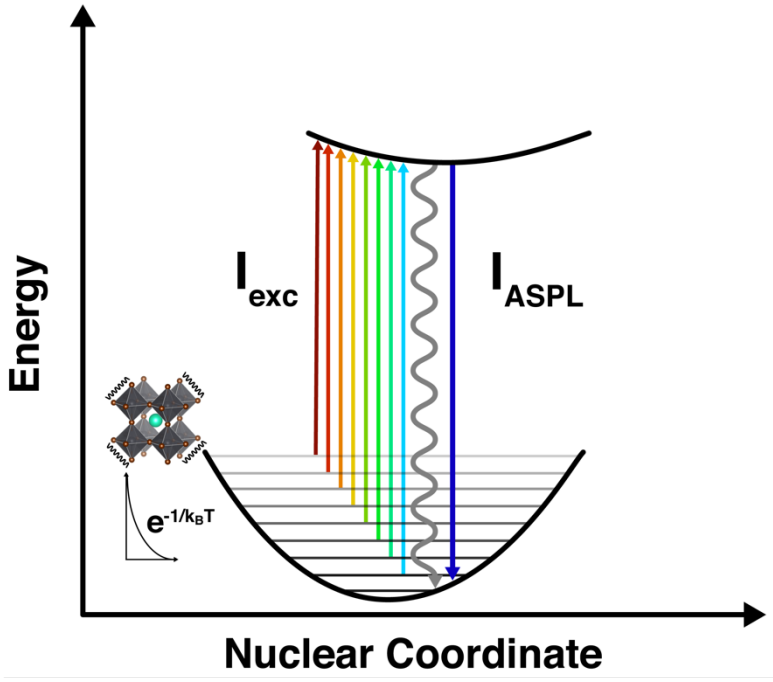
2.3 Conclusion

In conclusion, our study on the intricate dynamics of excited states reveals that the efficient up-conversion observed in $CsPbBr_3$ nanocrystals is driven by the Pb-Br-Pb bending mode. We also reveal that, under the below-gap excitation condition, coherent phonons unexpectedly emerge at the early times within the subset of nanocrystals undergoing up-conversion as polarons form. This result indicates that the up-conversion and subsequent relaxation is accompanied by a synchronized and phased lattice motion. This study emphasizes how the intricate and unique interplay between the soft lattice structure, phonons, and excited states dynamics of $CsPbBr_3$ nanocrystals facilitate the up-conversion process. Utilization of different lead-halide compositions with dominantly higher energy phonon modes, such as the Pb-X stretching mode, may improve up-conversion efficiency.

Chapter 3. Phonon-Driven Up-Conversion Dynamics in Pure Halide Perovskite Nanocrystals

3.1 Introduction

Lead-halide perovskites have attracted significant attention in the past few years as highly promising nanomaterials for phonon-driven up-conversion. This is attributed to their distinctive characteristics including a soft lattice, narrow emission linewidth, and near-unity photoluminescence quantum yield (PLQY) owing to their low trap density and tolerance for shallow surface defects[5,15,50,51,17–19,22,28,29,32,49]. In phonon-driven up-conversion, electrons initially populate thermally and vibronically available states residing above the valence band edge creating a thermal bath that follows a Boltzmann distribution. Electrons from this thermal distribution can absorb sub-bandgap photons to arrive at the conduction band edge. This transition, in an ideal case, is followed by anti-Stokes photoluminescence (ASPL), in which the emitted photons are of higher energy than the absorbed ones. Scheme 3.1 illustrates this sequential process.



Scheme 3.1: Molecular picture of energy levels illustrating the up-conversion process and anti-Stokes photoluminescence (ASPL) in perovskite nanocrystals. Electronics states emerge as a result of lattice vibrations which are thermally populated following Boltzmann distribution. Through sub-bandgap phonon-assisted light absorption, a valence electron is excited to the conduction band followed by ASPL, hence reducing the lattice phonon population.

Previous studies on phonon-driven up-conversion have been conducted on two-dimensional lead iodide[32], mixed-halide perovskites[52,53], and $CsPbBr_3$ nanocrystals[17,54]. In particular, $CsPbBr_3$ nanocrystals, on an ensemble and single-particle level, have been shown to exhibit up-conversion efficiencies of up to 75% when the excitation is detuned below the gap by around 23 meV[17]. Investigation of the up-conversion process in other pure-halide perovskite nanocrystals, such as $CsPbCl_3$ and $CsPbI_3$, offers prospective means to identify features of the materials such as any particular phonon mode that bolsters efficient up-conversion.

Here, we employ a combination of steady-state and time-resolved techniques to determine the up-conversion efficiency in pure-halide perovskite nanocrystals. Our work not only aims to discern any specific phonon that aids efficient up-conversion but also investigates the intricate electron-phonon couplings within these nanocrystals that undergo up-conversion. Using a Xenon lamp that is dually monochromated for especially narrow bandwidth, we retrieved an exponential relationship between the excitation wavelength and the ratio of illumination intensity to the ASPL intensity. Through this process, we extracted the characteristics phonon energy that contributes to up-conversion. From steady-state measurements, we identified specific phonon modes for each halide system as follows: $CsPbCl_3$ nanocrystals exhibited a phonon mode with an average energy of $8.1\ \text{meV}\ (66\ \text{cm}^{-1})$ that corresponds to a transverse optical (TO) mode predominantly involving the stretching of Cl atoms within the $[PbCl_3]^-$ cage[55,56]. For $CsPbBr_3$ nanocrystals, the phonon mode was identified as Pb-Br-Pb bending mode with an average energy of $7.9\ \text{meV}\ (64\ \text{cm}^{-1})$[27,33–35], while the primary phonon mode in $CsPbI_3$ nanocrystals corresponds to the stretching of Pb-I with an average energy of $10.4\ \text{meV}\ (84\ \text{cm}^{-1})$[57]. These phonon modes were further evaluated by Raman measurements.

In time-resolved measurements, transient absorption (TA) results for above gap excitation $CsPbCl_3$ and $CsPbBr_3$ nanocrystals aligned with anticipated intraband cooling characteristics; however, the TA data for $CsPbI_3$ nanocrystals behaved differently. Instead of a consistent pattern, $CsPbI_3$showed a fluctuating integrated TA signal over time, indicating a diffusive dynamic[58], as elaborated next. The below-gap excitation of chloride and bromide perovskite nanocrystals revealed unexpected coherent phonon oscillations, but these were absent in iodide perovskite nanocrystals. These coherent lattice vibrations consistent with the frequency of the TO mode and of the Pb-Br-Pb bending mode in $CsPbCl_3$ and $CsPbBr_3$ nanocrystals that are undergoing up-conversion, respectively. Unlike chloride and bromide perovskite nanocrystals, TA results for $CsPbI_3$ nanocrystals undergoing up-conversion lack coherent oscillations and exhibit characteristics resembling that of diffusive and disordered liquid-like dynamics. This results in random lattice vibrations along charge redistribution on the way to forming polarons[58]. Our findings in the steady-state and time-resolved measurements suggest that even though the up-conversion process utilizes the vibrational degree of freedom of lead halide frameworks in all three perovskites, its detailed up-conversion mechanism can be distinctly different. This work sheds light on the potential for phonon-driven up-conversion in pure-halide perovskites, broadening the scope to include chloride, bromide, and iodide perovskite nanocrystals. It emphasizes distinctive correlations between the halides and the mode of the phonons driving the up-conversion, highlighting their influence on the lattice vibrations whether through coherent or diffusive dynamics.

3.2 Results & Discussion

3.2.1 Steady-State Characterizations

We performed investigations of phonon-driven up-conversion, also termed anti-Stokes photoluminescence (ASPL), in order to identify the specific phonon modes involved in different pure-halide perovskite nanocrystals, specifically $CsPbX_3$ where X represents Cl, Br, or I. These nanocrystals were synthesized using a modified version of previously published reports to produce highly luminescent and monodisperse nanocrystals[15,23]. Figure 3.1a shows the steady-state absorption and photoluminescence (PL) spectra of each of the three halide perovskites with emission of 402 nm for chloride, 509 nm for bromide, and 690 nm for iodide perovskites. The nanocrystals, synthesized without any post-synthetic treatments, exhibited photoluminescence quantum yield (PLQY) as follow: $50.12\% \pm 5\%$ for $CsPbCl_3$, $100\% \pm 2\%$ for $CsPbBr_3$, and $97.3\% \pm 2\%$ for $CsPbI_3$ (see Figure B1). The high PLQY is an attribute of lead-halide perovskite nanocrystals, and also allows us to study the sub-bandgap dynamics without significant non-radiative processes that could complicate resulting dynamics. X-ray diffraction (XRD) patterns of these nanocrystals reveal cubic symmetries (Figure 3.1b, reference patterns in Figure B3). Transmission electron microscopy (TEM) images in Figure 3.1c, d and e, along their High-Resolution TEM and their respective Fast Fourier Transform (FFT) patterns illustrate highly monodisperse cubic nanocrystals with each of the halides showing size distributions[59] as follow: $6.5 \pm 0.43\ nm$ for Cl, $7.79 \pm 0.68\ nm$ for Br, and $11.77 \pm 2.07\ nm$ for I. These nanocrystals fall within the intermediate quantum confinement regime determined by the respective Bohr radii of $5\ nm$, $7\ nm$, and $12\ nm$ for $CsPbCl_3$, $CsPbBr_3$, and $CsPbI_3$[15]. Large area TEM images are shown in Figure B2 which further relate narrow size distribution.

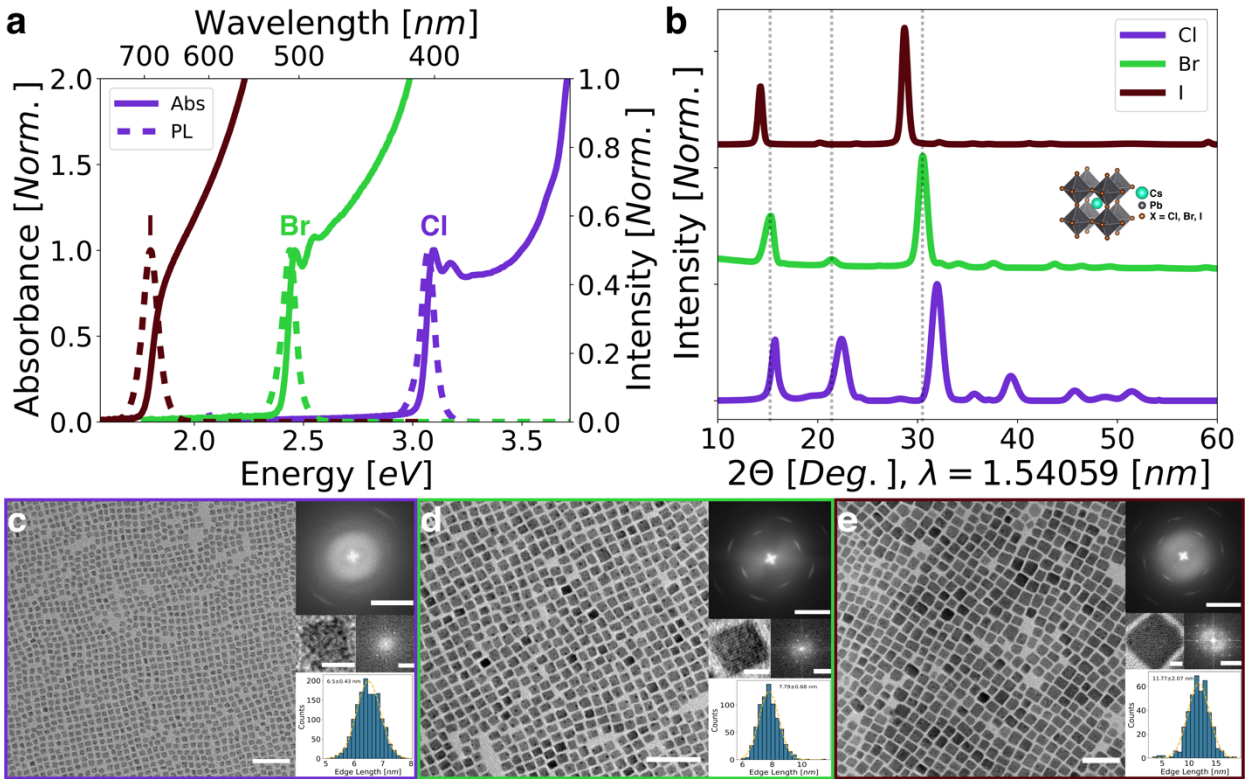


Figure 3.1: Steady-state characterizations of pure-halide perovskite nanocrystals. (a) Absorption and photoluminescence (PL) spectra of halide perovskites. (b) X-ray diffraction (XRD) patterns for $CsPbCl_3$, $CsPbBr_3$, and $CsPbI_3$ nanocrystals with cubic symmetry (reference patterns in Figure B3) with inset illustrating the cubic crystal structure modeled with Vesta software[38]. (c-e) Transmission electron microscopy (TEM) images and their corresponding Fast Fourier Transform (FFT) pattern, along with high-resolution TEM (HRTEM) images and their FFT patterns displaying monodispersed cubic nanocrystals of chloride, bromide, iodide perovskites. Each image is accompanied with the size distribution measured: $6.5 \pm 0.43\ nm$ for Cl, $7.79 \pm 0.68\ nm$ for Br, and $11.77 \pm 2.07\ nm$ for I. Scale bars: main TEM – $50\ nm$, main FFT – $2\ nm^{-1}$, HRTEM – $5\ nm$, HRTEM FFT – $3\ nm^{-1}$. Note: the presence of dark dots observed on some nanocrystals TEM images is attributed to the reduction of metallic lead atoms (Pb^0) induced by the electron beam.

3.2.2 Phonon-Driven Up-Conversion in $CsPbX_3$ Nanocrystals

A Xenon lamp was directed through a dual monochromator to produce a narrow linewidth excitation (~3 nm) to photoexcite the nanocrystals below gap at different wavelengths. We initially anticipated the need for a coherent light source such as laser illumination for sub-bandgap excitation of the nanocrystals to observe up-conversion. However, we found that incoherent photons from the Xenon lamp are equally effective, solidifying the idea that there exists a thermalized bath of electrons above the valence band edge that are excited thermally and vibronically, as illustrated in Scheme 3.1.

Figures B4a, B5a and B6a (and their insets) show the ASPL as a result of sub-bandgap excitation at room temperature over an energy range that is detuned below the bandgap. Whereas several investigations of ASPL primarily focused on Br perovskite nanocrystals[5,17], results presented here extend this understanding by showing that other pure halides (i.e. Cl and I) exhibit comparable up-conversion efficiency as shown in Figure 3.2a. This up-conversion efficiency was calculated following a previous report[5] as further discussed in the Appendix B.

The detected band edge emission intensity of the nanocrystals was compared to illumination intensity. As shown in Figure 3.2a, an exponential relation of excitation detuning to ASPL intensity was observed. An exponential relation is modeled to an Arrhenius equation to extract a characteristic energy (E_{ch}) as follows:

$$\frac{I_{exc}}{I_{aspl}} \propto e^{-\left(\frac{E_g - h\nu}{E_{ch}}\right)} \tag{1}$$

where E_g is the bandgap energy, $h\nu$ is the photon excitation energy, and E_{ch} is a characteristic energy. This characteristic energy involves both $\kappa_B T$ at room temperature (RT) and the phonon energy (E_p) responsible for the up-conversion process. Notably, Figure 3.2a shows that trends of ASPL efficiency with detuning do not overlap, so different characteristic phonon energy results from fitting to equation 1 with results shown in Figure 3.2b. Interestingly, we find that for different halides, there exists specific phonon modes implicated in up-conversion. In the chloride, a transverse optical (TO) mode predominates, characterized by the motion primarily involving Cl atoms within the $[PbCl_3]^-$ octahedral cage, with an averaged frequency of 66 cm^{-1}, in agreement with previous reports[55,56]. For bromide perovskites, on the other hand, an average frequency of 64 cm^{-1} corresponds to longitudinal optical mode involving the bending of Pb-Br-Pb[27,33–35]. Additionally, the phonon mode involved in the up-conversion process for the iodide was identified with an average frequency of 84 cm^{-1}, which is consistent with the Pb-I stretching mode[57]. Raman spectroscopy further corroborated the existence of these identified phonon modes as shown in Figure 3.2c with Stokes and anti-Stokes spectra (see Figure B7 for raw data and background fit). In the Raman spectra, the corresponding phonon modes for different halide perovskite nanocrystals are marked with asterisks.

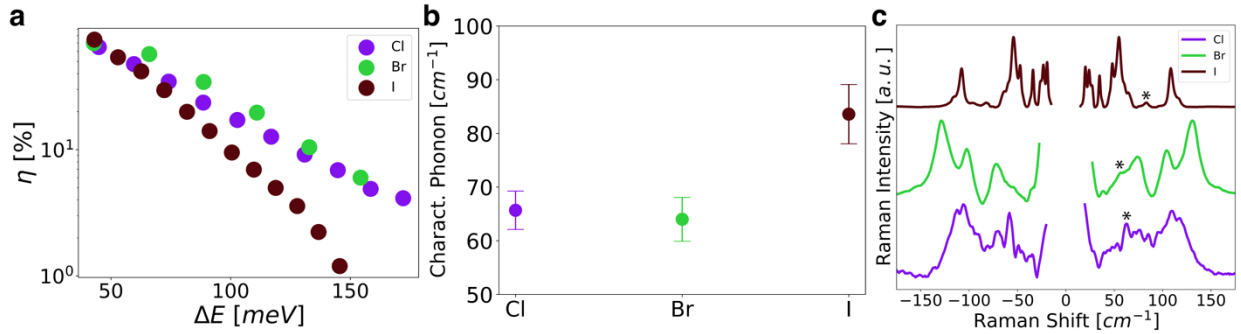


Figure 3.2: Up-conversion efficiency and phonon identification. (a) Up-conversion efficiency as a function of detuned energy within the bandgap. (b) Characteristic phonon modes extracted from the steady-state up-conversion and anti-Stokes photoluminescence (ASPL) measurements. Error bars represent the average data for each of the halide system. (c) Raman spectroscopy displaying Stokes and anti-Stokes signals with scattered laser at zero shift removed.

3.2.3 Transient Absorption (TA) and Pump Fluence Dependence

To further investigate the up-conversion process, we compared the early-time TA dynamics in all three pure-halide perovskite NCs with both above- and below-gap excitations. The above-gap excitation was delivered with power of $92\ \frac{\mu J}{cm^2}\ at\ 350\ nm$, $32\ \frac{\mu J}{cm^2} at\ 440\ nm$, and $29\ \frac{\mu J}{cm^2} at\ 590\ nm$ for chloride, bromide, and iodide perovskite nanocrystals, respectively. For below gap excitation, however, it is critical to investigate the pump fluence dependence of signal as the nanocrystals could achieve electronic excitation via two-photon absorption, which would also result in a different total energy deposition per excited electron. We first performed pump fluence dependence measurement for below-gap excitation (at 420 nm for Cl, 540 nm for Br, and 725 nm for I) and monitored the band edge bleach signals that correspond to electron-hole pair excitation. We observe a linear dependence, as illustrated in Figure 3.3, indicating that pumping within this power regime ensures a one-photon process consistent with up-conversion. This linear scale also allows us to choose a pump intensity level that optimizes the signal-to-noise ratio. Therefore, we set the below gap excitations for $CsPbCl_3$, $CsPbBr_3$, and $CsPbI_3$ to $739\ \frac{\mu J}{cm^2} at\ 420\ nm$, $217\ \frac{\mu J}{cm^2} at\ 540\ nm$, and $113\ \frac{\mu J}{cm^2} at\ 725\ nm$, respectively.

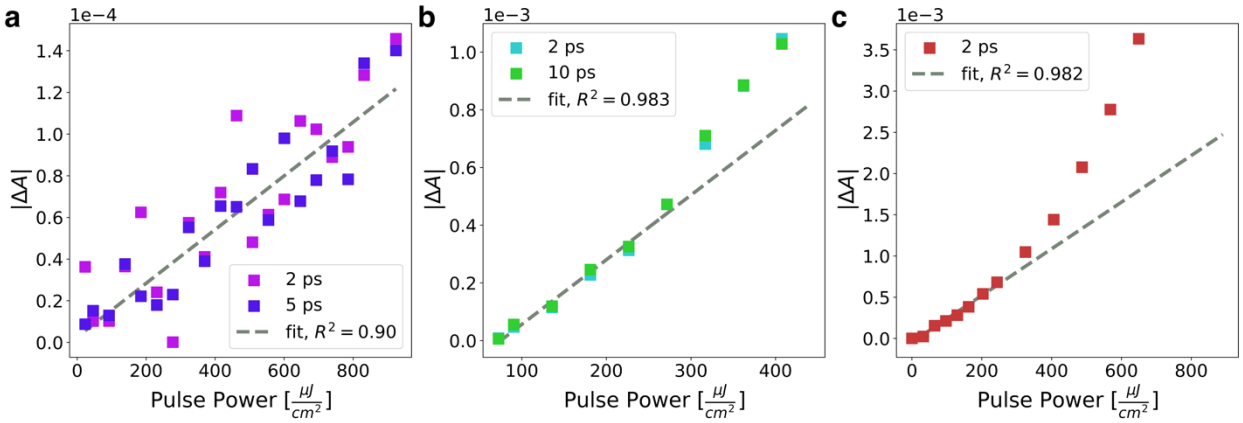


Figure 3.3: Transient absorption (TA) and pump fluence dependence. Band edge bleach signal as a function of pump power for (a) $CsPbCl_3$, (b) $CsPbBr_3$, and (c) $CsPbI_3$, revealing linear and superlinear regimes, important for choosing an optimal power to ensure a high signal-to-noise ratio but avoiding multiphoton excitation.

3.2.4 Excited States Dynamics in Pure Halide Perovskite Nanocrystals

For above gap excitation, the TA spectral maps and the selected time slices shown in Figure 3.4 for the three pure-halide systems exhibit distinct features. Upon photoexcitation, a band-edge bleach and a below-band edge photoinduced absorption (PIA_1) at ~410 nm for $CsPbCl_3$ (Figure 3.4a, 3.4b), ~515 nm for $CsPbBr_3$ (Figure 3.4c, 3.4d), and ~705 nm for $CsPbI_3$ (Figure 3.4e, 3.4f) are present. This red-shifted PIA_1 (relative to the bleach peak) is consistent with the formation and relaxation of a hot exciton state. This feature conveys the intraband cooling of electrons and holes to band-edge states, with energy released nonradiatively through phonons or Auger mechanisms[44,45,60,61]. It is noteworthy that if the exciton cooling occurs rapidly (faster than a

phonon period), the generated phonons could exhibit an oscillatory pattern, observable in the TA signal. However, under the above-gap excitation conditions in this study, none of the compositions show such a behavior. In the TA contour plot for the first 2 ps of delay time, $CsPbCl_3$ and $CsPbBr_3$ share similar spectral features. The red-shifted PIA then transitions to a blue-shifted PIA_2 at 385 nm for $CsPbCl_3$ and 485 nm for $CsPbBr_3$ This PIA transition is attributed to exciton-to-biexciton transition[60]. Moreover, when integrating the areas under the TA curves at different time slices (see insets of Figure 3.3b, d, f), we observe that $CsPbCl_3$ and $CsPbBr_3$ reach a plateau within 0.7-1 ps, consistent with polaron formation timescales[27]. However, compared to the other compositions, $CsPbI_3$ does not show the PIA_2 feature, and the integrated areas of the TA curves appear to fluctuate. This picosecond-fluctuating behavior of $CsPbI_3$ nanocrystals could be related to the diffusive and disordered liquid-like dynamics addressed in a previous report[58].

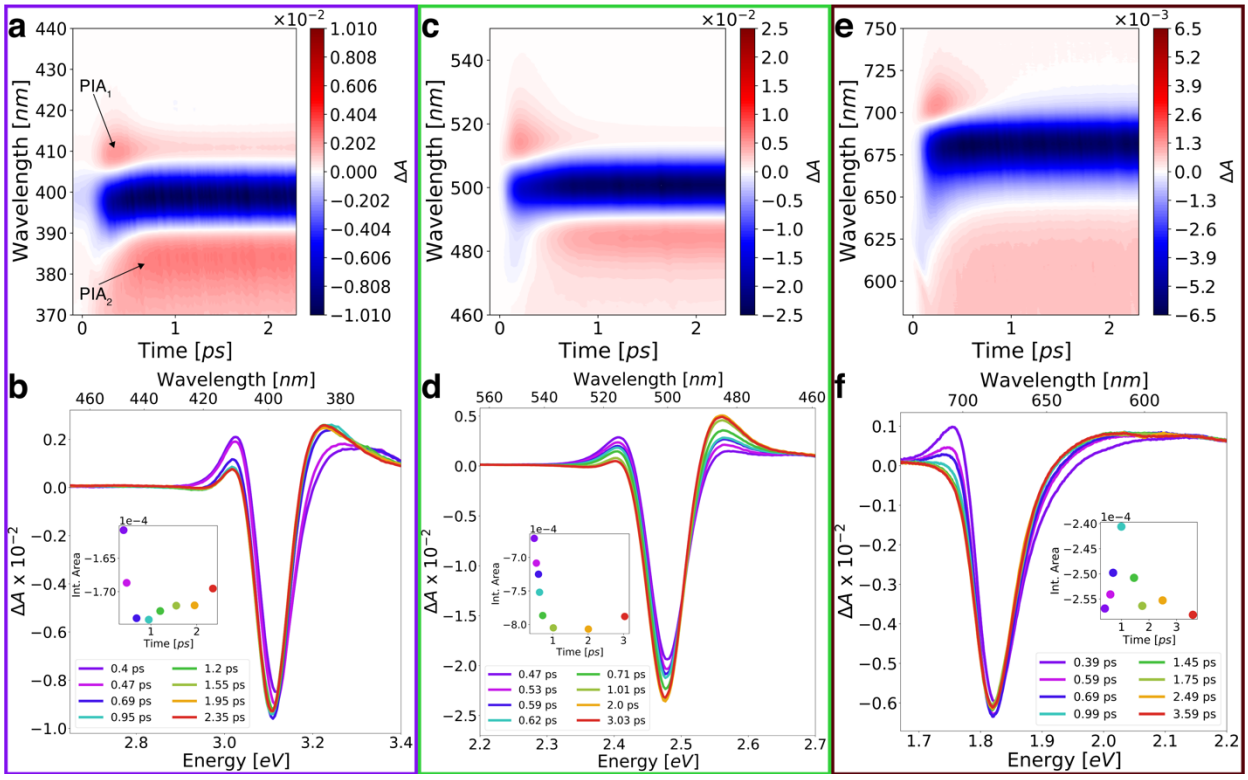


Figure 3.4: Above gap excitation time-resolved transient absorption (TA) measurement. TA spectral maps for (a) $CsPbCl_3$, (c) $CsPbBr_3$, and (e) $CsPbI_3$ perovskite nanocrystals showing typical signals (long-time limit bleach decays are presented in Figure B9). Selected time slices of TA spectra with their corresponding integrated area in insets for (b) $CsPbCl_3$, (d) $CsPbBr_3$, and (f) $CsPbI_3$. Expected lineshape is observed, except for $CsPbI_3$, where the absence of a blue-shifted photoinduced absorption (PIA_2) is noted. This absent PIA_2 is attributed to the diffusive and disordered liquid-like excited states dynamics in $CsPbI_3$ perovskite nanocrystal[58].

For below-gap excitation within the linear intensity regime, distinct characteristics appear in the TA spectra for three halide components. Setting aside the coherence artifact near time zero due to pulse overlap, we observe a subtle PIA_1 and a more pronounced PIA_2 in $CsPbCl_3$ (Figure 3.5a), that produces a similar second-order-derivative lineshape as compared to the above-gap excitation case (Figure 3.4b, 3.5b). What is different here is that the ΔA of PIA_1 remains nearly constant,

while the PIA_2 feature rises over time, yielding a monotonously decreasing trend in integrated area with pump-probe time delay. In $CsPbBr_3$ (Figure 3.5c, d), initial below-gap excitation only gives rise to PIA_1 with its absolute ΔA on a similar scale as the bleach, leading to a first-order derivative lineshape. At later time delay, a transition from PIA_1 into PIA_2 is observed, resembling the above gap excitation, indicating that an exciton-to-biexciton transition occurs. This PIA_1 is not expected to be present owing to an absence of hot excitons. The spectral features of $CsPbI_3$ are distinct from the chloride and bromide counterparts by missing both PIA_1 and PIA_2 (Figure 3.5e, f) in the linear regime. Within the first 500 fs upon photoexcitation, a spectral shift giving rise to the bleach is observed too, with opposite shift direction comparing to the above-gap excitation.

Unexpectedly, we observe an oscillatory signal in the TA spectra for $CsPbCl_3$ (Figure 3.5a, Figure B8a) and $CsPbBr_3$ (Figure 3.5c, Figure B8b) residing along the border of the PIA_2 and ground state-bleach. The oscillation amplitude in $CsPbCl_3$ is weaker than $CsPbBr_3$ (Figure B8), suggesting they may have different excited state potential energy surface along the direction of coherent oscillatory relaxation. However, no clear oscillatory signal in TA spectra was observed for $CsPbI_3$ (Figure 3.5e, Figure B8c). We attribute the absence of a coherent phonon oscillation to the fact that $CsPbI_3$ excited state dynamics behave like a disordered liquid and have an irreversible diffusive dynamic, perhaps spoiling coherent response.

The coherent phonon frequencies observed in $CsPbCl_3$ and $CsPbBr_3$ can be quantified using fast Fourier transform (FFT) across the temporal axis. We find a characteristic frequency of $57\ cm^{-1}$ for $CsPbCl_3$ (Figure 3.6a) that corresponds to the transverse optical (TO) mode involving the stretching motion of primarily Cl atoms within the $[PbX_3]^-$ octahedral cage[55,56]. We also find a characteristic frequency of $50\ cm^{-1}$ for $CsPbBr_3$ (Figure 3.6b) that is consistent with the Pb-Br-Pb bending mode[27,33–35]. The observation of this coherent phonons implicates active involvement of phonons in the ultrafast up-conversion and relaxation processes, even in the absence of hot excitons. Thus, nanocrystals undergoing up-conversion contain a quantum of distinct phonons that impulsively dissipate upon absorption, and the observed coherent oscillation reveals a dominant relaxation mechanism on the path to polaron formation.

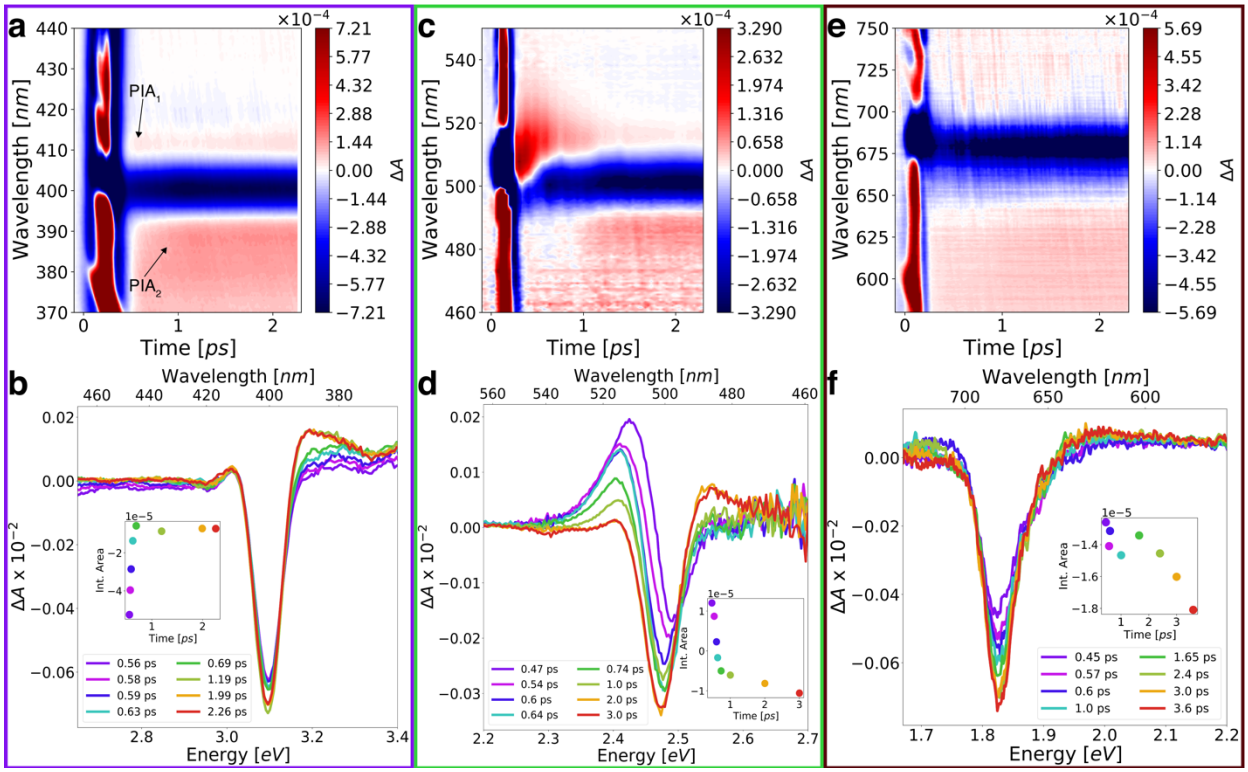


Figure 3.5: Below gap excitation time-resolved transient absorption (TA) measurement. TA spectral maps for (a) $CsPbCl_3$, (c) $CsPbBr_3$, and (e) $CsPbI_3$ perovskite nanocrystals showing faint and pronounced oscillatory signals at the intersection of the red-shifted photoinduced absorption (PIA_1) and ground-state bleach signals for chloride and bromide perovskites. Such oscillatory signal is absent in iodide perovskites. Selected time slices of TA spectra with their corresponding integrated area in insets for (b) $CsPbCl_3$, (d) $CsPbBr_3$, and (f) $CsPbI_3$. Unexpected red-shifted and blue-shifted PIAs (PIA_1 and PIA_2) are observed, except for $CsPbI_3$, where the absence of PIAs is unsurprising, given that below gap excitation does not generate hot excitons.

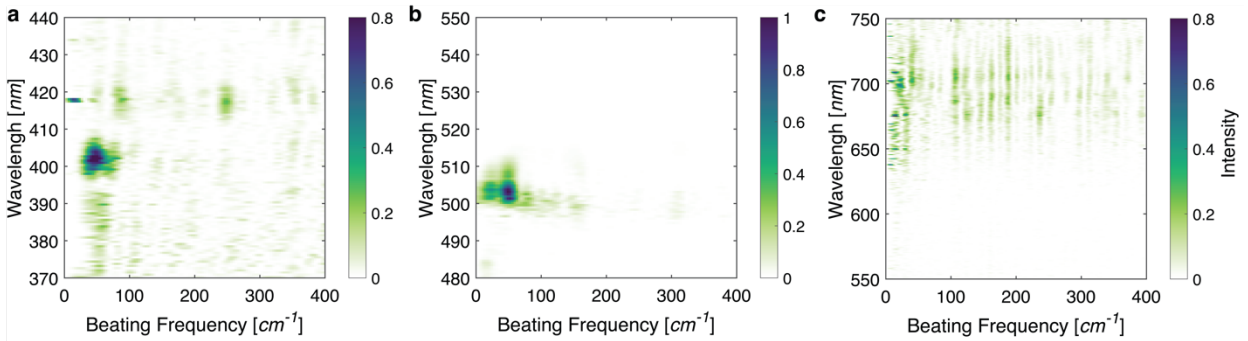


Figure 3.6: Beatmaps analysis. Beating frequency derived from the oscillation components by subtracting of the exponential decay (depicted in Figure B8) for (a) $CsPbCl_3$ exhibiting frequency of 57 cm^{-1}, (b) $CsPbBr_3$ with frequency of 50 cm^{-1}, and (a) $CsPbI_3$, which shows no beating frequency.

3.3 Conclusion

In conclusion, our study on the steady-state and excited-state dynamics of pure halide perovskite nanocrystals reveals not only efficient up-conversion, but also different type of phonon modes is involved in the up-conversion process. In $CsPbCl_3$, transverse optical mode involving primarily the stretching of chloride atoms was identified, while the Pb-Br-Pb bending mode was identified for $CsPbBr_3$. In $CsPbI_3$, the Pb-I stretching mode was responsible for the up-conversion. We also, unexpectedly, unveils the emergence of coherent phonon oscillations in $CsPbCl_3$ and $CsPbBr_3$ nanocrystals. However, this coherent phonon oscillations were absent in $CsPbI_3$ nanocrystals, and we attributed it to the fact that iodide perovskite exhibits disordered liquid-like and diffusive dynamics that potentially diminish any coherent oscillations. This work showcases the potential use of different halides that involves different phonon modes with distinct excited state dynamics for potential applications in laser cooling.

Chapter 4. Phonon-Driven Up-Conversion Dynamics in Mixed Halide Perovskite Nanocrystals

4.1 Introduction

Lead-halide perovskites have undergone significant research in the past few years due to their high promising optoelectronic properties, rendering them invaluable for applications in solar cells and light emitting devices[51,62,63]. Owing to their minimal trap density and tolerance to shallow defects, cesium lead halide perovskites ($CsPbX_3$, where X = Cl, Br, or I) exhibit narrow emission linewidth and near unity photoluminescence quantum yield (PLQY)[15,18,19,22,28,29,32,49,50,64]. One particular interesting frontier where lead-halide perovskites excel is in the phonon-assisted up-conversion. In the process of phonon-assisted up-conversion, valence electrons are initially excited through vibronic and thermal energy to vibronic states that emerge due to bandgap fluctuation. These electrons, distributed following the Boltzmann distribution, absorb a sub-bandgap photon to arrive at the edge of the conduction band. Subsequently, the electron can undergo through non-radiative recombination, generating heat, or radiatively recombine, emitting a photon. This emitted photon, in a process referred to as anti-Stokes photoluminescence (ASPL), is of higher energy than the one absorbed. This ASPL, which involve phonons, effectively reduces the phonon population in the lattice; thus, lowering the lattice temperature which is an essential process in solid-state laser cooling[5].

Recent thorough investigations of phonon-driven up-conversion have been conducted on layered structures[32] and nanocrystals perovskites[5,17]. However, significantly less attention has been dedicated to exploring phonon-assisted up-conversion in mixed halides[52,65]. Here, we focus our phonon-driven up-conversion investigation on mixed halides, namely, chloride-bromide (Cl:Br), iodide-bromide (I:Br), and bromide-iodide (Br-I) to elucidate the phonon energies and quantify the up-conversion efficiency. We synthesized mixed halide perovskites with composition of 25%, and for simplicity, we assume a composition in the final product to remain as 25%. Thus, we produced three different mixed halides as follow: $CsPbCl_{0.75}Br_{2.25}$, $CsPbI_{0.75}Br_{2.25}$, $CsPbBr_{0.75}I_{2.25}$ perovskite nanocrystals. Using a narrow bandwidth laser, we observe an exponential trend between the intensity of the sub-bandgap laser and the band edge emission, referred to as the ASPL. We modeled the exponential relation with an Arrhenius equation to extract an activation energy that we then extract the characteristics phonon energies for each mixed halide perovskites. We find the phonon energies as follow: $7.83\ meV$ $(63.17\ \mathrm{cm}^{-1})$ for $CsPbCl_{0.75}Br_{2.25}$, $4.07\ meV$ $(32.86\ \mathrm{cm}^{-1})$ for $CsPbI_{0.75}Br_{2.25}$, and $5.93\ meV$ $(47.84\ \mathrm{cm}^{-1})$ for $CsPbBr_{0.75}I_{2.25}$. We then computed the up-conversion efficiency for each mixed halides. Surprisingly, across all mixed halides, we observed a non-monotonic trend in the up-conversion efficiency, peaking at a higher detuned energies within the bandgap. In pure bromide perovskites ($CsPbBr_3$), the highest up-conversion of 75% occurs at sub-bandgap excitation detuned by 23 meV within the bandgap[17]. In mixed halides, the up-conversion efficiency increases with excitation further into the bandgap, reaching a maximum around 75, 60, and 50 meV for Cl:Br, I:Br, and Br:I compositions, respectively. Therefore, the deeper the peak of the up-conversion efficiency occurs within in the

bandgap, the more effective the phonons annihilation during the up-conversion process, a crucial advantage for solid-state laser cooling. Overall, this study sheds light on optimizing the phonon-assisted up-conversion efficiency in perovskite nanocrystals via engineered halide compositions, paving the way for their potential application in laser cooling of solid-state materials.

4.2 Results & Discussion

While significant work has been done exploring the phonon-driven up-conversion in pure halide perovskites, there has been attention directed towards investigating mixed halides. Previous studies on mixed halide perovskites primarily emphasized their ability to up-convert when exciting below bandgap[52,53]. Here, we extend the investigation of mixed halides to extract precise phonon energies involved in the up-conversion, alongside quantifying the corresponding up-conversion efficiencies. Following a modified version of previously reported procedures[15,23], we first synthesized pure halides along with the desired mixed halides with composition as follow: 25% chloride to bromide (Cl:Br), 25% iodide to bromide (I:Br), and 25% bromide to iodide (Br:I). For simplicity, we assume a 25% composition, despite that the measurements conducted by scanning electron microscopy-energy dispersive spectroscopy (SEM-EDS) may occasionally overestimate or underestimate the compositions (see Figure C1). Figure 4.1a and b show the steady-state absorption and photoluminescence spectra, as well as the X-ray diffraction (XRD) patterns, for both pure and mixed halides. Based on the XRD patterns in Figure 4.1b, along with the reference patterns shown in Figure C2, all nanocrystals in this study exhibited cubic symmetry. The mixed halide perovskites, synthesized without any post-treatments, exhibited a range of moderated to high photoluminescence quantum yield (PLQY) as illustrated in Figure C3. $CsPbCl_{0.75}Br_{2.25}$, $CsPbI_{0.75}Br_{2.25}$, and $CsPbBr_{0.75}I_{2.25}$ nanocrystals displayed PLQY of $100\% \pm 2\%$, $49.4\% \pm 2\%$, and $93.8\% \pm 2\%$, respectively. Figure 4.1c-e illustrate the transmission electron microscopy (TEM) images of the three mixed halide perovskites, displaying highly monodisperse cubic nanocrystals with each mixed halides showing size distribution[59] as follow: $5.56 \pm 0.52\ nm$ for Cl:Br, $8.49 \pm 1.15\ nm$ for I:Br, and $9.2 \pm 1.38\ nm$ for Br:I. It is worth noting that transitioning from mixing chloride with bromide to mixing iodide with bromide resulted in larger nanocrystals, even when maintaining identical synthesis conditions such as temperature and quench time. Additionally, to ensure the homogenous mixing of halides within the nanocrystals, we performed above and below gap excitation (Figure C4a), all resulting in a band edge emission. Photoluminescence excitation (PLE) scans were also performed both above and below gap, which consistently resulted in identical spectra (Figure C4b), thus confirming a homogenously mixed halide perovskite nanocrystals.

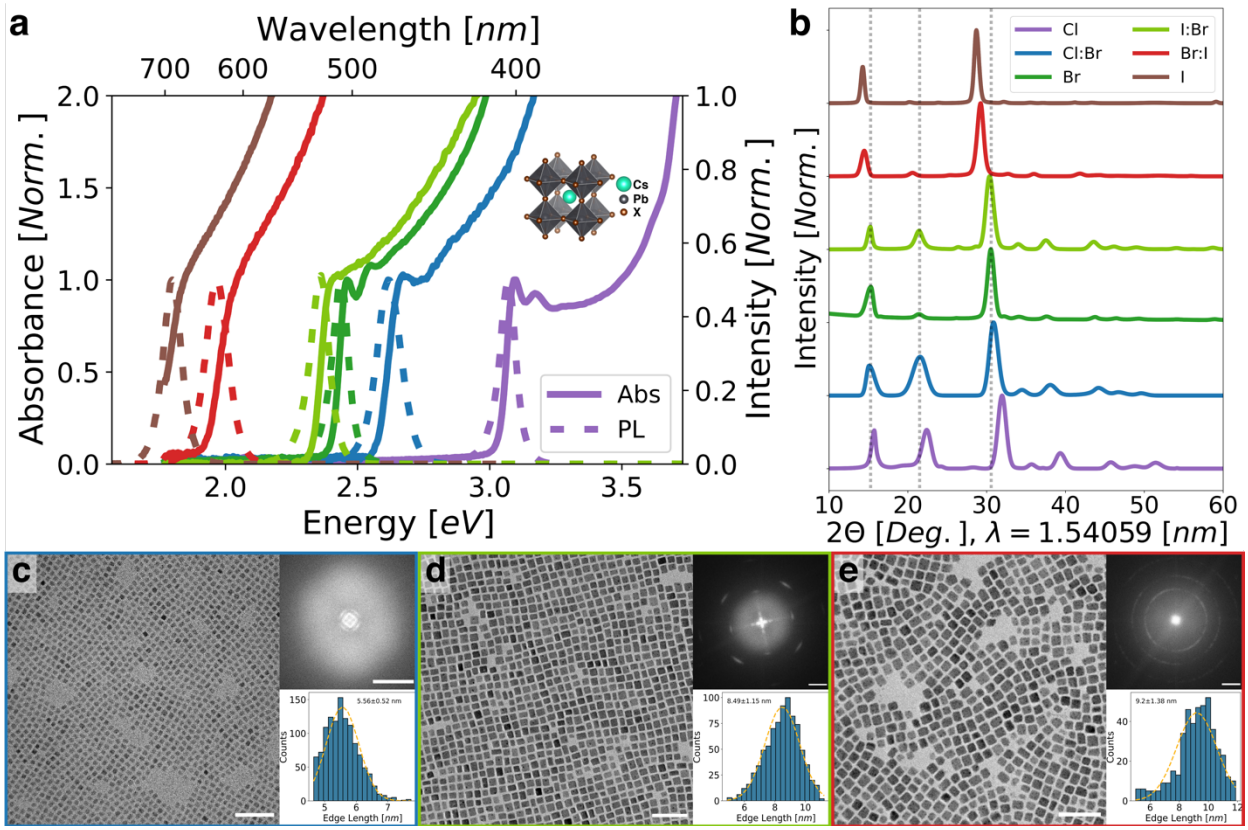


Figure 4.1: Steady-state characterizations of mixed halide perovskite nanocrystals. (a) Absorption and photoluminescence (PL) spectra of mixed halide perovskites, with inset illustrating the cubic crystal structure modeled with Vesta software[38]. (b) X-ray diffraction (XRD) patterns for $CsPbCl_3$, $CsPbCl_{0.75}Br_{2.25}$, $CsPbBr_3$, $CsPbI_{0.75}Br_{2.25}$, $CsPbBr_{0.75}I_{2.25}$, and $CsPbI_3$ nanocrystals with cubic symmetry (reference patterns in Figure C2). (c-e) Transmission electron microscopy (TEM) images and their corresponding Fast Fourier Transform (FFT) pattern, displaying monodispersed cubic nanocrystals of mixed Cl:Br, I:Br, and Br:I perovskites. Each image is accompanied with the size distribution measured: $5.56 \pm 0.52\ nm$ for Cl:Br, $8.49 \pm 1.15\ nm$ for I:Br, and $9.2 \pm 1.38\ nm$ for Br:I. Scale bars: main TEM – 50 nm, main FFT – 1 nm^{-1}. Note: the presence of dark dots observed on some nanocrystals TEM images is attributed to the reduction of metallic leads (Pb^0) induced by the electron beam.

We set out to investigate the phonons driving the up-conversion in mixed halide perovskites, aiming to quantify their up-conversion efficiencies. Using a narrow bandwidth laser, we excited the nanocrystals with a sub-bandgap photon with energy detuned within the bandgap. This excitation transitions a valence electron, facilitated by phonons, to the conduction band. This up-conversion process is followed by anti-Stokes photoluminescence (ASPL), which completes the cycle of phonon annihilation from the lattice. Figure C5a, C6a, and C7a and their respective insets show the sub-bandgap excitations with the band edge emission for each mixed halide perovskites. By analyzing the ratio between intensity and band edge emission, we realized an exponential relation that we modeled with Arrhenius equation to retrieve an activation energy encompassing the characteristic phonon energy and $\kappa_B T$ at room temperature. Deconvoluting and assigning the characteristic phonon energies extracted from the steady-state PL is particularly challenging when

dealing with mixed halides. Nonetheless, we find the corresponding phonon energies as follow: 7.83 meV (63.17 cm^{-1}) for $CsPbCl_{0.75}Br_{2.25}$, 4.07 meV (32.86 cm^{-1}) for $CsPbI_{0.75}Br_{2.25}$, and 5.93 meV (47.84 cm^{-1}) for $CsPbBr_{0.75}I_{2.25}$.

Following a similar approach reported previously[5,17] for calculating the up-conversion efficiency (further detailed in the SI), we computed the up-conversion efficiencies for mixed halide perovskites as illustrated in Figure 4.2. Unexpectedly, the up-conversion efficiencies in mixed halide perovskite nanocrystals exhibited non-monotonic trend unlike the pure counterparts. To understand this non-monotonicity, we must consider the fact that now each nanocrystal consists of two different halides, characterized by different masses and spring constants within the $[PbX_3]^-$ octahedral cage. Each halide introduces a distinct set of vibronic states positioned above the valence band with different spacing that are then vibronically and thermally populated according to the Boltzmann distribution. These vibronic states are spaced based on the mass of the halide and its spring constant of its bond with lead. For example, we expect chloride to exhibit stronger vibration and fluctuation in the band gap compared to bromide and iodide. Figure 4.3 illustrates the up-conversion process with vibrational density of states (DOS). The emergence of these vibronic states is attributed to the bandgap fluctuations. Each halide induces distinct fluctuation in the bandgap, producing a set of states such that the combinations of the two halides vibrational DOS contain higher electron density at higher detuned energies, resulting in a non-monotonicity in up-conversion efficiency.

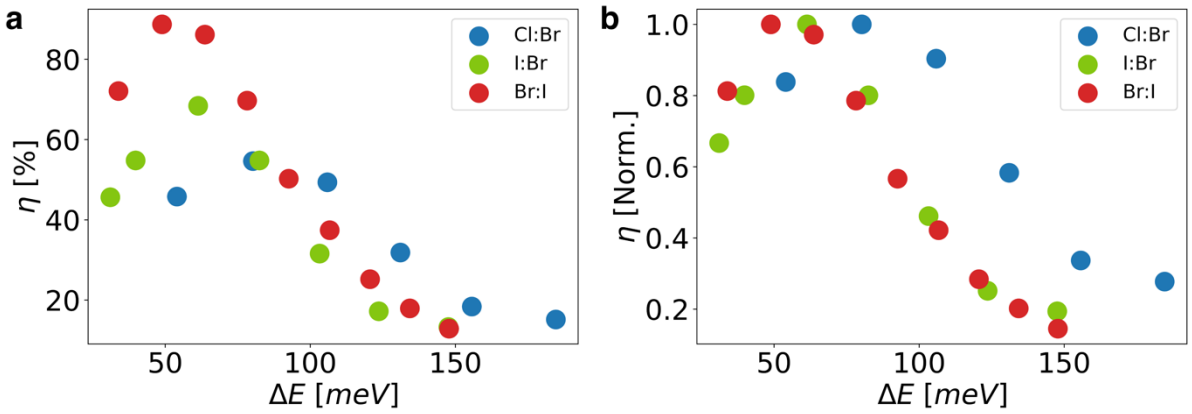


Figure 4.2: Up-conversion efficiency in mixed halide perovskites. (a) Computed up-conversion efficiency for mixed halides with composition of 25% as a function of detuned energies within the bandgap. The figure highlights the non-monotonic trend that is attributed to the two-phonon contributions from each halide, which distinctly fluctuates the bandgap. (b) Normalized up-conversion efficiency illustrates the position of the up-conversion maximum for each halide. Specifically, it indicates that chloride-bromide mix exhibit larger detuned energy resulting in maximum efficiency in up-conversion.

It is noteworthy to mention that transitioning from chloride to iodide mix yields higher up-conversion efficiencies (Figure 4.2a). We also observe that the peak shifts to a lower detuned energy in Br:I compared to Cl:Br as illustrated clearly in the normalized up-conversion efficiency in Figure 4.2b. This further reinforces that the maximum vibrational DOS arises from the combination of independent halide vibronic states, as shown in Figure 4.3.

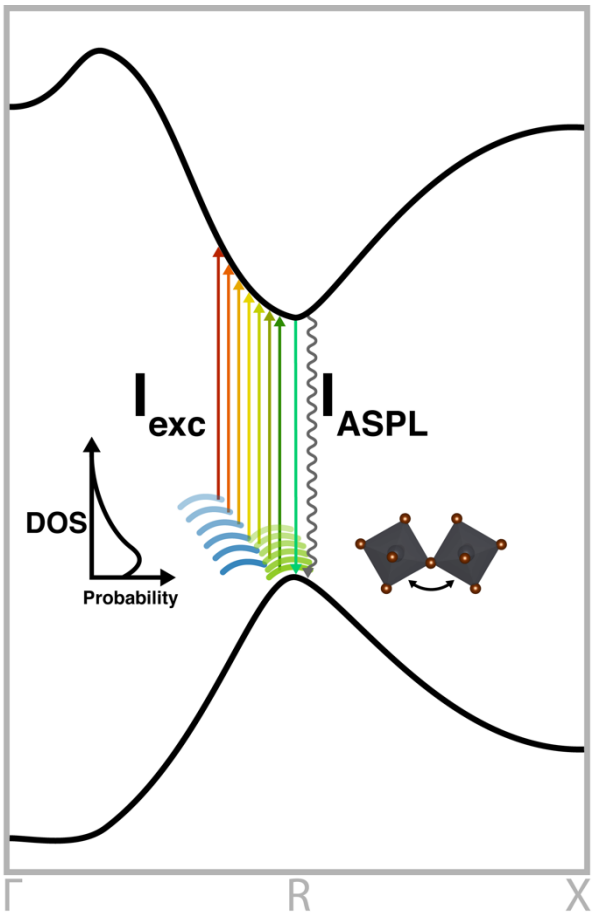


Figure 4.3: Non-monotonic up-conversion process in mixed halide perovskites. In mixed halide perovskites, each halide, based on its mass and spring constant, produces a distinct set of vibronic density of states (DOS) that results from bandgap fluctuations. These states are spaced differently for each halide, and when combined together, they produce a maximum in DOS which are thermally populated by valence electrons following Boltzmann distribution. Sub-bandgap photons excite these electrons to the conduction band, followed by anti-Stokes photoluminescence (ASPL). Since we have a maximum in DOS that is at a deeper detuned energy, the computed up-conversion efficiency exhibit a non-monotonic behavior.

To rule out surface effects, such as acoustic phonons, we computed the up-conversion efficiency of I:Br mixed halides with different sizes, all produced from the same synthesis to ensure composition consistency (Figure C8, C9, and C10). One size is in the strong quantum confined regime (Figure C10a), which typically has a strong surface effect, while the other is in the intermediate quantum confinement regime (Figure C10b). The quantum confinement is evident by the excitonic feature shown in Figure C8d and C9d, corresponding to the strong and intermediate regimes, respectively. As shown in Figure 4.4, the up-conversion efficiency still exhibits non-monotonicity, reaching its maximum peak at the same detuned energy irrespective of the nanocrystal size. Thus, we can confirm that this non-monotonic trend in up-conversion efficiency is a result of two-phonons process by which different halides fluctuate the bandgap differently producing vibronic states residing above the valence band with different energy spacing. These vibronic states form a DOS that, when combined, leads to a peak in up-conversion efficiency.

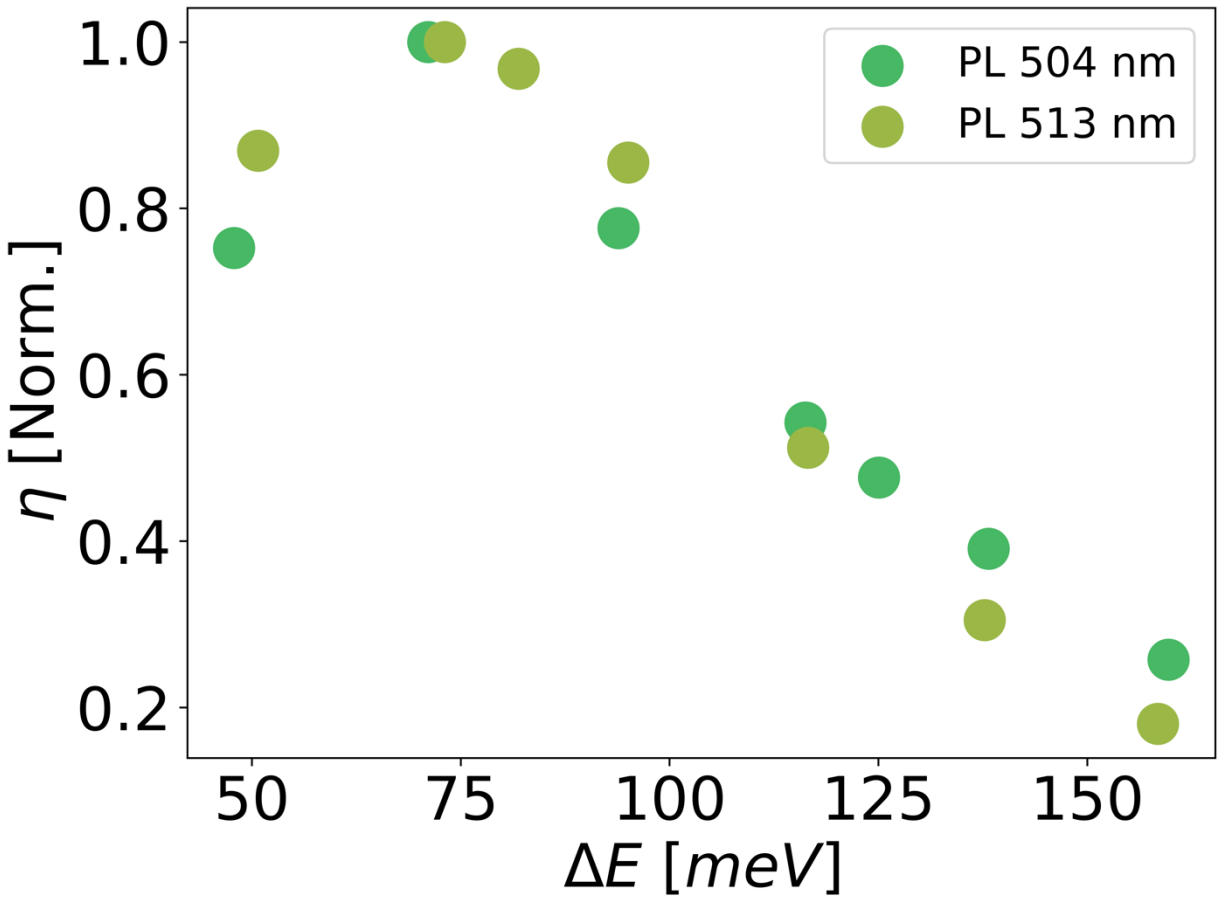


Figure 4.4: Size-dependent up-conversion efficiency in mixed halide perovskites. Normalized up-conversion efficiency as a function of detuned energy for $CsPbI_{0.75}Br_{2.25}$ perovskites of varying sizes. Photoluminescence (PL) emission at 504 nm corresponding to nanocrystals sized at $6.16 \pm 0.87\ nm$ (Figure C10a), while emission at 513 nm corresponding to nanocrystals sized at $6.78 \pm 0.93\ nm$ (Figure C10b). Regardless of the nanocrystal size, the peak of the non-monotonic up-conversion efficiency coincides at the same detuned energy.

4.3 Conclusion

In conclusion, in this extended work on perovskite nanocrystals for phonon-driven up-conversion in mixed halides, we reveal that not only it is possible to achieve efficient up-conversion, but also there exist a non-monotonic trend in up-conversion. We found that the up-conversion increases as we detuned the sub-bandgap excitation deeper within the bandgap before it decreases, which was unexpected. We attributed this non-monotonicity to the fact that in the nanocrystals consists of two different halides; each has different mass and spring constant that affect and fluctuate the bandgap differently. The combination of these fluctuation originating from the two distinct halides produce a set of vibronic density of states (DOS) that reside above the valence band that is not monotonic. This non-monotonic behavior in up-conversion efficiency allows to leverage higher energy to annihilate phonons within the lattice while maintaining high efficiencies. This work has directly implication in potentially maximizing the cooling power of nanocrystals for applications in laser cooling.

our study on the steady-state and excited-state dynamics of pure halide perovskite nanocrystals reveals not only efficient up-conversion, but also different type of phonon modes is involved in the up-conversion process. In $CsPbCl_3$, transverse optical mode involving primarily the stretching of chloride atoms was identified, while the Pb-Br-Pb bending mode was identified for $CsPbBr_3$. In $CsPbI_3$, the Pb-I stretching mode was responsible for the up-conversion. We also, unexpectedly, unveils the emergence of coherent phonon oscillations in $CsPbCl_3$ and $CsPbBr_3$ nanocrystals. However, this coherent phonon oscillations were absent in $CsPbI_3$ nanocrystals, and we attributed it to the fact that iodide perovskite exhibits disordered liquid-like and diffusive dynamics that potentially diminish any coherent oscillations. This work showcases the potential use of different halides that involves different phonon modes with distinct excited state dynamics for potential applications in laser cooling.

Chapter 5. Non-Monotonic Size-Dependent Exciton Radiative Lifetime in CsPbBr3 Nanocrystals

5.1 Introduction

Colloidal nanocrystals, also known as quantum dots (QDs), have attracted considerable attention due to their straightforward and inexpensive solution-phase synthesis and their wide-range spectral tunability from the quantum confinement effect[66,67]. Lead-halide perovskite nanocrystals, in particular cesium lead bromide ($CsPbBr_3$), have emerged in the past few years as highly desirable and efficient optical materials due to their facile synthesis, narrow emission linewidth, and near-unity photoluminescence quantum yield (PLQY) owing to their low trap density and tolerance for shallow surface defects[15,18,19,22,28,29,49–51,68]. Of particular interest when discussing photoluminescence is the radiative lifetime – the duration of an exciton before undergoing radiative recombination. This measure provides mechanistic insight into the efficiency of the light emitting process[69–71]. Specifically, the radiative lifetime reveals the intricate dynamics controlling the photoluminescence behaviors. Thus, a comprehensive understanding and optimization of the radiative lifetime becomes essential for the enhancement of optical materials. Nanocrystals with near-unity PLQY and short radiative lifetimes have possible applications in coherent quantum light emitters[72] and solid-state laser cooling[5]. For example, to observe laser cooling in solid-state materials, two processes must occur in rapid succession: exciton up-conversion followed by radiative recombination, resulting in anti-Stokes photoluminescence[5]. A shorter radiative lifetime enhances the likelihood of avoiding non-radiative pathways that induce heating, thereby maximizing the cooling probability. One way to tune the radiative lifetime is through the nanocrystal size[26,73]. For nanocrystals, three distinct quantum confinement regimes dictated by the Bohr radius – weak, intermediate, and strong – are commonly observed. Each regime exhibits unique electronic structure and optical properties, influencing factors such as the radiative lifetime. Notably, $CsPbBr_3$ nanocrystals have a relatively large Bohr diameter (~7nm), enabling experimental exploration across all three confinement regimes[15].

In this work, we set out to explore the effect of nanocrystal size on radiative lifetime under ambient conditions. Very high-quality $CsPbBr_3$ nanocrystals were synthesized to ensure monoexponential decay behaviors, enabling direct extraction of the radiative lifetime. Unexpectedly, our results unveil a non-monotonic trend in the radiative lifetime. The smaller nanocrystals within the strong confinement regime and larger nanocrystals within the weak confinement regime surprisingly exhibited longer radiative lifetimes, while the intermediate confinement regime displays the shortest radiative lifetime. Interestingly, we observed a symmetry lowering transition from the cubic to the orthorhombic phase[74–78] of the $CsPbBr_3$ nanocrystal system in a coincidentally similar size regime, aligning with the inflection point observed in the radiative lifetimes. Both X-ray diffraction (XRD) patterns and molecular dynamics simulations conducted on $CsPbBr_3$

nanocrystals with varying sizes confirm the occurrence of this phase transition. However, we find no evidence that this phase transition has a direct influence on the radiative lifetime.

In previous work investigating size-dependent lifetime in $CsPbBr_3$ under low temperature conditions (~4-5 K), revealed an exponential trend, with radiative lifetime decreasing as the size increases[26,72]. Under ambient conditions, however, the work of Krieg *et al* shows the reverse trend[73]. It was rationalized that higher lying states become thermally accessible at ambient conditions and introduce a delay in the radiative recombination of excitons[73]. Neither of these studies thoroughly explored the inflection point marking the transition from the intermediate to the strong confinement regime.

In larger nanocrystals within the weak confinement regime, we ascribe the lengthening of the radiative lifetime to the thermal population of high-lying dim states within $3\kappa_B T$. These states effectively mix with the lowest bright state under ambient conditions, resulting in a delay in the radiative lifetime for weakly confined nanocrystals where the density of states is high. This observation finds support from a previous work where the lengthening of radiative lifetime is attributed to the mixing of S state with higher P state that are symmetry forbidden[73]. The smaller nanocrystals within the strong confinement regime, show longer radiative lifetimes due to a reduction in oscillator strength. In contrast, intermediately confined nanocrystals exhibit the shortest radiative lifetime, as the effect of states mixing is reduced in this regime along with an enhancement in the oscillator strength. The non-monotonic trend in radiative lifetime observed in the present study appears to reflect a behavior common among intensively studied II-VI (CdSe), III-V (InP), and perovskite semiconducting nanocrystals[70,79–81]. In all, this study provides a thorough insight into the size-dependent radiative lifetime in $CsPbBr_3$ nanocrystals, paving the way to engineer materials with tailored decay rates to meet diverse optical application needs.

5.2 Results & Discussion

We set out to investigate the effect of nanocrystal size on optical properties, focusing on the radiative lifetime. High-quality nanocrystals were synthesized following a modified version of previous reports to minimize non-radiative pathways and to directly extract the radiative lifetime. Figure 5.1a shows absorption and photoluminescence spectra of $CsPbBr_3$ nanocrystals in the strong, intermediate, and weak confinement regime. Figure 5.1c, d, and e show their corresponding Transmission Electron Microscopy (TEM) images (larger area shown in Figure D1) along with calculated size distributions[59], illustrating highly monodisperse ensemble. Photoluminescence Full-Width at Half Maximum (FWHM) and Stokes shift are extracted for different nanocrystal sizes revealing a linear trend. Both the FWHM and Stokes shift exhibit an increase as nanocrystal sizes decrease, which has been observed previously[82,83]. This linear trend is correlated between the size of the nanocrystals and the strength of coupling to high-energy optical phonons (2-17 meV)[83,84]. Specifically, smaller nanocrystals exhibit stronger coupling to these phonons. This coupling results in large fluctuations in the bandgap[85], consequentially causing broader emission linewidths and larger Stokes shift as evident in Figure 5.1a and b.

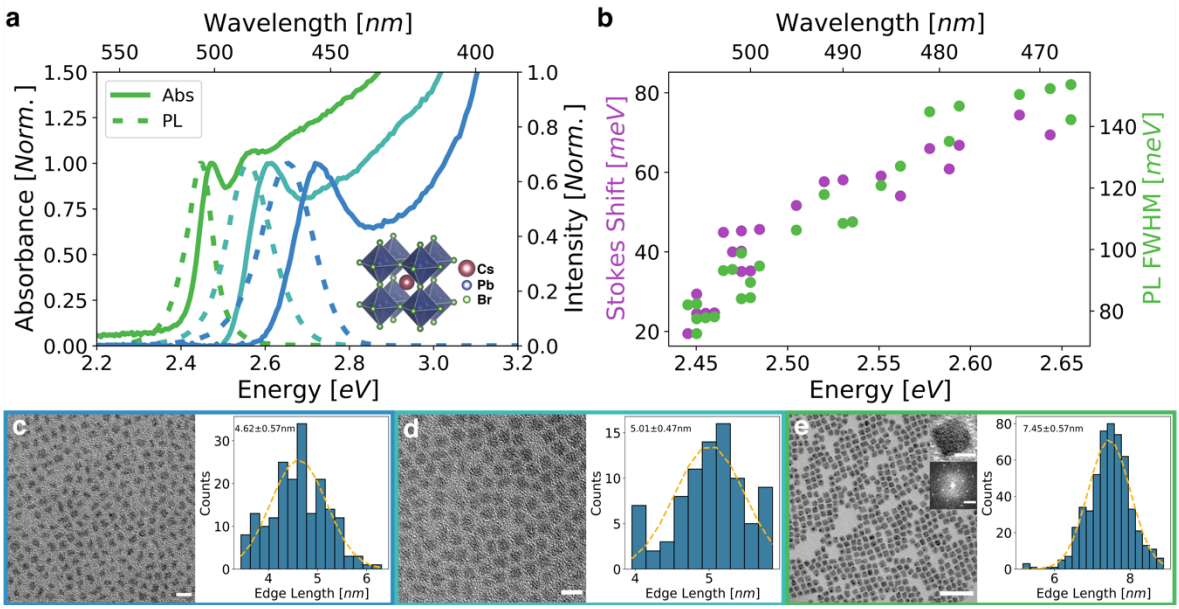


Figure 5.1: Optical and structural characterizations of $CsPbBr_3$ nanocrystals with varying sizes. a, steady-state absorption, and photoluminescence (PL) spectra of selected nanocrystals in weak, intermediate, and strong quantum confinement regime, with inset showing the crystal structure created with Vesta[38]. **b**, Stokes shift and full width at half max as a function of bandgap energy are plotted displaying a linearly increasing trend as nanocrystal sizes decrease. **c**, **d**, **e** are transmission electron microscope (TEM) images along with their corresponding size distributions fitted with gaussian curve to extract the average nanocrystal size. TEM images scale bars are as follow: **c,** 10 nm, **d**, 10 nm, and **e**, 50 nm with inset showing high resolution TEM of a single nanocrystal with 5 nm scale bar and its corresponding Fast Fourier Transform (FFT) with 2 nm^{-1} scale bar.

Each synthesized nanocrystals underwent characterization to determine photoluminescence quantum yield (PLQY) and time-resolved photoluminescence (TRPL) to quantify the radiative lifetime (τ_r), which is inversely related to the radiative rate (κ_r), using the following relation:

$$PLQY = \frac{\frac{1}{\tau_r}}{\frac{1}{\tau_r} + \frac{1}{\tau_{nr}}} = \frac{\frac{1}{\tau_r}}{\frac{1}{\langle\tau\rangle}} \tag{1}$$

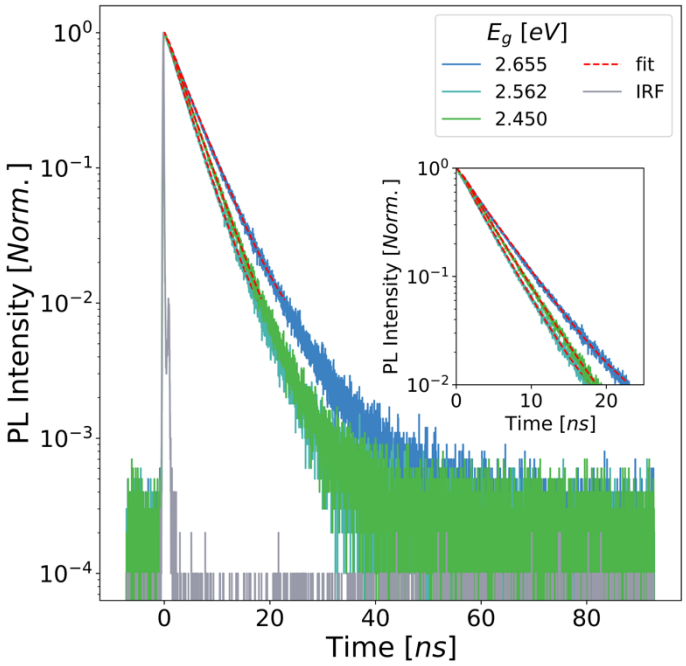
$$\tau_r = \frac{\langle\tau\rangle}{PLQY} \tag{2}$$

$$\kappa_r = \frac{1}{\tau_r} \tag{3}$$

where $\langle\tau\rangle$ is total lifetime extracted by deconvoluting with the instrument response function (IRF) and subsequentially fitting the initial two decades of TRPL decays, as shown in Figure 5.2, using a monoexponential function as follow:

$$I(t) = \int_{\infty}^{t} IRF(t') * A\, e^{-\frac{t-t'}{\tau}}\, dt' \tag{4}$$

The tabulated data in Figure 5.2 shows the near-unity PLQY $CsPbBr_3$ nanocrystals across the three confinement regimes. Notably, the strongly and weakly confined nanocrystals exhibit longer radiative lifetime (or slower radiative rate) compared to the intermediately confined nanocrystals.



E_g [eV]	2.655	2.562	2.450
PLQY [%]	94±3	100±3	90±3
τ [ns]	4.515±0.014	3.386±0.01	3.889±0.010
κ_r [ns^{-1}]	0.209±0.006	0.295±0.008	0.231±0.007

Figure 5.2: Time-resolved photoluminescence (TRPL) characterization. Three selected nanocrystals sizes in strong, intermediate, and strong quantum confinement regimes are assessed using TRPL. Decays are deconvoluted with instrument response function (IRF) and the initial two decades are fitted to a monoexponential function to extract the total lifetime (inset). Absolute photoluminescence quantum yield (PLQY) was measured to calculate the radiative rates for each nanocrystals. The resulting data, including bandgap (E_g), PLQY, total lifetime, and radiative rate, are tabulated, revealing a non-monotonic trend that emerges in lifetimes and radiative rates. Lifetime with their residual and goodness of the fit is illustrated in Figure D2.

We conducted further measurements of PLQY and TRPL across different nanocrystal sizes within each of the three confinement regimes under ambient conditions. Surprisingly, our findings reveal a non-monotonic trend in both radiative lifetime and radiative rate, as shown in Figure 5.3a and b. We find, in confirmation of earlier reports[73], that the weakly confined nanocrystals exhibit longer radiative lifetimes that we attributed to thermally accessible dim states positioned above the lowest

bright state. However, our measurements on strongly confined nanocrystals unexpectedly display similar long radiative lifetimes. Interestingly, we observe the shortest radiative lifetimes within the intermediate confinement regime. Thus, there exists some optimal nanocrystal size for applications where fast radiative recombination is desirable.

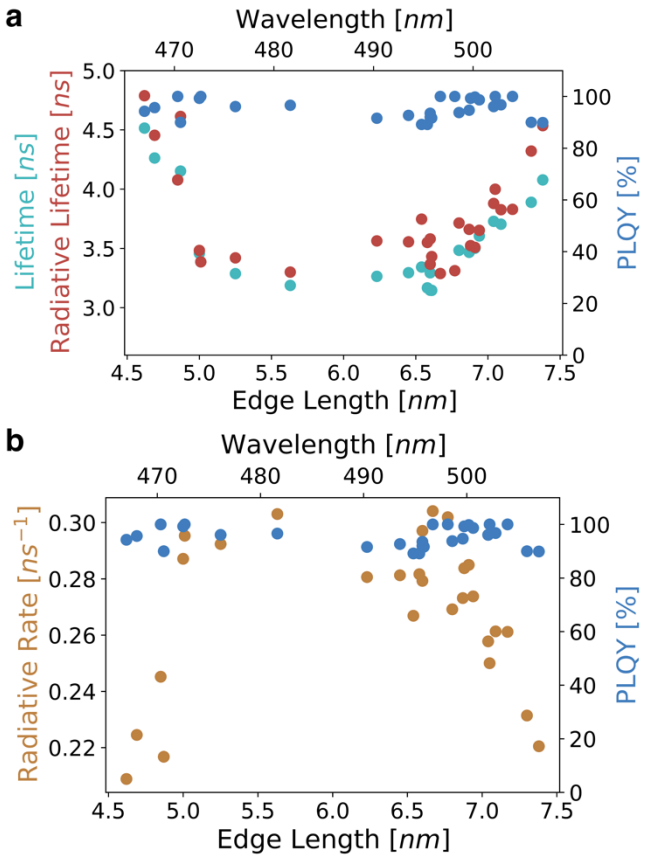


Figure 5.3: Size-dependent exciton radiative lifetimes and rates of $CsPbBr_3$ nanocrystals. a, Measured total lifetime under ambient conditions along with calculated radiative lifetimes via the absolute photoluminescence quantum yield (PLQY) as a function of nanocrystal size exhibit an unexpected non-monotonic trend. Larger nanocrystals in weak confinement regime show lengthened radiative lifetimes that decrease as the nanocrystal size transition into the intermediate confinement regime. Surprisingly, the trend reverses with decreasing nanocrystals size reaching the strong confinement regime. **b**, radiative rates, the inverse of radiative lifetimes, showcasing an optimal size associated with maximum radiative rate. Larger sizes shown in Figure D3.

To understand the underlying factors that may contribute to the lengthened radiative lifetime, we delved into a comprehensive examination of the crystal structure. In Figure 5.4a, the powder X-ray diffraction (XRD) patterns of the nanocrystals with sizes spanning the three confinement regimes are illustrated. The nanocrystals in the strong confinement regime exhibits a cubic phase. As the size of the nanocrystals increases, a transition into an orthorhombic phase is observed[74–78]. This phase transition, as discussed below, is further corroborated by molecular dynamics (MD) simulations at 300 K, as shown in Figure 5.4b.

The LAMMPS software package was used to perform MD simulations of $CsPbBr_3$ nanocubes of sizes ranging from <2 – 6 nm at 300 K using a previously parameterized force field[86]. Simulations were equilibrated for 800 ps and statistics collected for 9 ns with a 1 fs timestep, and the average structural symmetry was computed to resolve the size-dependent phase behavior. To produce a quantitative metric of the structural symmetry, we define an order parameter, ξ, that distinguishes the common cubic and orthorhombic phases of $CsPbBr_3$ nanocrystals. The order parameter is defined on the probability distribution of nearest neighbor halide-halide-halide (X-X-X) angles of the nanocrystal configuration,

$$\xi_i(\theta) = \frac{(P_i(\theta) - P^{\circ}_{cubic}(\theta))^2}{(P^{\circ}_{ortho}(\theta) - P^{\circ}_{cubic}(\theta))^2} \tag{5}$$

where $P_i(\theta)$ is the probability of finding an X-X-X angle of θ in the i-th configuration and $P^{\circ}(\theta)$ is the probability of observing angle θ in a perfectly symmetric structure. If the configuration along the MD trajectory possesses cubic symmetry, then the numerator is zero and the order parameter becomes zero. If the configuration is orthorhombic, the ratio of terms is unity, and the order parameter is one. The average order parameter for a certain size is, $\xi(\theta) = \frac{1}{N_{traj}} \sum_i \xi_i(\theta)$, where N_{traj} is the number of configurations in the trajectory. Simply, we compare the simulated geometry of the nanocrystal against perfectly cubic and orthorhombic nanocubes of the same size.

The probability distribution of X-X-X angles distinguishes strongly between cubic and orthorhombic $CsPbBr_3$ at two angles, 60º and 160º. For perfectly cubic perovskites, 1/6th of the angles is 60º while, contrastingly, zero angles are 60º for perfectly orthorhombic structures. This is reversed at 160º, where perfectly cubic structures have 0% probability and orthorhombic structures have a 1/6th probability. Figure D4 shows histograms illustrating the probabilities, allowing for a clear distinction of certain angles that specifically emerge in one phase but are absent in the other. We develop a composite measure of the size-dependent phase behavior of perovskite nanocrystals in our simulations by averaging $\xi(60°)$ and $\xi(160°)$:

$$\xi = \frac{\xi(60°) + \xi(160°)}{2}. \tag{6}$$

As evident in Figure 5.4b, the smaller nanocrystals, characterized by strong quantum confinement, display a cubic phase. As the nanocrystals size increases, a transition occurs, with the phase progressively shifting towards orthorhombic symmetry – results that closely align with the experimental XRD patterns shown in Figure 5.4a. MD simulations were also performed on analogous $CsPbI_3$ perovskite nanocrystals and a similar phase behavior observed. Comparative analysis of the size-dependent anisotropy for $CsPbBr_3$ and $CsPbI_3$ nanocrystals are presented in Figure D5.

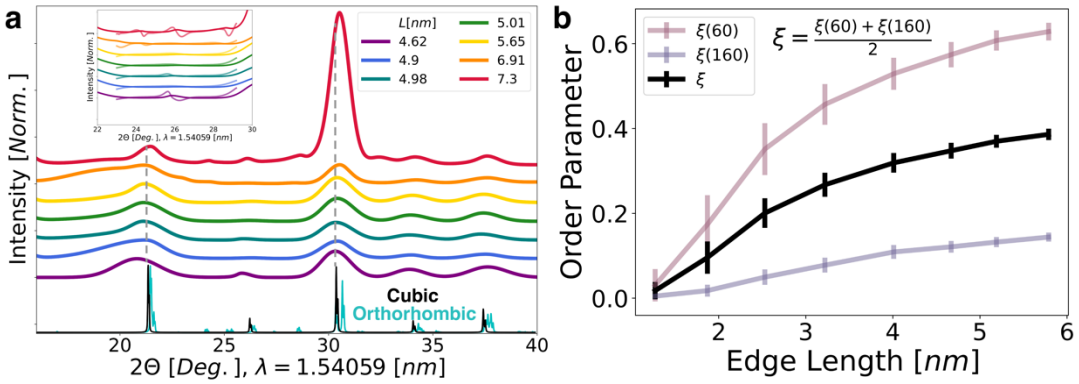


Figure 5.4: X-ray diffraction (XRD) and molecular dynamics (MD) of varying $CsPbBr_3$ nanocrystal sizes. a, XRD patterns illustrating the transition from cubic to orthorhombic symmetry. **b**, a composite order parameter that assesses the degree of crystal phase computed from MD simulation trajectories under ambient conditions in reference to a perfect cubic and orthorhombic symmetry, where 0 indicates a cubic phase and 1 means an orthorhombic phase. Error bars denote the variance of the order parameter due to fluctuations in the geometry over the simulation. The order parameter results align with XRD patterns, confirming the size-dependent phase transition from being cubic in small nanocrystals to orthorhombic in larger nanocrystals.

Further theoretical understanding of the interplay between perovskite structural and optical properties was gained by performing electronic structure calculations on the relaxed structures for varying nanocrystal sizes. Accurate excited states including electron-hole correlation and spin-orbit coupling effects were computed within the semi-empirical pseudopotential framework as described in previous reports[87]. We obtain a validated pseudopotential from Weinberg et al. describing local, nonlocal and spin-orbit coupling effects for $CsPbI_3$[87]. The electronic properties of $CsPbI_3$ and $CsPbBr_3$ show analogous trends[88]; thus, we compute radiative lifetimes using the validated $CsPbI_3$ model as a proxy to understand the measured $CsPbBr_3$ radiative lifetimes.

Due to computational constraints, the investigation of nanocrystal sizes spans strongly and intermediately confined nanocrystals with sizes ranging from 3.1 – 5.7 nm. In addition, we relax nanocrystal structures at 0 K using a conjugate gradient approach to obtain static input geometries. It was verified that the 0 K structures show the same size dependent phase behavior as the 300 K MD simulations (see Figure D4). This gives us three structures to compare for each size: cubic, orthorhombic, and relaxed.

We calculated the radiative lifetime in the time-dependent perturbation theory framework as:

$$\tau_r = \frac{1}{\kappa_r} = \sum_n e^{-\beta E_n} \frac{3\pi\varepsilon_o \hbar c^3}{{\omega_n}^3 |\mu_n|^2} \tag{8}$$

where $\varepsilon_o, \hbar, c$ are the vacuum permittivity, reduced Planck's constant, and speed of light, respectively. The parameters ω_n and $|\mu_n|^2$ correspond to the transition frequency and the oscillator strength of exciton n. Reported radiative lifetimes are the Boltzmann thermal average of excitons within $3\kappa_B T$ of the lowest exciton. We assume that the timescale of radiative recombination is faster than relaxation to the ground state and do not include the lowest exciton in our Boltzmann

average. This procedure produces radiative lifetimes that agree well with experiments. A reduction in radiative lifetime is observed as nanocrystal size increases from the strongly confined to intermediately confined regime (Figure 5.5a). We rationalize this decrease in radiative lifetime by analyzing the size-dependent oscillator strength of states within $3\kappa_B T$ of the lowest bright exciton. We find a drastic increase in the lowest bright state's oscillator strength as the nanocrystal size increases, independently of crystal symmetry (Figure 5.5b). While one might expect a further decrease in radiative lifetime due to the increase in the oscillator strength, an interesting lengthening in radiative lifetime occurs. New states exhibiting weak oscillator strength (i.e. dim states) within $3\kappa_B T$ emerge, which under ambient conditions, mix with the lowest bright state. This mixing of states leads to an extension of radiative lifetimes in larger nanocrystals that results in non-monotonicity in the radiative lifetime as observed for the largest calculated nanocrystals, shown in Figure 5.5a. To examine how temperature influences of this mixing, we computed the radiative lifetimes at lower temperatures (Figure D6). Our analysis reveals an exponential decrease as nanocrystals size decrease at lower temperatures, indicating that the dim states become thermally inaccessible. This observed exponential trend aligns closely with previously reported experimental findings[26,72]. It is noteworthy to point that the competing effects of weakened oscillator strength and dim state mixing occur distinctly for the strong and weak confinement regimes, respectively, leaving the intermediate confinement regime to exhibit the shortest radiative lifetime. This aligns well with the experimentally observed non-monotonic trend in size-dependent radiative lifetime in $CsPbBr_3$ nanocrystals, shown in Figure 5.3. Additionally, this rationalization explains the trend we predict to be common among prototypical II-VI (CdSe, Figure D7) , III-V (InP, Figure D8), and perovskite semiconducting nanocrystals[70].

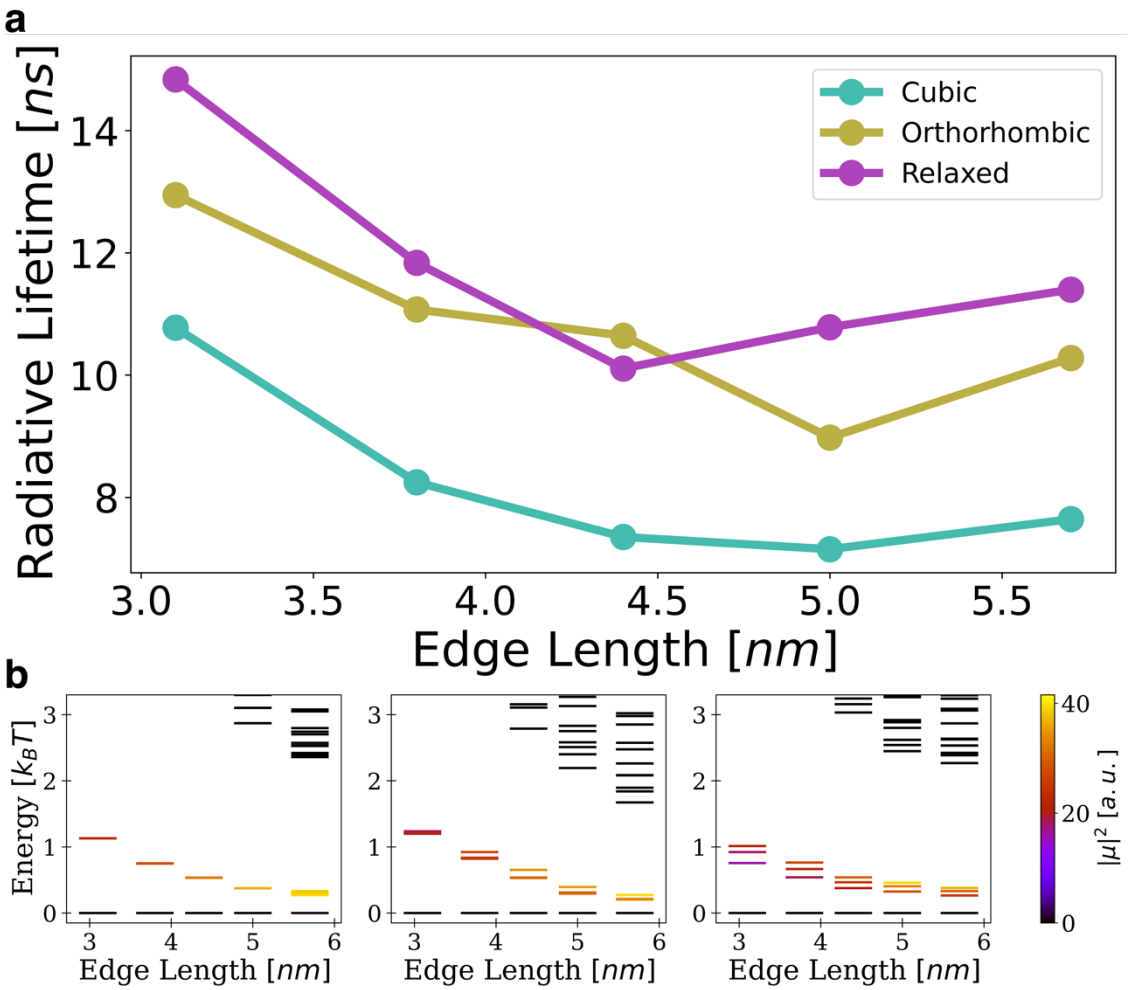


Figure 5.5: Size-dependent radiative lifetimes calculation. a, radiative lifetimes computed through electronic structure calculations on perfect cubic and orthorhombic symmetries along relaxed structure with varying nanocrystal sizes. **b**, Calculated excitonic states as a function of nanocrystal size plotted for cubic, orthorhombic, and relaxed structure. Here states within $3\kappa_B T$ above the lowest exciton levels are included. Color map indicates oscillator strength, which happens to increase for the lowest bright exciton with increasing nanocrystal size.

5.3 Conclusion

In conclusion, the investigation of the effect of $CsPbBr_3$ nanocrystal size on radiative lifetime reveals an unexpected non-monotonic trend. Larger and smaller nanocrystals in the weak and strong quantum confinement regimes displayed longer radiative lifetimes, leaving the intermediately confined nanocrystals to exhibit the shortest radiative lifetimes. This non-monotonicity in radiative lifetime appears to be a common trend among II-VI (CdSe), III-V (InP), and perovskites semiconducting nanocrystals. Interestingly, we observed a phase transition from cubic and orthorhombic symmetry that was confirmed by X-ray diffraction and MD simulations. This transition coincided with the intermediate confinement regime, but we find no evidence suggesting its influence on radiative lifetimes. Further analysis revealed that large nanocrystals in

the weak confinement regime showed extended radiative lifetime due to the thermal population under ambient conditions of high-lying states with weak oscillator strengths. In contrast, the unexpected lengthening of radiative lifetime in smaller nanocrystals within the strong confined regime was attributed to a significant reduction in oscillator strength, leaving the intermediately confined nanocrystals to exhibit the shortest radiative lifetimes. This study emphasizes the intricate and unique interplay between the $CsPbBr_3$ nanocrystal size and radiative lifetime, paving the way to improve and engineer optical materials with desirable radiative lifetimes for diverse optical applications.

Chapter 6. Can Semiconductor Nanocrystals Be Laser Cooled?

6.1 Introduction

Since its inception in 1929 by Pringsheim[1], optical refrigeration or laser cooling has attracted significant attention due to its potential impact on global heating among other applications. For example, sun rays could potentially be absorbed and converted to cool the environment, which may sound counter-intuitive but that's the promise of some materials that has the potential to be used in laser cooling. Other applications that may benefit from laser cooling are in high-power laser temperature control to quantum sensing and computing[5,6,39]. Initial work since laser cooling was proposed was focused on cooling atoms through Doppler cooling mechanism, which has allowed the study of quantum mechanical behaviors at near absolute zero. However, more applications can be explored if condensed matters or solid-state materials can be cooled. Not until 1995 where the first laser cooling in solid-state materials was observed, which paved the way explore more solid-state materials[8]. Early work on solid-state laser cooling was done on rare-earth materials by which rare-earth elements were doped into glass or crystals to result in up-conversion of sub-bandgap excitation. A record net cooling of 89 K was observed in Yb^{3+}-doped yttrium lithium fluoride (YLF) crystals[9]. This cryogenic temperature is effectively the Minimum Achievable Temperature (MAT) for rare-earth-based solid-state materials because rare-earth elements' ground state maximum, being atoms, becomes depopulated at low temperature since it follows Boltzmann statistics, reducing the possibility of up-conversion[10]. Thus, semiconductor materials were sought for laser cooling since they follow Fermi-Dirac statistics in which the maximum of the valence band remains populated even at absolute zero, allowing a MAT of <10 K[10]. At first, bulk GaAs semiconductor was studied for laser cooling and after significant research, bulk semiconductors have not shown any net cooling[13]. Therefore, major work has been focused on colloidal nanocrystals and nanostructure due to their promising potential to be laser cooled. Some work on CdS nanobelts and perovskite platelets have shown the first net cooling for solid-state laser cooling; however, the results were controversial but did not invalidate the possibility to laser cool semiconductors[4,11,14,89,90].

Among semiconducting nanomaterials candidates for laser cooling[5], cesium lead bromide ($CsPbBr_3$) perovskite nanocrystals have emerged as a highly promising nanomaterial owing to their ease of synthesis, near-unity photoluminescence quantum yield (PLQY), and substantial up-conversion efficiencies[5,15,17]. Notably, $CsPbBr_3$ nanocrystals exhibit a remarkably low trap density and can tolerate shallow surface defects, which contribute to their near-unity PLQY[19,28,29]. Extremely high PLQY (>99%) is essential to observe net laser cooling[5]. Attainment of laser cooling in semiconductors depends on two sequential processes: efficient up-conversion, where a phonon is annihilated upon sub-bandgap light absorption to arrive at an excited state population; and anti-Stokes photoluminescence (ASPL), where the emitted photon energy is higher than that of the excitation electron. Once an electron undergoes up-conversion to arrive at the conduction band edge, competition between radiative and non-radiative decay pathways determines whether

net cooling is observed in solid-state semiconductor materials[12,13]. Radiative emission without generation of a phonon leads to an overall reduction in phonon population (reducing phonons = cooling), while non-radiative recombination results in phonon generation. Thus it is imperative to shorten the radiative lifetimes, inversely increase the radiative rates, to reduce the non-radiative recombination probability. With previous chapters discussing in great details regarding optimizing the radiative lifetimes as well as rigorous investigations of up-conversion process and efficiency with perovskite nanocrystals, this chapter focuses on attempts to laser cool perovskites and other nanocrystals such as II-VI (Cadmium Selenide, CdSe). We specifically set up a technique that can measure change in temperature of the nanocrystal directly instead of relying on spectral signatures such as Raman signals as has been done previously, which resulted in ambiguous results[4,11,14,89]. Figure 6.1 illustrates the laser cooling experimental setup. Briefly, a narrow bandwidth laser with sub-bandgap energy is directed onto the sample that is encapsulated with a thermally insulating glass cuvette. A sensitive thermal camera is placed in close proximity to the sample to detect any temperature change within $\pm$0.1 ℃. With different ~100% PLQY samples configured in solution phase, encapsulated thin film, polymer matrix, aerogel, and under low pressure as well as different sub-bandgap laser excitation, no net laser cooling was observed yet. We suspect that environment, whether glass cuvette, solution or polymer are potentially the cause of parasitic heating. Some measurements showed almost zero change in temperature, indicating the potential to overcome any parasitic heating, and toward achieving true net laser cooling in semiconductor nanocrystals. Next promising set up is to completely eliminate the surrounding by suspending the nanocrystals in a self-assembled configuration on and measure the superlattice oscillation with a resonance frequency as a function of temperature[91].



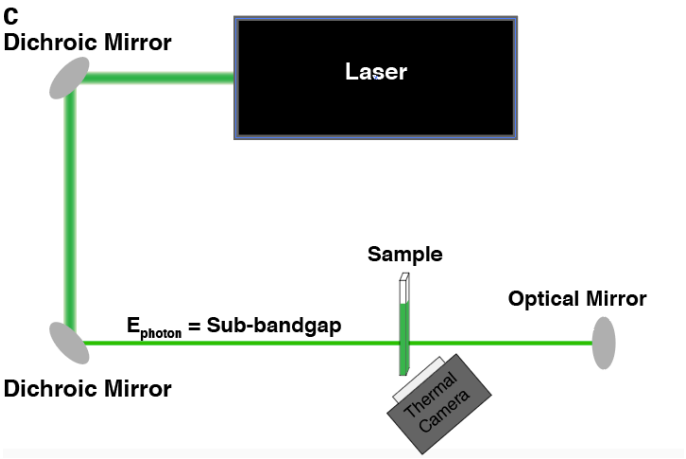


Figure 6.1: Direct laser cooling measurement setup. (a) Front and (b) side views of the optical table where the laser cooling measurements are conducted. (c) Schematic showing the laser path to the sample that is also getting back reflected by an optical mirror along with a sensitive thermal camera in close proximity to the sample to detect any temperature change.

6.2 Results & Discussion

As discussed in the introduction chapter, a critical photoluminescence quantum yield (PLQY) must be met before a net laser cooling can be achieved. For $CsPbBr_3$, this critical PLQY is 99.0-99.1%. Thus, it is imperative to produce nanocrystals as close to 100% as possible to leverage any cooling power. Taking the best synthesis procedure developed and optimized for $CsPbBr_3$ nanocrystals, near-unity, ~100%, PLQY was measured with an integrating sphere. Figure 6.2 show steady state absorption and photoluminescence (PL) spectra with emission at 509 nm along with PLQY measurement and transmission electron microscopy (TEM), illustrating a highly monodispersed ensemble.

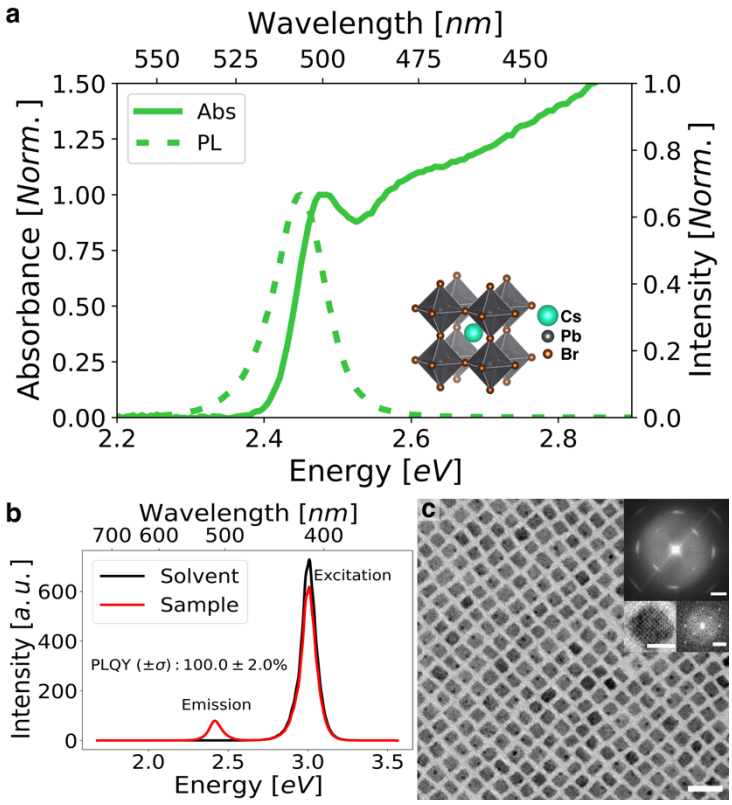


Figure 6.2: Optical and structural characterizations of $CsPbBr_3$ nanocrystals. a, steady-state absorption and photoluminescence (PL) spectra, with inset illustrating the crystal structure made with Vesta[38]. b, Near-unity photoluminescence quantum yield (PLQY) measurement. c, Transmission electron microscopy (TEM) image shows highly monodispersed nanocrystals and top inset shows the corresponding Fast Fourier Transform (FFT) (scale bars 20 nm and 1 nm^{-1}, respectively). Bottom insets show high-resolution TEM image of a single nanocrystal with its corresponding FFT (scale bars 5 nm and 2 nm^{-1}, respectively).

With such high-quality nanocrystals on hands, we ran several measurements as will be outlined next. Concentrated nanocrystals in toluene were added to a thin glass cuvette with low thermal conductivity and was encapsulated. A sub-bandgap 532 nm green laser was aligned on the sample in cuvette as shown in Figure 6.3a and the thermal camera positioned and focused on the sample. Different laser powers were selected, 1.5 W, 2 W, and 5 W. Initially, with laser blocked (OFF), the sample was let to thermally equilibrate as shown in Figure 6.3b, c and d. Then, the laser at the aforementioned powers was unblocked (ON) for 1-3 min to observe temperature change. Looking at the cross-hair spot (Cen=Center), we see that for 1.5 W, 2 W, and 5 W a temperature change of $\Delta T = 1.5\ ℃, 1.8\ ℃$ and $3.9\ ℃$ occurred, respectively. Therefore, only net heating observed with this set of measurements.

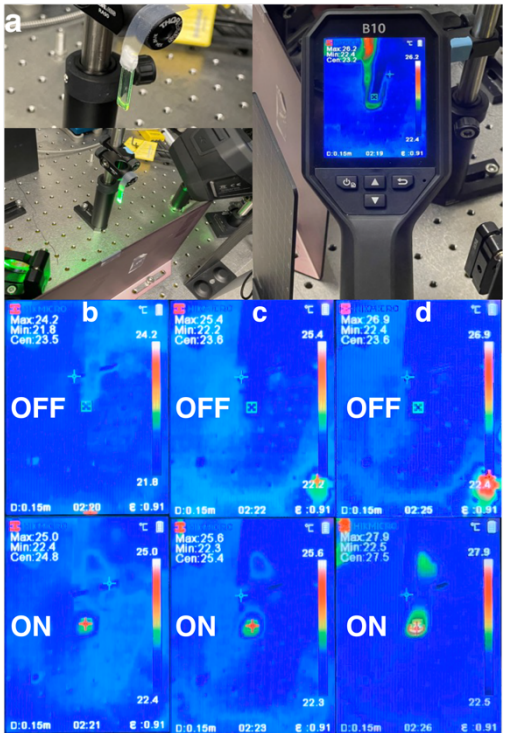


Figure 6.3: Laser cooling measurement with thermal camera and 532 nm sub-bandgap laser. (a) sample and thermal camera set up. (b) 1.5 W, (c) 2 W, and (d) 5 W laser power was blocked (OFF) until the sample is stabilized, then the laser was unblocked (ON) and temperature change was observed. We see a new heating of $\Delta T = 1.5$ ℃, 1.8 ℃ and 3.9 ℃ for 1.5 W 2 W, and 5 W, respectively.

We tested toluene in cuvette to rule out any potential parasitic heating, as shown in Figure 6.4. With 5 W laser power, we found that the toluene in cuvette heated up to 3.0 ℃, indicating that, if we compare to the measurement in Figure 6.3d, the sample heated by 0.9 ℃, which is quite low considering the potential heating of one non-radiative event with heating energy corresponding to the $CsPbBr_3$ sample bandgap of 2.435 eV.

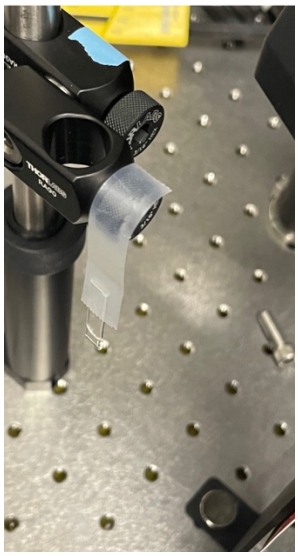


Figure 6.4: Pure toluene solvent. With clean cuvette with just toluene solvent, the laser power was set to 5 W to resemble the measurement in Figure 6.3d. We found that the toluene in cuvette heated up to 3.0 ℃.

To avoid solvent effect, we completely vacuum dried the nanocrystal solution, which left a thin film that is encapsulated. We ran the same measurement at 5 W power, and we measured $\Delta T = 1.3$ ℃, slightly more than $\Delta T = 0.9$ ℃ we anticipated. We attributed that to the fact that drying the nanocrystal into solid forms a condense film. Self-reabsorption increases which potentially could result in non-radiative recombination that compete with radiative recombination since the nanocrystals are not exactly 100%.

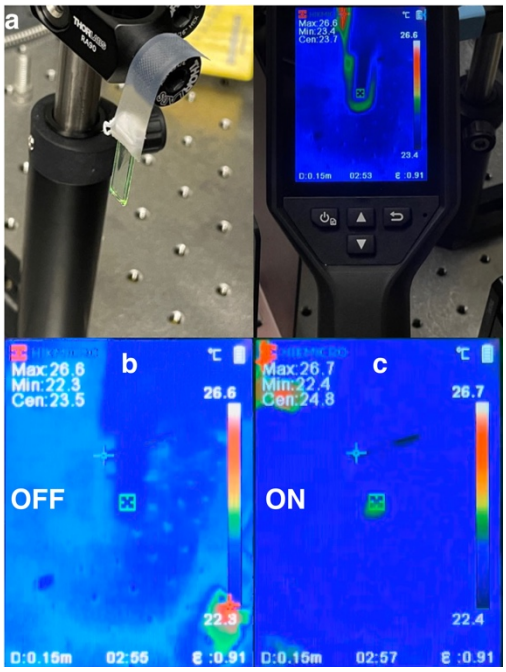


Figure 6.5: An encapsulated thin film. (a) sample that has been fully vacuum dried into a thin film. 5 W 532 nm laser (b) OFF and (c) ON resulted in a temperature change of $\Delta T = 1.3$ ℃.

We then wanted to avoid using the glass cuvette as it is relatively thick and would require significant cooling or heating power from the nanocrystals to observe effect with the thermal camera. So, we reverted to using a thin glass coverslip. Initially, we tested, with 532 nm at 5 W power, a single bare coverslip, as shown in Figure 6.6. We observed a $\Delta T = 0.4$ ℃ (Figure 6.6b and d).

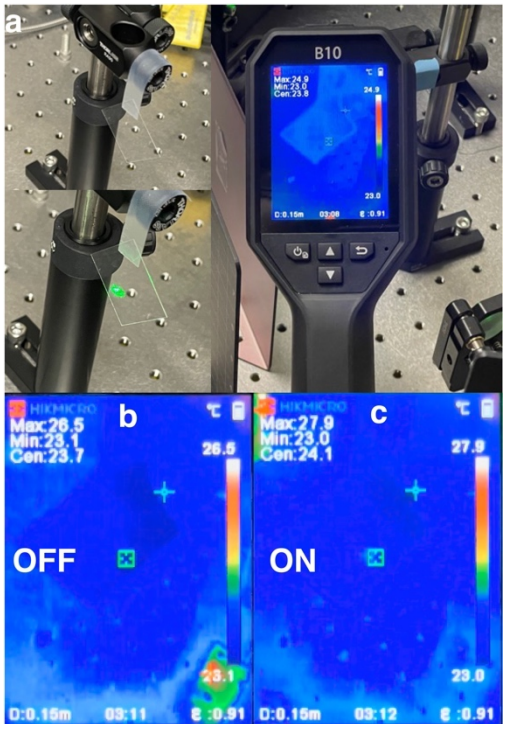


Figure 6.6: Bare coverslip. (a) clean bare glass coverslip. 5 W 532 nm laser (b) OFF and (c) ON resulted in a temperature change of $\Delta T = 0.4$ ℃.

With coverslip heating with 0.4, we sandwiched a dropcasted thin film nanocrystals between two glass coverslips and sealed the edges with epoxy to avoid air exposure (Figure 6.7a). With 5 W power, we observed a net heating of $\Delta T = 3.7$ ℃, where we assume 0.8 ℃ was added from the two coverslips. We also suspect the nanocrystals degraded as they might have gotten mixed with some epoxy during the sample preparation.

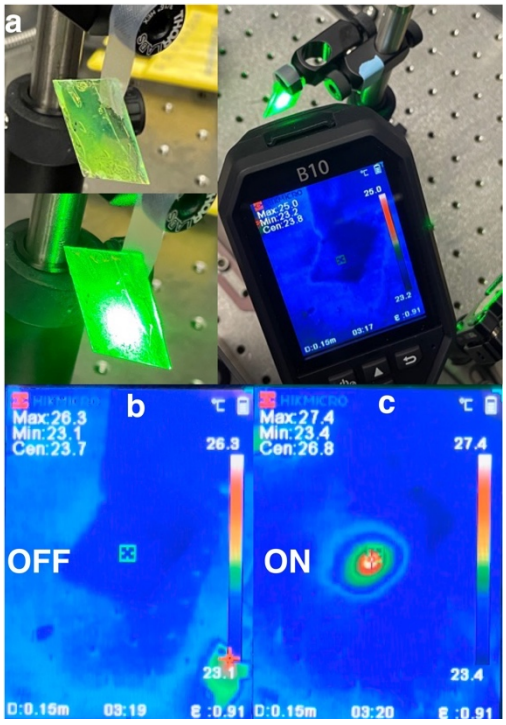


Figure 6.7: Nanocrystals thin film sandwiched by two glass coverslips. (a) nanocrystals thin film between two glass coverslip. 5 W 532 nm laser (b) OFF and (c) ON resulted in a temperature change of $\Delta T = 3.7$ ℃.

So, to avoid using epoxy and cover slips, we prepared a polymer matrix. The matrix consists of 5 wt% polystyrene previously dissolved in toluene then mixed with nanocrystals. The mix was then dropcasted and solvent was allowed to evaporate naturally to form a uniform polymer-nanocrystals film. We also prepared a plain polymer film to test for any parasitic heating (Figure 6.8). The plain polymer film heated to $\Delta T = 1.8$℃ with 5 W 532 nm laser. Unexpectedly, the polymer-nanocrystals mix shown in Figure 6.9, when excited with the 532 nm at 5 W was heated intensely and net roughly $\Delta T = 117.5$ ℃, which left the film with a burned hole (Figure 6.9e). We attributed this large heating to the fact that the nanocrystals in the polymer matrix were not fully encapsulated and were exposed to the outside environment, degrading them, and lowering their quantum yield.

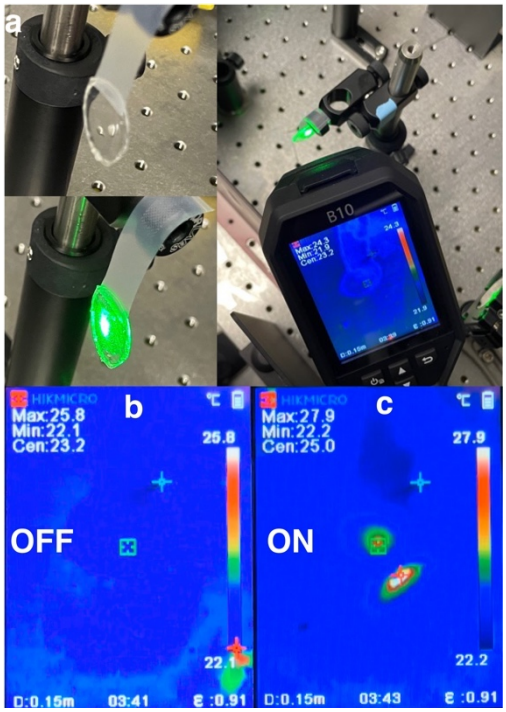


Figure 6.8: Polystyrene film. (a) Polystyrene film prepared as 5 wt% in toluene and dropcasted and allowed to dry naturally. 5 W 532 nm laser (b) OFF and (c) ON resulted in a temperature change of $\Delta T = 1.8$ ℃.

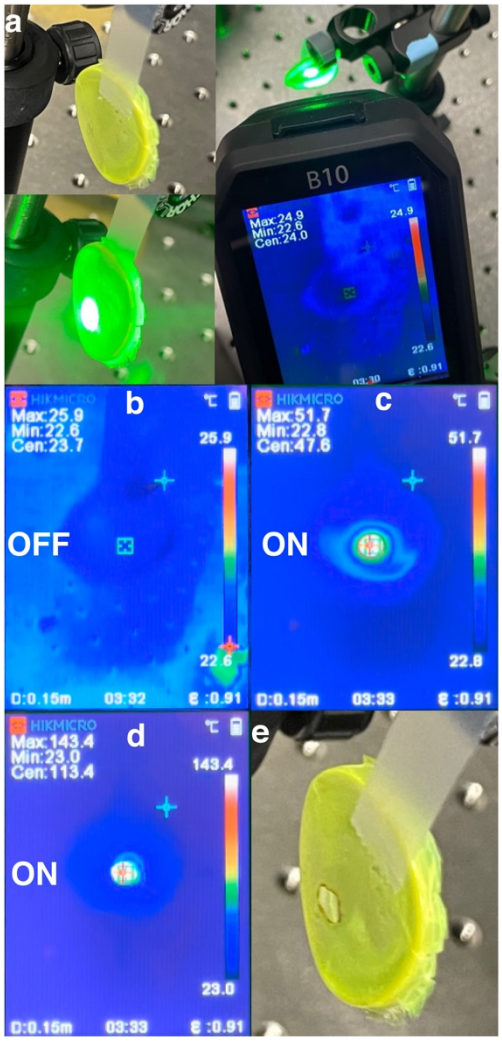


Figure 6.9: Polymer-nanocrystals matrix film. (a) Nanocrystals was mixed with prepared polystyrene in toluene and dropcasted and allowed to dry naturally. 5 W 532 nm laser (b) OFF and (c, d) ON resulted in a temperature change of $\Delta T = 117.5$ ℃. (e) Due to the high temperature generated from the polymer-nanocrystals matrix, the film was burned through.

We retested the nanocrystals in solution in the thin glass cuvette with 532 nm at different power to track the timescale at which these heating occurs. As evident in Figure 6.10, we see a consistent 50-55 seconds at which net heating plateau which is acceptable considering the nanocrystals, which is expected to heat or cool within in the milliseconds range[14], transfer its heat to the surrounding.

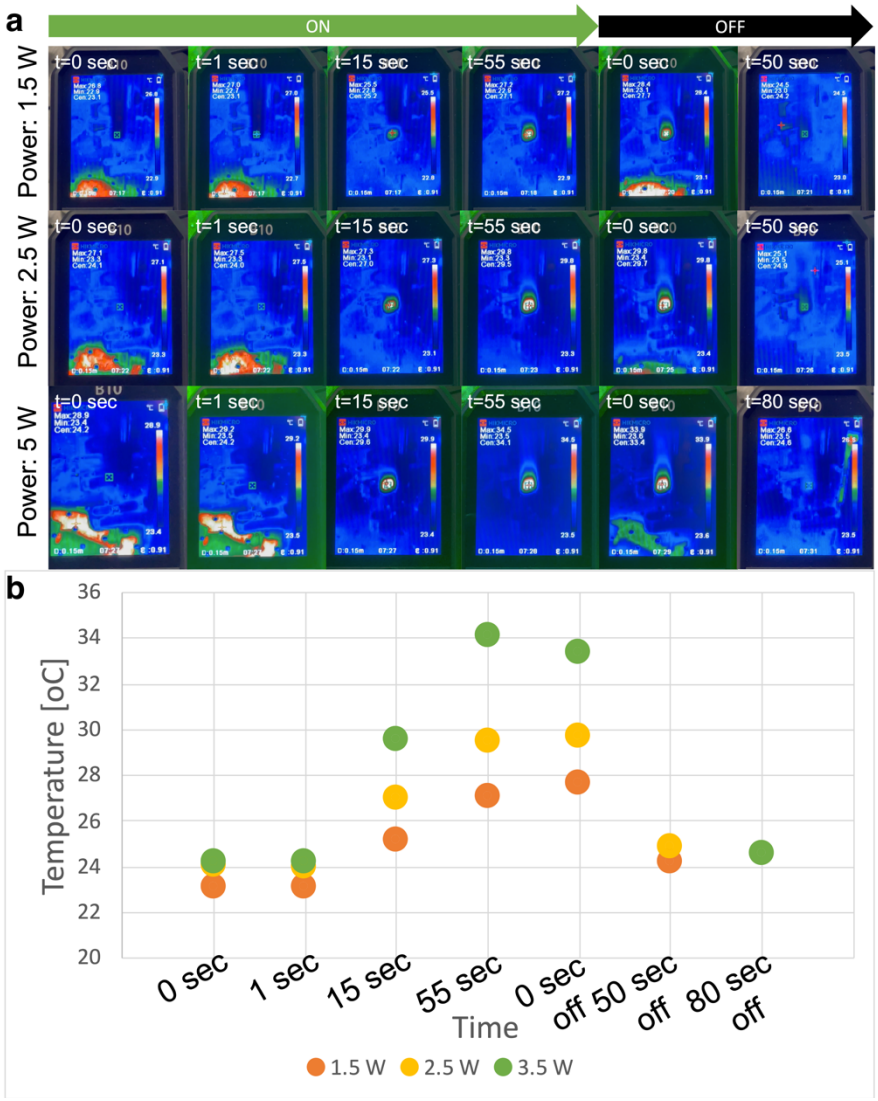


Figure 6.10: Sub-bandgap excitation over time. (a) Laser cooling measurements with 532 nm laser at different power, 1.5 W, 2 W, and 5W over time. (b) Detected temperature change over time illustrates the fast and consistent increase in temperature for different laser power.

Since with all the discussed attempts thus far produced net heating, we attributed it to the fact that the 532 nm laser is detuned relatively deep in the bandgap with up-conversion efficiencies in the 10-20% as discussed in previous chapters. Since the 532 nm laser is generated through second-harmonic generation (SHG) from a 1064 nm laser, we suspect that some 1064 nm photons leaked through even though we used two dichroic mirrors (Figure 6.1c) to transmit most of the infrared light. Thus, we shifted the laser cooling experiments by using a 520 nm diode laser with power up to 1 W. Figure 6.11 shows the attempt results with the new laser set to 0.9 W, and we observed a net heating of $\Delta T = 0.9$ ℃, which is quite small, showing a promise for laser cooling the perovskite nanocrystals.

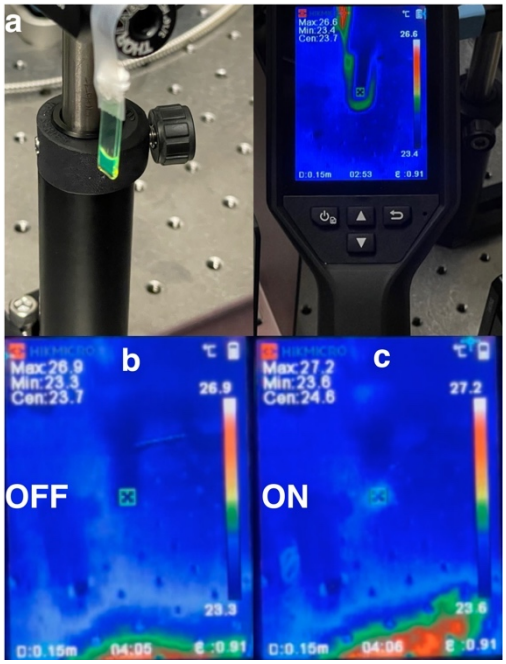


Figure 6.11: Laser cooling measurement with thermal camera and 520 nm sub-bandgap diode laser. (a) sample and thermal camera set up.0.9 W laser power was blocked (a) OFF until the sample is stabilized, then the laser was unblocked (b) ON, and temperature change was observed. We see a heating of $\Delta T = 0.9$ ℃.

To avoid solvent and glass cuvette that would require the nanocrystals to transfer its heating or cooling energy to, we tried using an aerogel film that we dropcasted a drop of nanocrystals solution. At first, we tested a bare aerogel with the new 520 nm diode laser. Surprisingly, there was some heating even though there should not be anything absorption the laser. Figure 6.12 shows that the bare aerogel heated to $\Delta T = 4.2$ ℃ when the 520 nm laser power is set to 0.9 W.

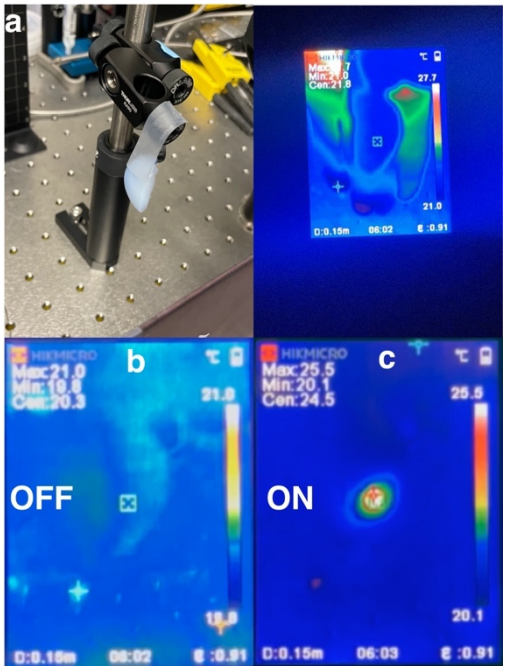


Figure 6.12: Bare aerogel film for laser cooling measurement. (a) aerogel film purchased from Aerogeltechnologies. 0.9 W 502 nm diode laser (b) OFF and (c) ON resulted in a temperature change of $\Delta T = 4.2$ ℃.

We then dropcasted the nanocrystals onto the aerogel film and tested for laser cooling. Although we observed minimal heating of $\Delta T = 0.9$ ℃ under the exact conditions as in Figure 6.12, potentially the nanocrystals were actually able to cool the aerogel by $\Delta T = 3.3$ ℃. Figure 6.13 shows the measurement of nanocrystals in aerogel by which possible cooling was observed.

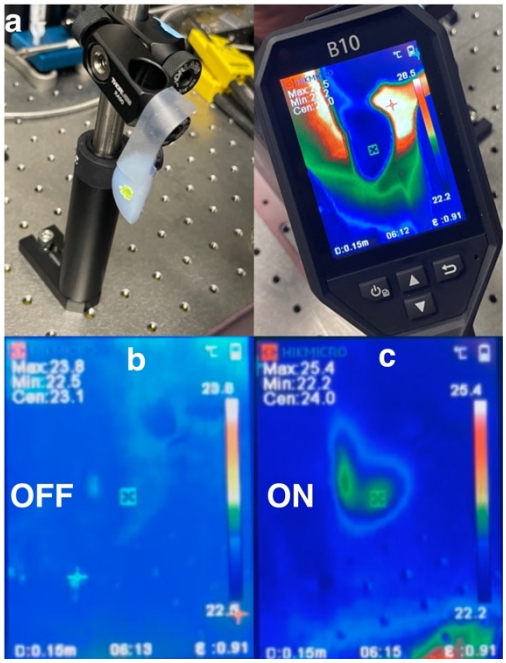


Figure 6.13: Nanocrystals in aerogel film. (a) nanocrystal dropcasted on aerogel film. 0.9 W 502 nm diode laser (b) OFF and (c) ON resulted in a temperature change of $\Delta T = 0.9$ ℃. If compared to bare aerogel, potentially we observed a cooling of $\Delta T = 3.3$ ℃.

All the attempts thus far were done under atmospheric pressure. To eliminate any potential effect from any air flow, we attempted laser cooling under low pressure, in a cryostat with pressure down to 10^{-7} Pa. We prepared a thin film dropcasted on a glass coverslip as well as dried film of nanocrystals in a glass cuvette as shown in Figure 6.14 and 6.15.

We first tested the thin film on glass cover slip (Figure 6.14) with the 520 nm diode laser at 0.9 W. We observed a net heating of $\Delta T = 77.6$ ℃ that it burned a hole through the glass coverslip (Figure 6.14e) despite the fact that the sample was prepared under inert environment (nitrogen filled glovebox) and placed in a cryostat that was then lowered in pressure. So, we attribute this large heating to possible nanocrystals photon cycling (self-reabsorption) as the nanocrystal film was thick.

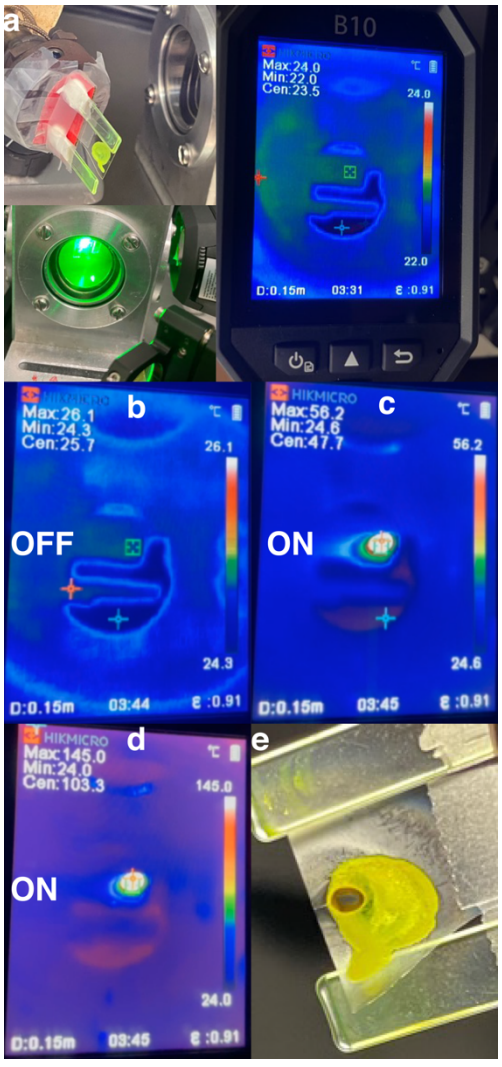


Figure 6.14: Laser cooling measurements in cryostat using coverslip. (a) nanocrystal dropcasted on glass coverslip under inert environment and was placed inside a cryostat for low pressure measurement. 0.9 W 502 nm diode laser (b) OFF and (c and d) ON resulted in a temperature change of $\Delta T = 77.6$ ℃. (e) The sample heated and burned a hole through the coverslip.

We then tested the cuvette (Figure 6.15), and a net heating of $\Delta T = 1.1$ ℃. A summary table 6.1 showing the several laser cooling configurations and attempts on perovskite nanocrystals with photoluminescence emission of 509 nm and near- unity, 100%, photoluminescence quantum yield.

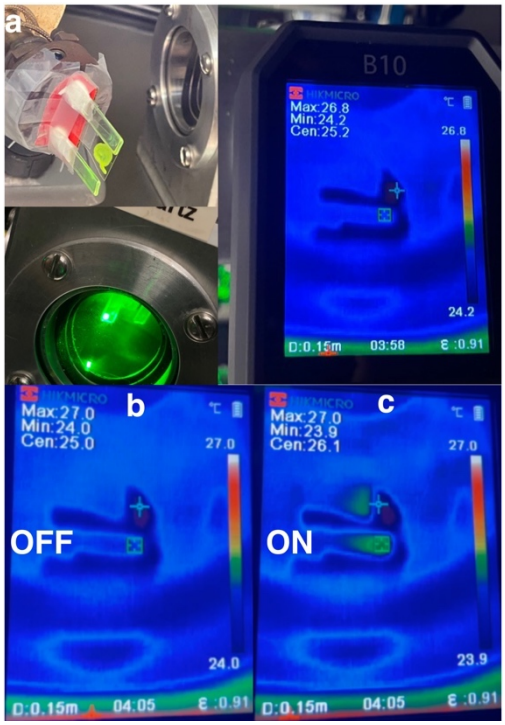


Figure 6.15: Laser cooling measurements in cryostat using thin glass cuvette. (a) nanocrystals solution was added to thin glass cuvette, vacuum dried and then placed under inert environment inside a cryostat for low pressure measurement. 0.9 W 502 nm diode laser (b) OFF and (c and d) ON resulted in a temperature change of $\Delta T = 1.1$ ℃.

Table 6.1: Summary of laser cooling measurements on perovskite nanocrystals with photoluminescence emission of 509 nm and photoluminescence quantum yield of ~100%. Boxed, in red, is a potential set f experiments that might have resulted in a net cooling.

Sample/Emission	Phase	Medium	Laser [nm]	Power [W]	ΔT [°C]
None	Toluene Solution	Tiny Glass Cuvette	532	5	3.0
ASAPO23L2/509nm	Toluene Solution	Tiny Glass Cuvette	532	1.5	1.5
ASAPO23L2/509nm	Toluene Solution	Tiny Glass Cuvette	532	2.5	1.8
ASAPO23L2/509nm	Toluene Solution	Tiny Glass Cuvette	532	5	3.9
ASAPO23L2/509nm	Thin Film	Tiny Glass Cuvette	532	5	1.3
None	None	Glass Coverslip	532	5	0.4
ASAPO23L2/509nm	Thin Film	2 Glass Coverslip	532	5	3.7
None	None	Polystyrene Film	532	5	1.8
ASAPO23L2/509nm	Thin Film	Polystyrene Film	532	5	117.5
ASAPO26L2/509nm	Toluene Solution	Tiny Glass Cuvette	520	0.9	0.9
None	None	Aerogel	520	0.9	4.2
ASAPO26L2/509nm	Thin Film	Aerogel	520	0.9	0.9
ASAPO27L2/509nm	Thin Film	1 Glass Coverslip - Cryostat	520	0.3	4.4
ASAPO27L2/509nm	Thin Film	1 Glass Coverslip - Cryostat	520	0.8	77.6
ASAPO27L2/509nm	Thin Film	Tiny Glass Cuvette - Cryostat	520	0.85	1.1

6.3 Conclusion & Future Recommendations

In conclusion, despite the tremendous investigations detailed in all chapters, including optimization, and understanding of up-conversion processes and radiative lifetimes in lead-halide perovskite nanocrystal, no conclusive evidence of laser cooling has been observed yet. In all the attempts, a special set up was developed to directly measure any temperature change using a sensitive thermal camera. Aerogel attempts might have shown a potential net laser cooling. Future work can utilize a slightly different sample configuration where the nanocrystals are made into a superlattice that are suspended to eliminate any surrounding effect (solvent, glass, polymer, etc.) and directly measure the superlattice temperature as a function of its resonance oscillation shift[91].

Appendix A

A.1 Urbach Energy

One method for quantifying absorption below the band edge (referred to as anti-Stokes absorption) involves determining the Urbach energy using the absorption coefficient relationship:

$$\alpha(hv) = \alpha_o \, e^{\left(\frac{hv - E_{pl}}{E_u}\right)} \tag{1}$$

where α is the absorption coefficient, hv is the excitation energy, E_{pl} is the band edge energy, and E_u is the Urbach energy.

Solving for α_o at the band edge is as follows:

$$I = I_o e^{-\alpha L} \tag{2}$$

$$log_{10}\left(\frac{I_o}{I}\right) = A = \alpha \, L \, log_{10}(e) \tag{3}$$

rearranging equation (3),

$$\alpha_o = \frac{A}{L \, log_{10}(e)} \tag{4}$$

where A is the absorption and L is cuvette path length (standard 1 cm). We solve for α_o at the band edge and find it to be $\alpha_o\left(A = 0.0698,\ E_{pl} = 2.436eV\right) = 0.1607\ cm^{-1}$.

Then rearranging equation (1):

$$\ln(\alpha(hv)) \propto \frac{1}{E_u} hv \tag{5}$$

We see that the Urbach energy can be extracted from the slope of the absorption coefficient as a function of excitation energy at the band tail, as shown in Figure 2.2e of the main text. We find the Urbach energy for our $CsPbBr_3$ nanocrystals to be $E_u = 30.95208617\ meV$

By utilizing the Urbach energy in conjunction with the absorption coefficient at the band edge, the anti-Stokes absorption can be derived from equation (3). Subsequently, this enables determination of the up-conversion efficiency.

A.2 Temperature Dependency of Up-Conversion Efficiency

In the main text, we examine the relationship between up-conversion efficiency and temperature. We establish that the ratio of the number of phonons (N_p) at two distinct temperatures, considering their respective phonon energies, directly correlates with the ratio of up-conversion efficiency at those temperatures. To investigate this connection, our initial step involves modeling the phonon energy as a function of temperature, as follows:

$$E_p(T) = E_o e^{\left(-\frac{\Delta E}{\kappa_B T}\right)}$$

We utilized the phonon energies obtained at both room temperature (RT) and liquid nitrogen (LN) temperature to determine the values E_o and ΔE.

The number of phonons (N_P) as a function of temperature follows the Boltzmann distribution:

$$N_p(T) = N_o e^{\left(-\frac{E_p(T)}{\kappa_B T}\right)}$$

So,

$$\frac{N_P(RT)}{N_p(LN)} \propto \frac{e^{-\left(\frac{E_p(RT)}{\kappa_B T(RT)}\right)}}{e^{-\left(\frac{E_p(LN)}{\kappa_B T(LN)}\right)}}$$

And we know that

$$\frac{\eta(RT)}{\eta(LN)} \approx \frac{N_P(RT)}{N_p(LN)}$$

Thus,

$$\eta(T) \approx \frac{\eta(RT)}{\frac{N_P(RT)}{N_p(T)}}$$

where $N_P(RT)$ is computed directly while $\eta(RT)$ is extracted from the data in Figure 2.2d across various detuning energies residing below the band gap.

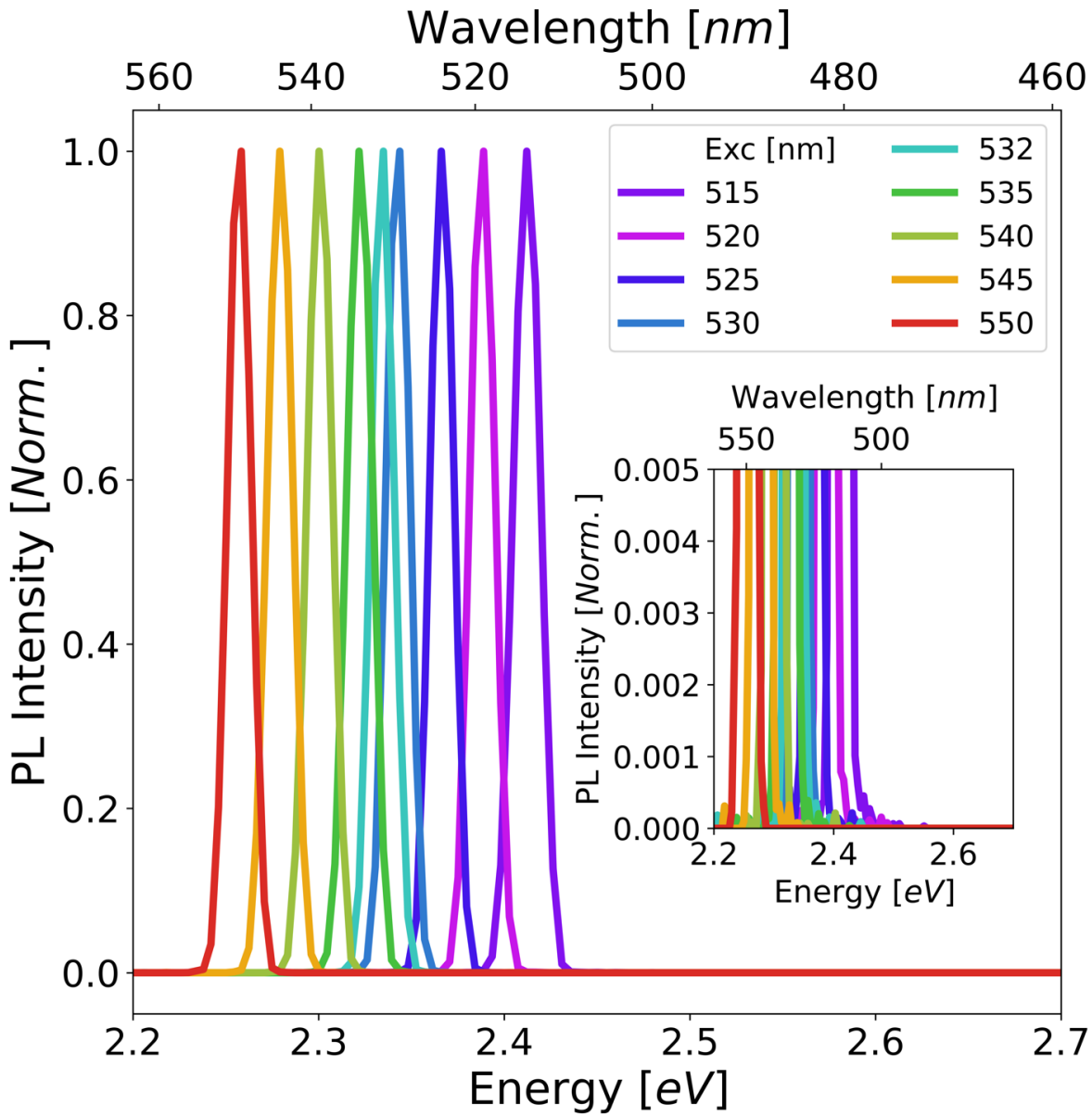


Figure A1: Anti-Stokes laser excitations with a 515 nm long pass filter.

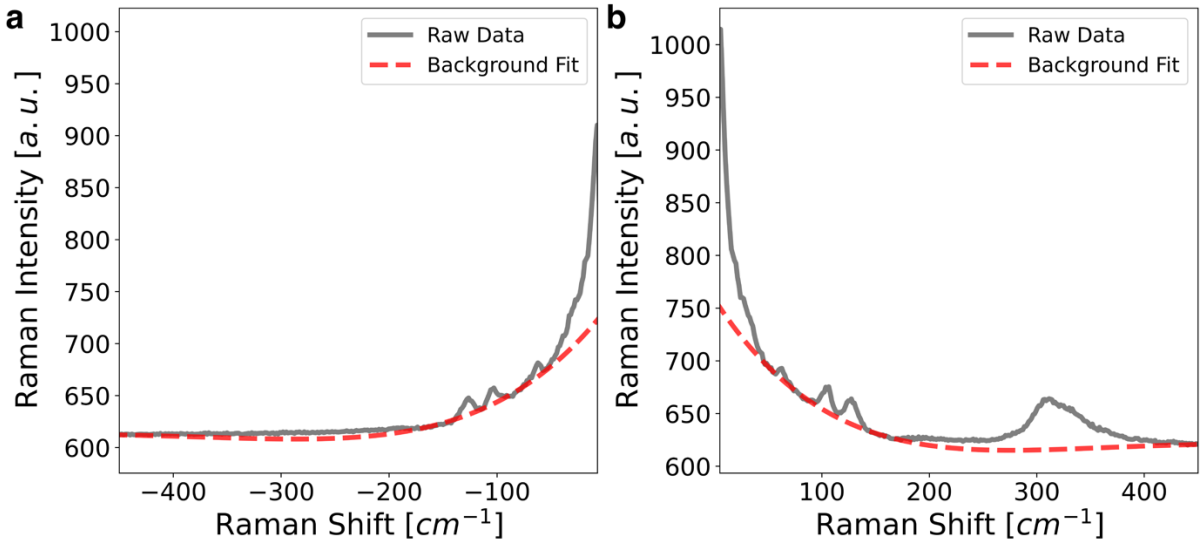


Figure A2: Raman spectroscopy. a, Anti-Stokes and **b**, Stokes Raman raw data with the background fit correction using the 5th order asymmetric truncated quadratic function.

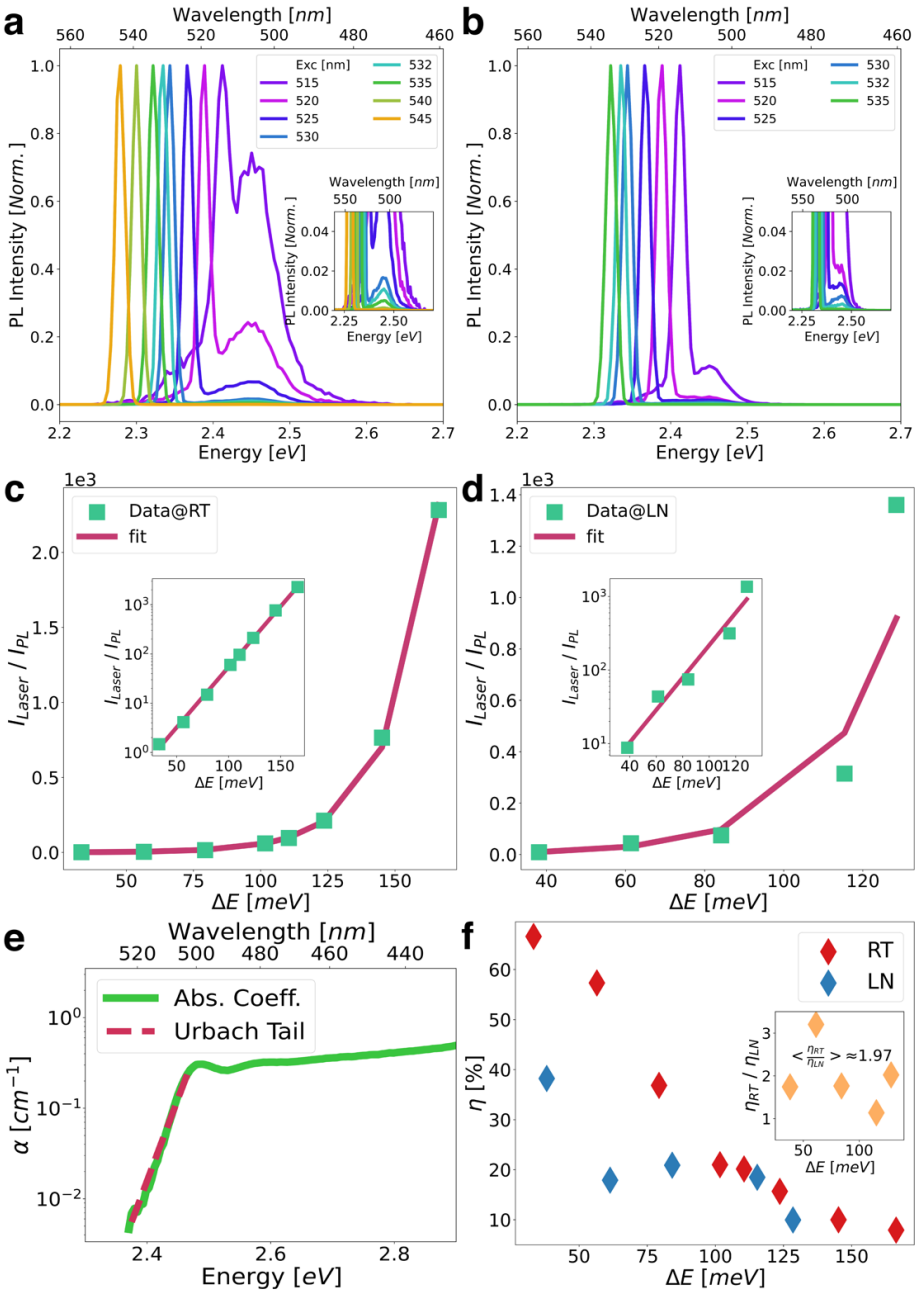


Figure A3: Comparative Analysis of Up-Conversion Efficiency at Room Temperature (RT) and Liquid Nitrogen (LN) Temperature. a, **b**, Below-gap excitation is illustrated for both (**a**) RT and (**b**) LN temperatures. **c**, **d**, Phonon energies of approximately 8 meV (64.712 cm^{-1}) and 6 meV (48.17 cm^{-1}) were determined by fitting the ratio of the laser intensity to the anti-Stokes photoluminescence (ASPL) intensity curve for (**c**) RT and (**d**) LN temperatures, respectively, and fall within the Pb-Br-Pb bending mode range[27,34,35,39]. **e**, The Urbach energy of 24.655 meV was obtained by fitting the tail of the absorption coefficient. **f**, Notably, the up-conversion efficiency exhibited a drastic decrease upon cooling to cryogenic LN temperatures, with a phonon population ratio closely matching the efficiency ratio.

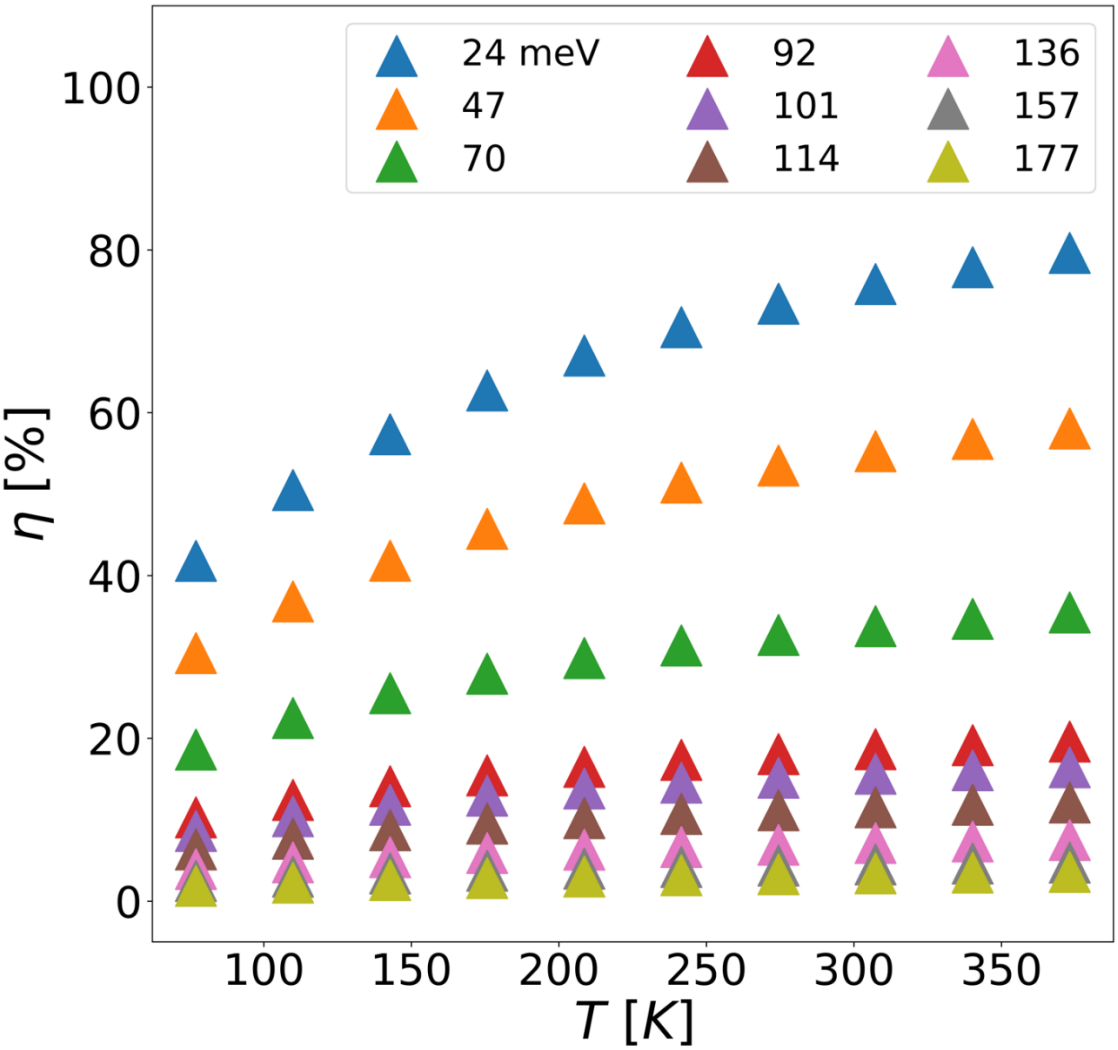


Figure A4: The up-conversion efficiency, as determined through the methodology described above, at various temperature conditions for different detuning energies below the band gap.

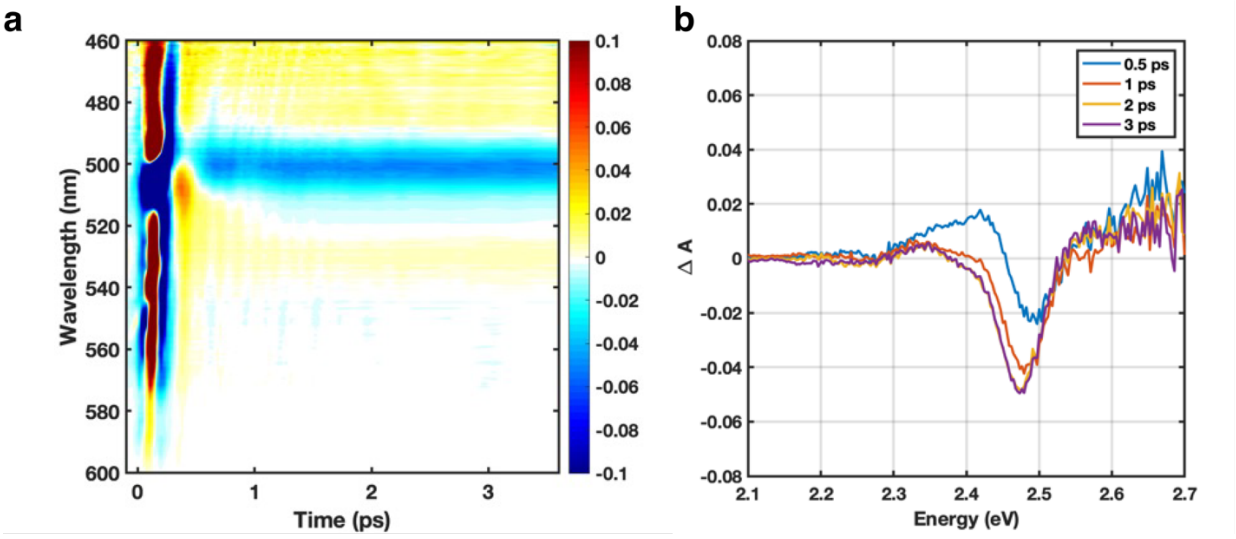


Figure A5: Low power below gap transient absorption. a, Time-resolved transient absorption map along with **b**, selected time traces at a low power of 163 $\frac{\mu J}{cm^2}$, demonstrating the persistent occurrence of coherent phonons.

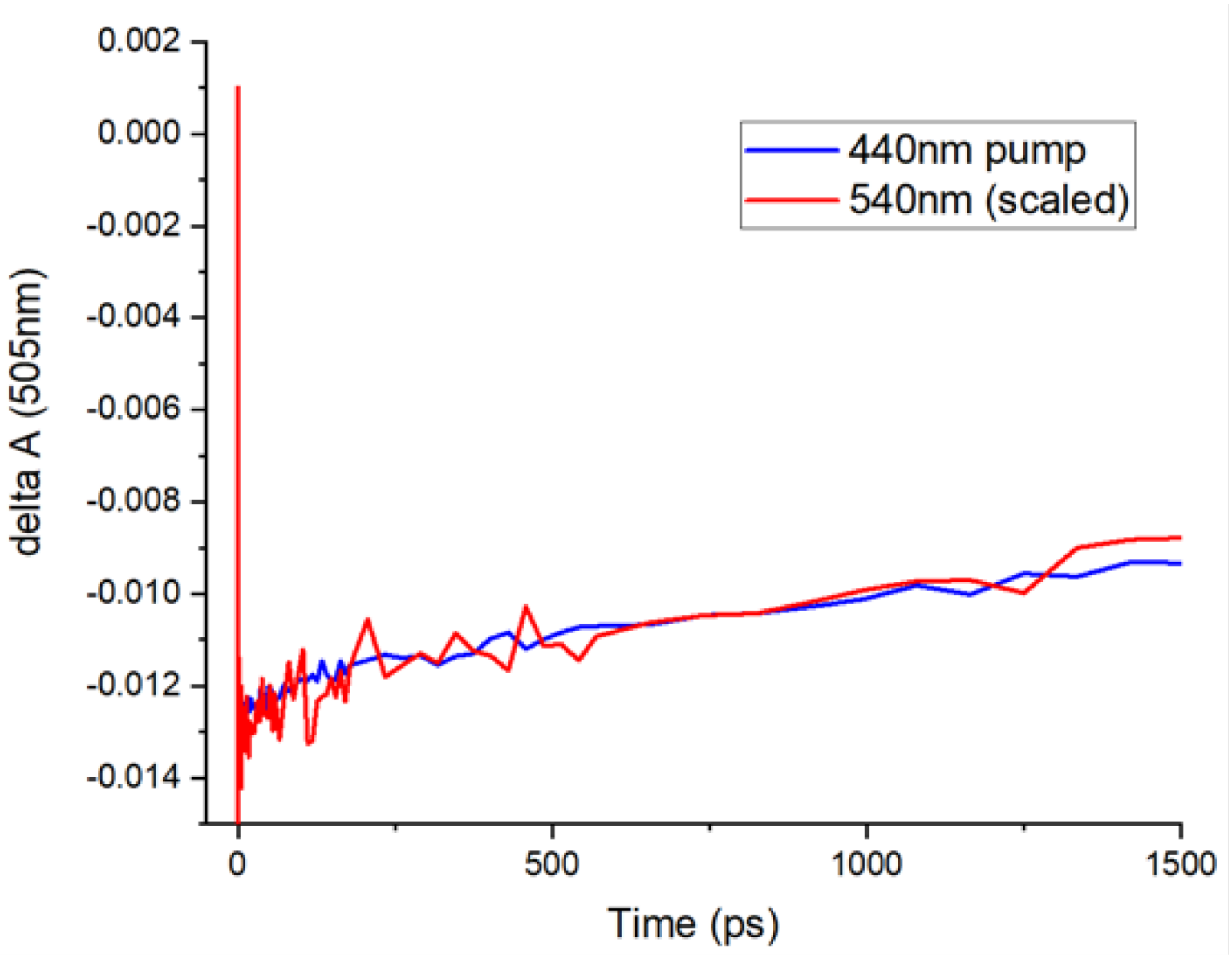


Figure A6: Illustration of decay traces that exhibit overlapping behavior in the long-time limit, both for resonant and non-resonant excitations.

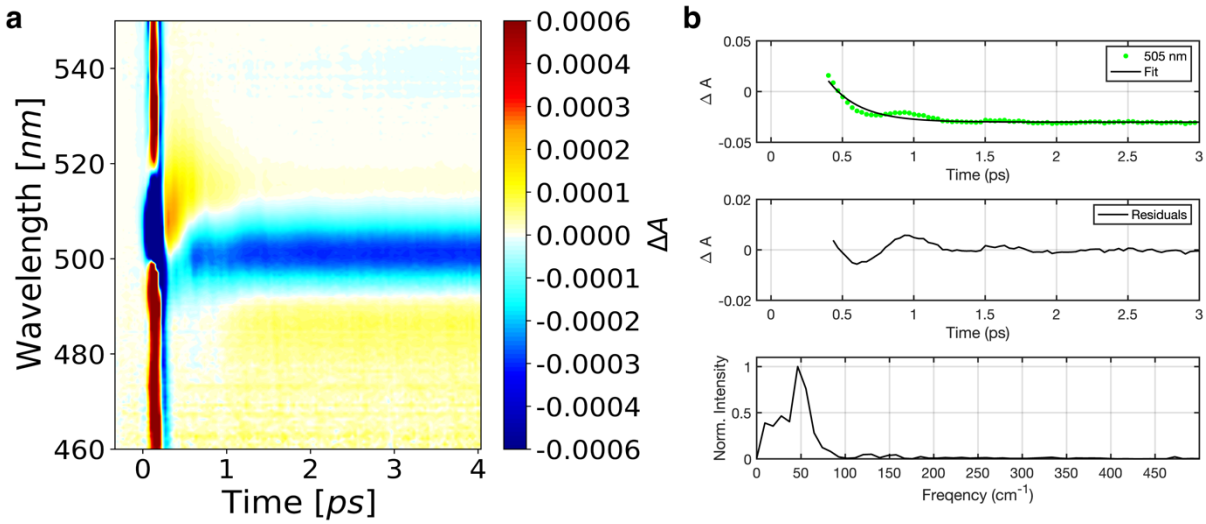


Figure A7: Time traces taken from a, time-resolved transient absorption and **b**, fitted to an exponential decay (top panel). The fit is subtracted to get the residual **(**b-middle panel) which is then Fourier transformed to get a beating frequency **(**bottom panel) that is attributed to a vibrational mode. This vibrational mode of ~50 cm^{-1} corresponds to the Pb-Br-Pb bending mode[27,34,35,39].

Appendix B

B.1 Up-Conversion Efficiency Analysis

The relation between up-conversion efficiency (η), Stokes photoluminescence (PL), and anti-Stokes photoluminescence (ASPL) is formulated[5] as follows:

$$I_{spl} = I_s\, A_s\, PLQY \tag{1}$$

$$I_{aspl} = I_{as}\, A_{as}\, \eta\, PLQY \tag{2}$$

where I_{spl} and I_{aspl} are the Stokes PL and ASPL intensities, $I_s$and I_{as} are the Stokes and anti-Stokes excitation intensities, A_s and A_{as} are the Stokes and anti-Stokes absorption, and η is the up-conversion efficiency. Measurement of the up-conversion efficiency (Figure B4-6) is performed such that I_{spl} and I_{aspl} are similar in value. This allows us to re-arrange equation (1) and (2) to solve for η as follows:

$$\eta \approx \frac{I_s\, A_s}{I_{as}\, A_{as}} \tag{3}$$

This requires knowing the absorption at the band tail (A_{as}) as a function of detuned energy within the bandgap. Due to the limitations of standard spectrophotometers in detecting absorption transition at the band tail, we resort to computing absorption using the correlation between the absorption coefficient and Urbach energy, as discussed below.

B.2 Urbach Energy

One method for quantifying absorption at the band tail (referred to as anti-Stokes absorption) involves determining the Urbach energy using the absorption coefficient relations:

$$\alpha(hv) = \alpha_o\, e^{\left(\frac{hv - E_{pl}}{E_u}\right)} \tag{4}$$

where α is the absorption coefficient, hv is the excitation energy, E_{pl} is the band edge energy, and E_u is the Urbach energy.

Solving for $\alpha_o$at the band edge is as follows:

$$I = I_o e^{-\alpha L} \tag{5}$$

$$log_{10}\left(\frac{I_o}{I}\right) = A = \alpha\, L\, log_{10}(e) \tag{6}$$

rearranging equation (6),

$$\alpha_o = \frac{A}{L\, log_{10}(e)} \tag{7}$$

where A is the absorption and L is cuvette path length (standard 1 cm). We solve for α_o at the band edge. Then rearranging equation (4):

$$\ln(\alpha(hv)) \propto \frac{1}{E_u} hv \tag{8}$$

We see that the Urbach energy can be extracted from the slope of the absorption coefficient as a function of excitation energy at the band tail, as shown in Figure B4-6.

By utilizing the Urbach energy in conjunction with the absorption coefficient at the band edge, the anti-Stokes absorption can be derived from equation (3). Subsequently, this enables determination of the up-conversion efficiency.

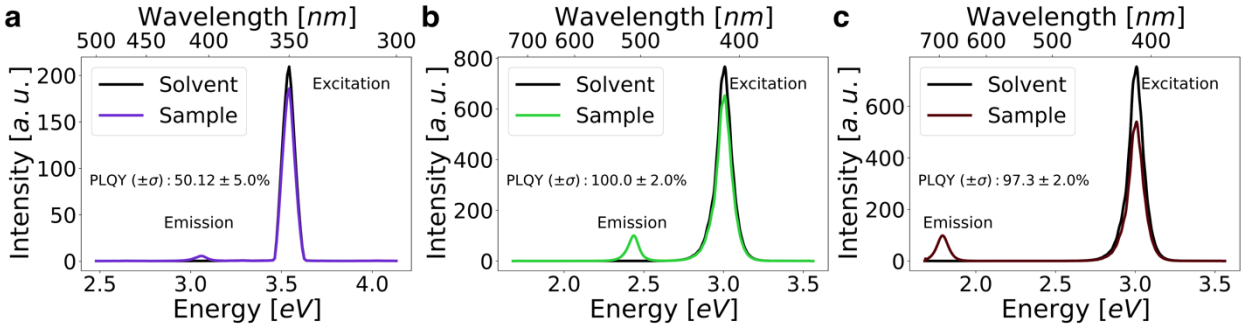


Figure B1: Absolute Photoluminescence Quantum Yield (PLQY). PLQY measured using integrating sphere for (a) $CsPbCl_3$ ($50.12\% \pm 5\%$), (b) $CsPbBr_3$ ($100\% \pm 2\%$), and (c) $CsPbI_3$ ($97.3\% \pm 2\%$).

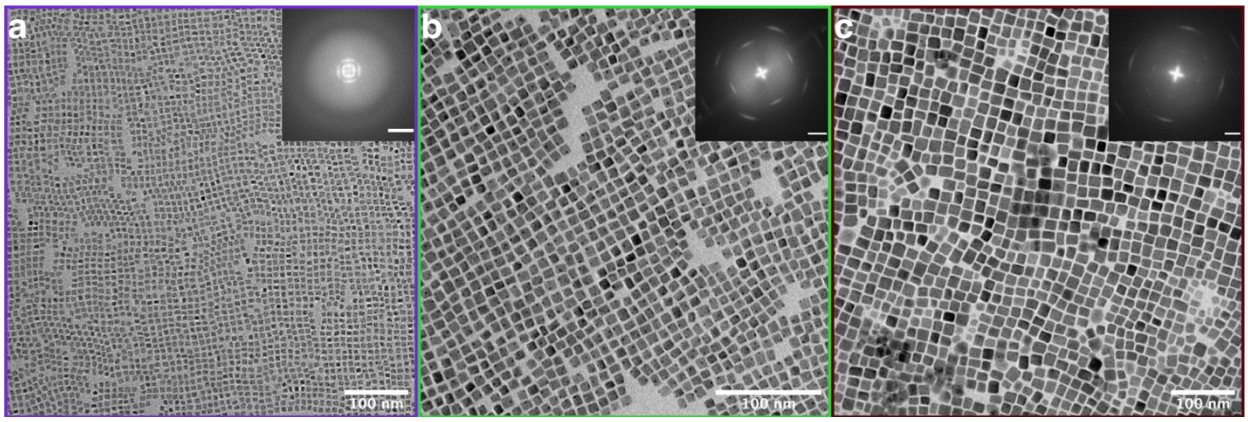


Figure B2: Transmission Electron Microscopy (TEM) images. Large area TEM images along with their respective Fast Fourier Transform (FFT) for (a) $CsPbCl_3$ (FFT scale bar $= 0.5\ nm^{-1}$), (b) $CsPbBr_3$ (FFT scale bar $= 1\ nm^{-1}$), and (c) $CsPbI_3$ (FFT scale bar $= 0.5\ nm^{-1}$).

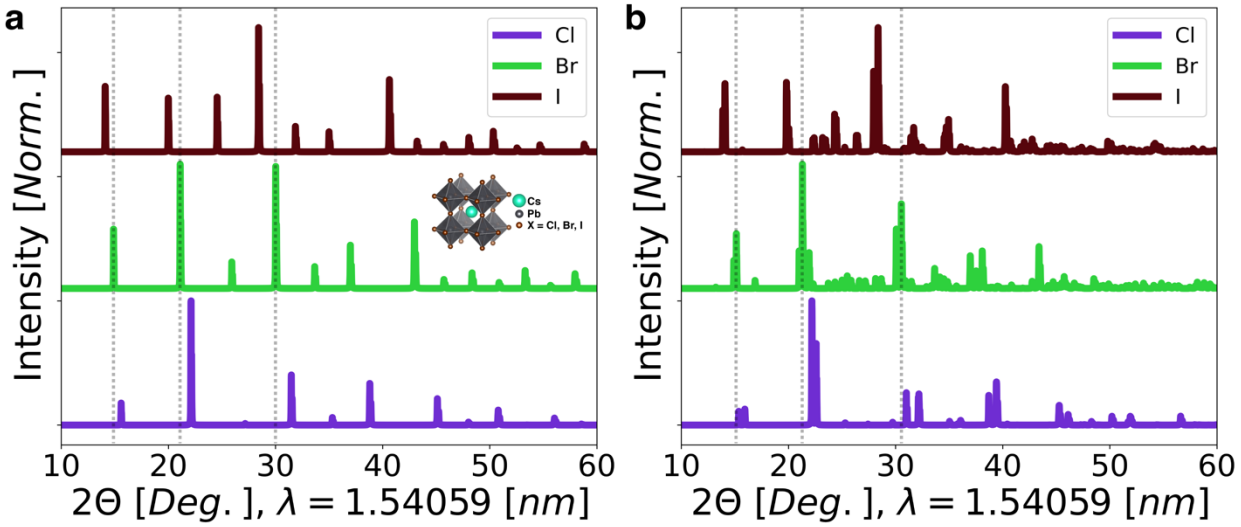


Figure B3: X-Ray Diffraction (XRD) Patterns. Reference XRD Patterns of pure halide perovskites in (a) cubic and (b) orthorhombic symmetry. Crystal structure (CIF files) was obtained from Materials Project[92] while the XRD patterns was computed using Vesta[38].

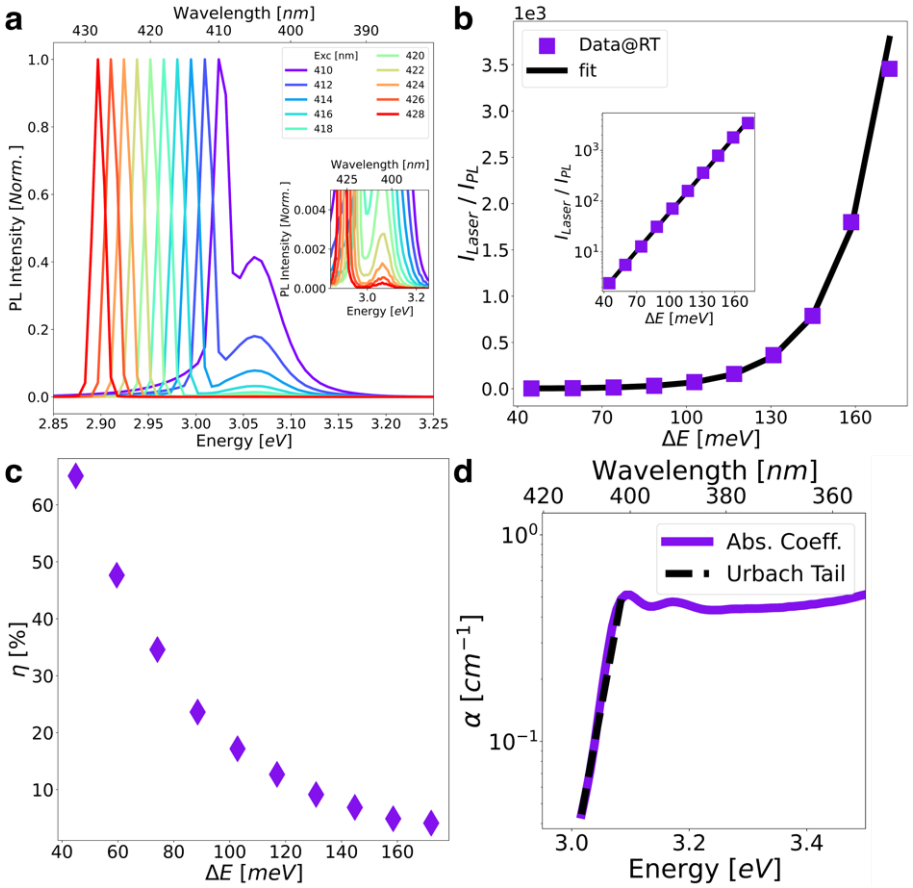


Figure B4: Below gap photoexcitation of $CsPbCl_3$ nanocrystals. (a) Photoexcitations with energies detuned within the band gap exhibit a distinct band edge emission. (b) The plot of laser intensity to band edge emission ratio reveals an exponential trend that is modeled with Arrhenius equation. Inset, shown on a logarithmic scale, confirm the exponential trend. The goodness of fit is $R^2 = 0.9903$. (c) The calculated up-conversion efficiency as a function of detuned energies within the bandgap. (d) Absorption coefficient is plotted, and the band tail is fitted to extract the Urbach energy required for calculating the up-conversion efficiency.

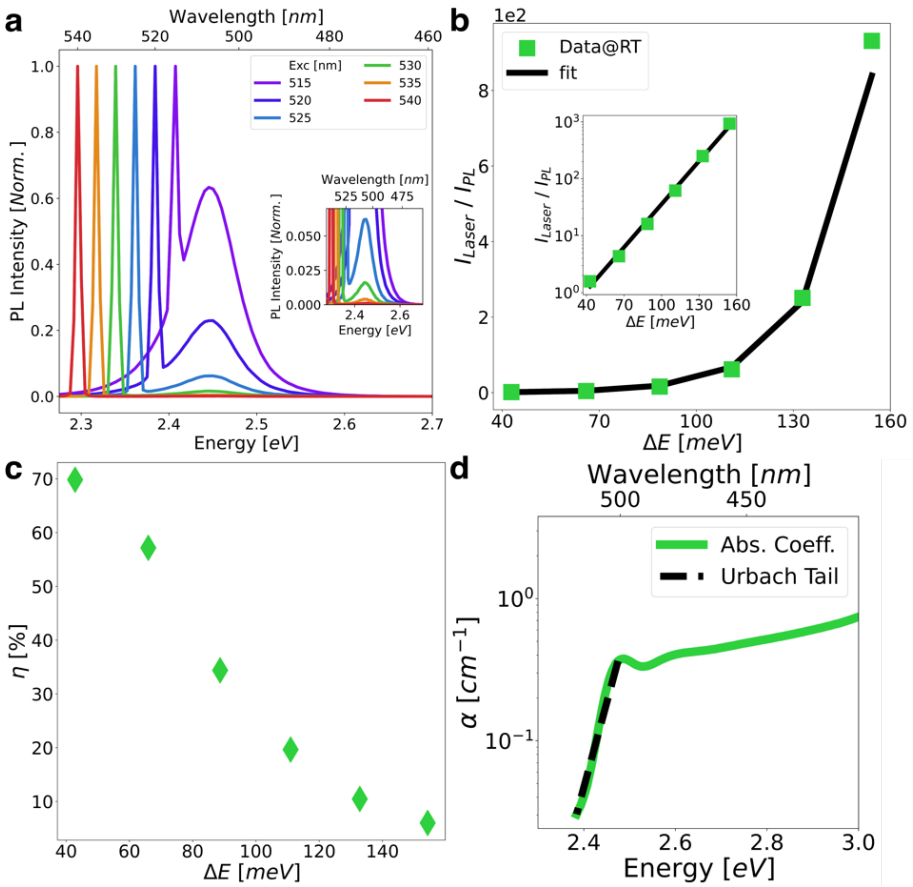


Figure B5: Below gap photoexcitation of $CsPbBr_3$ nanocrystals. (a) Photoexcitations with energies detuned within the band gap exhibit a distinct band edge emission. (b) The plot of laser intensity to band edge emission ratio reveals an exponential trend that is modeled with Arrhenius equation. Inset, shown on a logarithmic scale, confirm the exponential trend. The goodness of fit is $R^2 = 0.9988$. (c) The calculated up-conversion efficiency as a function of detuned energies within the bandgap. (d) Absorption coefficient is plotted, and the band tail is fitted to extract the Urbach energy required for calculating the up-conversion efficiency.

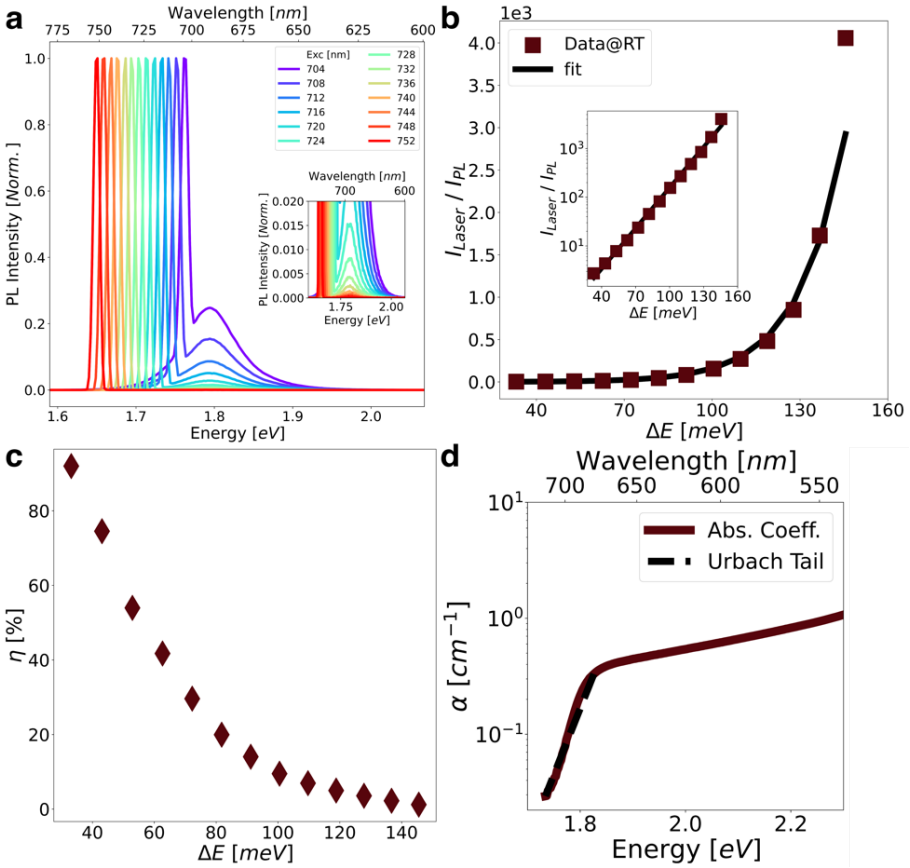


Figure B6: Below gap photoexcitation of $CsPbI_3$ nanocrystals. (a) Photoexcitations with energies detuned within the band gap exhibit a distinct band edge emission. (b) The plot of laser intensity to band edge emission ratio reveals an exponential trend that is modeled with Arrhenius equation. Inset, shown on a logarithmic scale, confirm the exponential trend. The goodness of fit is $R^2 = 0.9186$. (c) The calculated up-conversion efficiency as a function of detuned energies within the bandgap. (d) Absorption coefficient is plotted, and the band tail is fitted to extract the Urbach energy required for calculating the up-conversion efficiency.

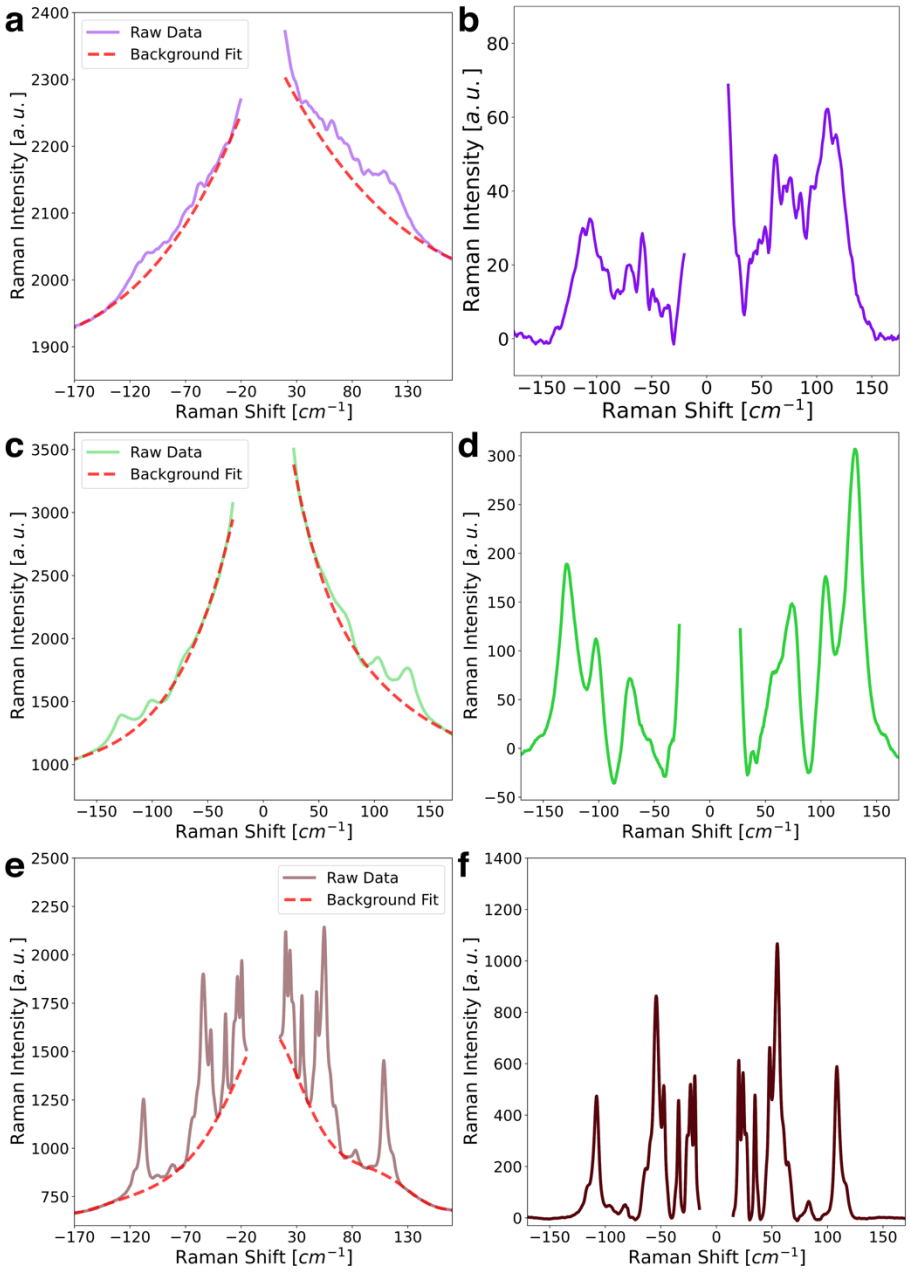


Figure B7: Raman spectroscopy. Raw data along with the background fit correction using the 5th order asymmetric truncated quadratic function and the data after background subtraction for (a and b) $CsPbCl_3$, (c and d) $CsPbBr_3$, and (e and f) $CsPbI_3$.

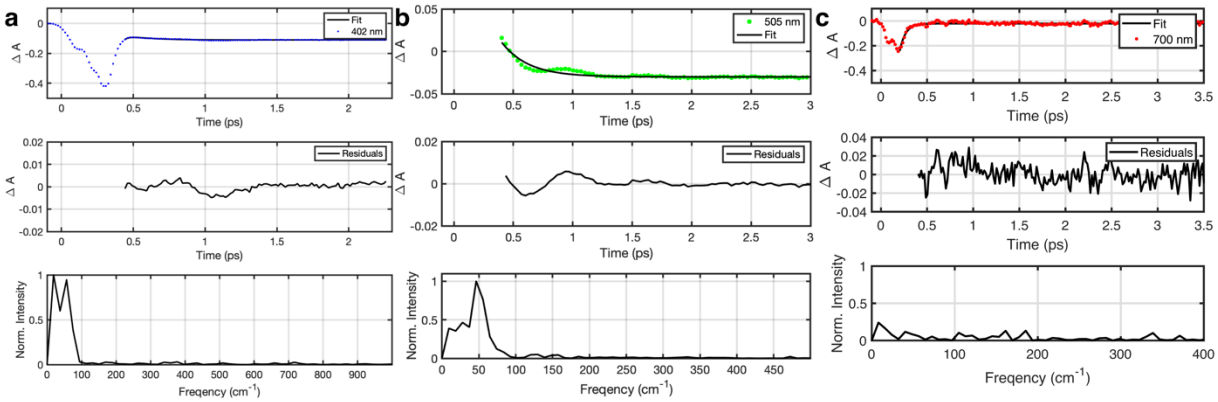


Figure B8: Beating frequency. Analysis of the beating frequency conducted for (a) $CsPbCl_3$, (a) $CsPbBr_3$, and (a) $CsPbI_3$ perovskite nanocrystals. (top panel) Time traces acquired from time-resolved transient absorption are fitted to an exponential decay. (middle panel) The fit is then subtracted to get the residual signal, which is then (bottom panel) Fourier transformed to get a beating frequency that is attributed to a vibrational mode. Specifically, in $CsPbCl_3$, we identify a vibration mode at approximately 57 cm^{-1}, attributed to the transverse optical (TO) mode involving the stretching of Cl atoms in the $[PbCl_3]^-$ octahedral cage[55,56]. We also observe an oscillation with a frequency of around 50 cm^{-1} corresponding to the Pb-Br-Pb bending mode in $CsPbBr_3$[27,34,35,39]. However, in $CsPbI_3$, no distinct oscillation is observed.

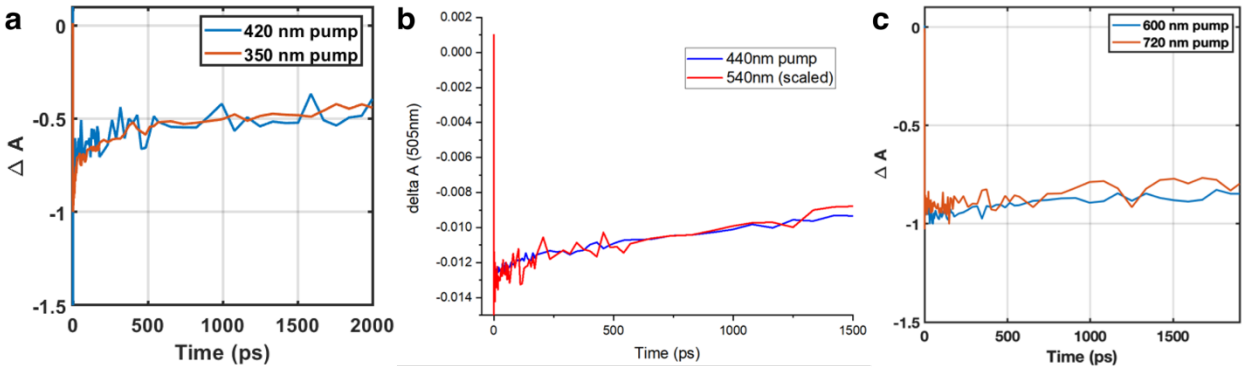


Figure B9: Long-time limit transient absorption (TA) bleach decays under above and below gap excitation. The decay traces exhibit overlapping behavior in the long-time limit for (a) $CsPbCl_3$, (b) $CsPbBr_3$, and (c) $CsPbI_3$.

Appendix C

C.1 Up-Conversion Efficiency Analysis

The relation between up-conversion efficiency (η), Stokes photoluminescence (PL), and anti-Stokes photoluminescence (ASPL) is formulated[5] as follows:

$$I_{spl} = I_s\, A_s\, PLQY \tag{1}$$

$$I_{aspl} = I_{as}\, A_{as}\, \eta\, PLQY \tag{2}$$

where I_{spl} and I_{aspl} are the Stokes PL and ASPL intensities, $I_s$and I_{as} are the Stokes and anti-Stokes excitation intensities, A_s and A_{as} are the Stokes and anti-Stokes absorption, and η is the up-conversion efficiency. Measurement of the up-conversion efficiency (Figure C4-6) is performed such that I_{spl} and I_{aspl} are similar in value. This allows us to re-arrange equation (1) and (2) to solve for η as follows:

$$\eta \approx \frac{I_s\, A_s}{I_{as}\, A_{as}} \tag{3}$$

This requires knowing the absorption at the band tail (A_{as}) as a function of detuned energy within the bandgap. Due to the limitations of standard spectrophotometers in detecting absorption transition at the band tail, we resort to computing absorption using the correlation between the absorption coefficient and Urbach energy, as discussed below.

C.2 Urbach Energy

One method for quantifying absorption at the band tail (referred to as anti-Stokes absorption) involves determining the Urbach energy using the absorption coefficient relations:

$$\alpha(hv) = \alpha_o\, e^{\left(\frac{hv - E_{pl}}{E_u}\right)} \tag{4}$$

where α is the absorption coefficient, hv is the excitation energy, E_{pl} is the band edge energy, and E_u is the Urbach energy.

Solving for $\alpha_o$at the band edge is as follows:

$$I = I_o e^{-\alpha L} \tag{5}$$

$$log_{10}\left(\frac{I_o}{I}\right) = A = \alpha\, L\, log_{10}(e) \tag{6}$$

rearranging equation (6),

$$\alpha_o = \frac{A}{L\, log_{10}(e)} \tag{7}$$

where A is the absorption and L is cuvette path length (standard 1 cm). We solve for α_o at the band edge. Then rearranging equation (4):

$$\ln(\alpha(hv)) \propto \frac{1}{E_u} hv \tag{8}$$

We see that the Urbach energy can be extracted from the slope of the absorption coefficient as a function of excitation energy at the band tail, as shown in Figure C4-6.

By utilizing the Urbach energy in conjunction with the absorption coefficient at the band edge, the anti-Stokes absorption can be derived from equation (3). Subsequently, this enables determination of the up-conversion efficiency.

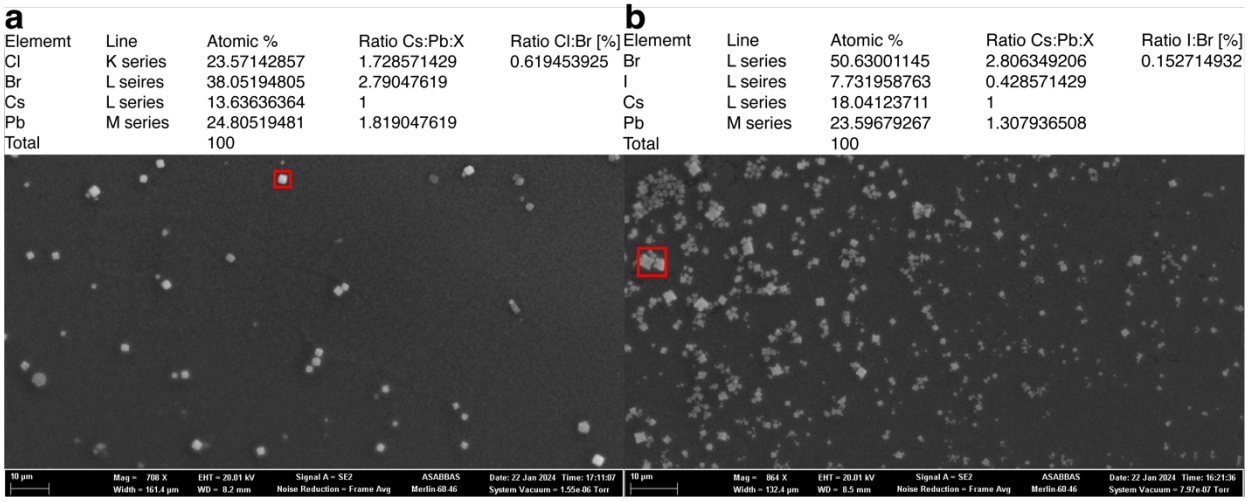


Figure C1: Elemental analysis. Scanning electron microscopy images with energy-dispersive spectroscopy (EDS) quantifying the composition of (a) $CsPbCl_{0.75}Br_{2.25}$ and (b) $CsPbI_{0.75}Br_{2.25}$ perovskite nanocrystal.

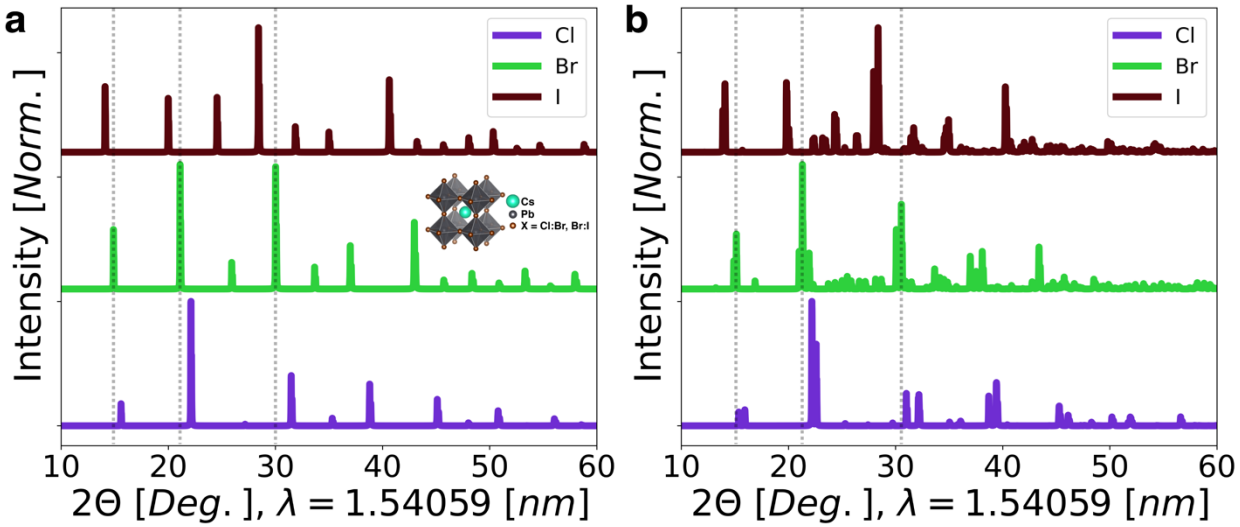


Figure C2: X-Ray Diffraction (XRD) Patterns. Reference XRD Patterns of pure halide perovskites in (a) cubic and (b) orthorhombic symmetry. Crystal structure (CIF files) was obtained from Materials Project[92] while the XRD patterns was computed using Vesta[38].

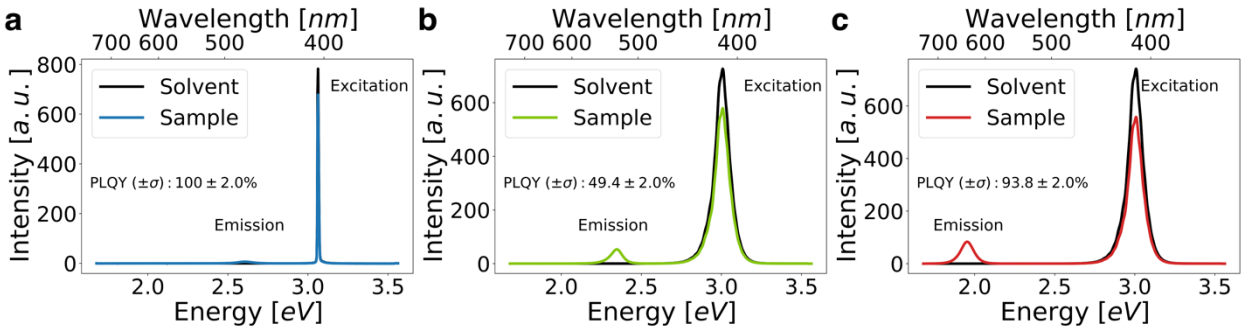


Figure C3: Absolute Photoluminescence Quantum Yield (PLQY). PLQY measured using integrating sphere for (a) $CsPbCl_{0.75}Br_{2.25}$ (100% ± 5%), (b) $CsPbI_{0.75}Br_{2.25}$ (49.4% ± 2%), and (c) $CsPbCl_{0.75}Br_{2.25}$ (93.8% ± 2%).

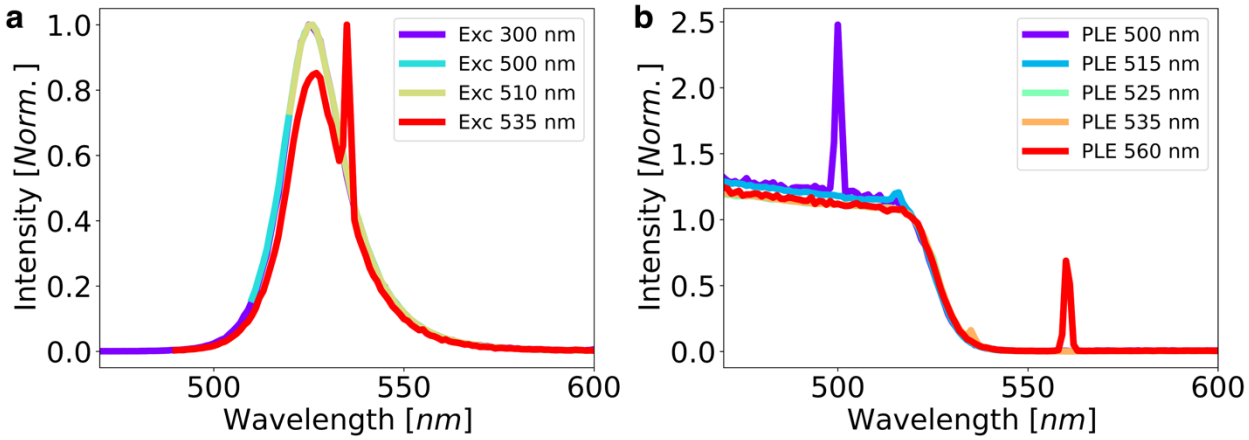


Figure C4: Above and below gap photoluminescence emission and excitation scans. To ensure homogenous mixing of iodide and bromide in $CsPbI_{0.75}Br_{2.25}$ nanocrystals, (a) photoluminescence emission scanned with excitation above and below gap reveal band edge emission, further confirming the homogenous mixing of the halides. (b) Photoluminescence excitation scan while detecting at wavelength above and below gap also results in identical spectra, ensuring homogeneity in the mixed halide perovskites.

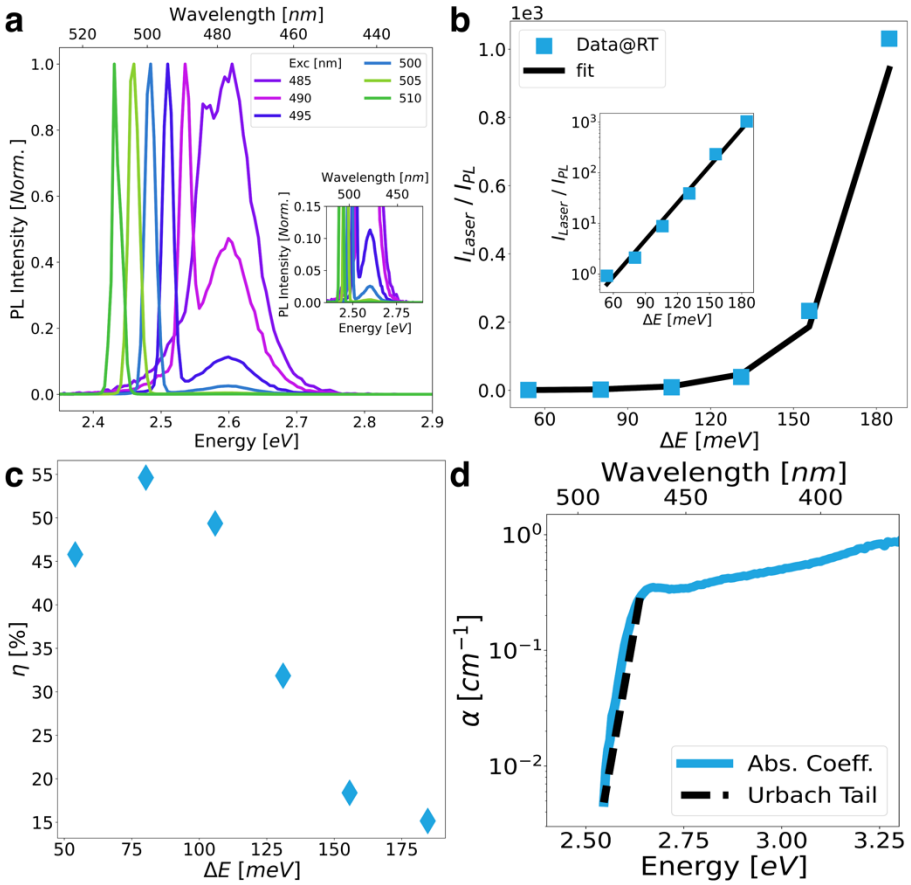


Figure C5: Below gap photoexcitation of $CsPbCl_{0.75}Br_{2.25}$ nanocrystals. (a) Photoexcitations with energies detuned within the band gap exhibit a distinct band edge emission. (b) The plot of laser intensity to band edge emission ratio reveals an exponential trend that is modeled with Arrhenius equation. Inset, shown on a logarithmic scale, confirm the exponential trend. The goodness of fit is R^2 = 0.98784. (c) The calculated up-conversion efficiency as a function of detuned energies within the bandgap. (d) Absorption coefficient is plotted, and the band tail is fitted to extract the Urbach energy required for calculating the up-conversion efficiency.

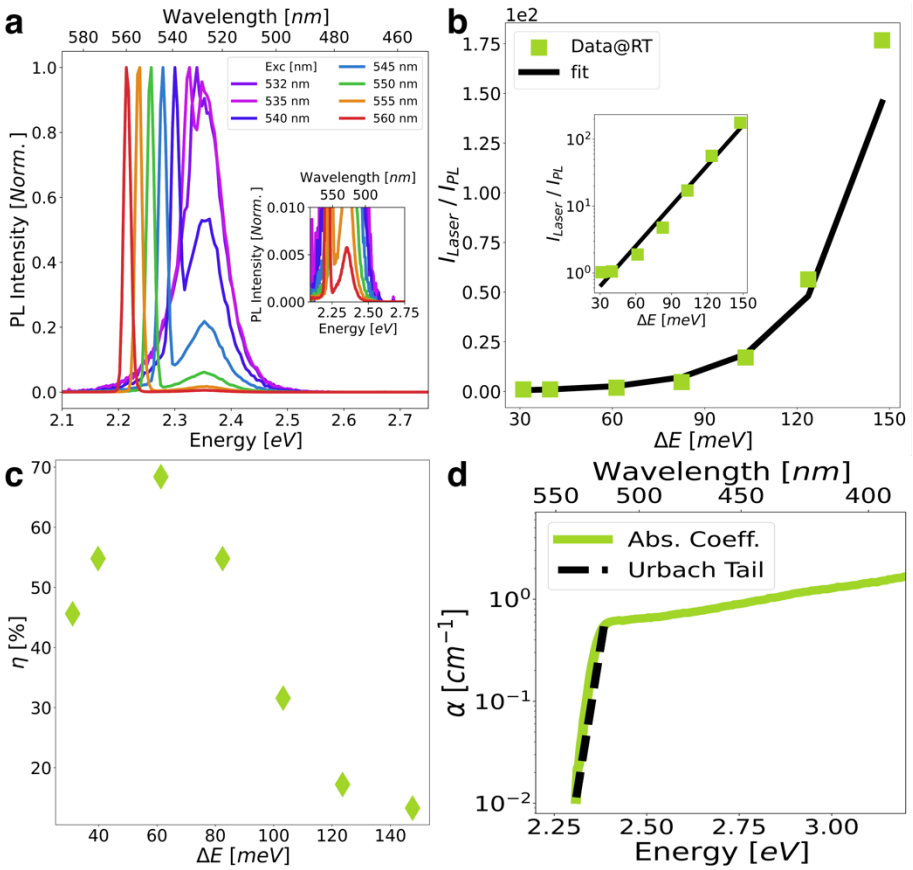


Figure C6: Below gap photoexcitation of $CsPbI_{0.75}Br_{2.25}$ nanocrystals. (a) Photoexcitations with energies detuned within the band gap exhibit a distinct band edge emission. (b) The plot of laser intensity to band edge emission ratio reveals an exponential trend that is modeled with Arrhenius equation. Inset, shown on a logarithmic scale, confirm the exponential trend. The goodness of fit is $R^2 = 0.9581$. (c) The calculated up-conversion efficiency as a function of detuned energies within the bandgap. (d) Absorption coefficient is plotted, and the band tail is fitted to extract the Urbach energy required for calculating the up-conversion efficiency.

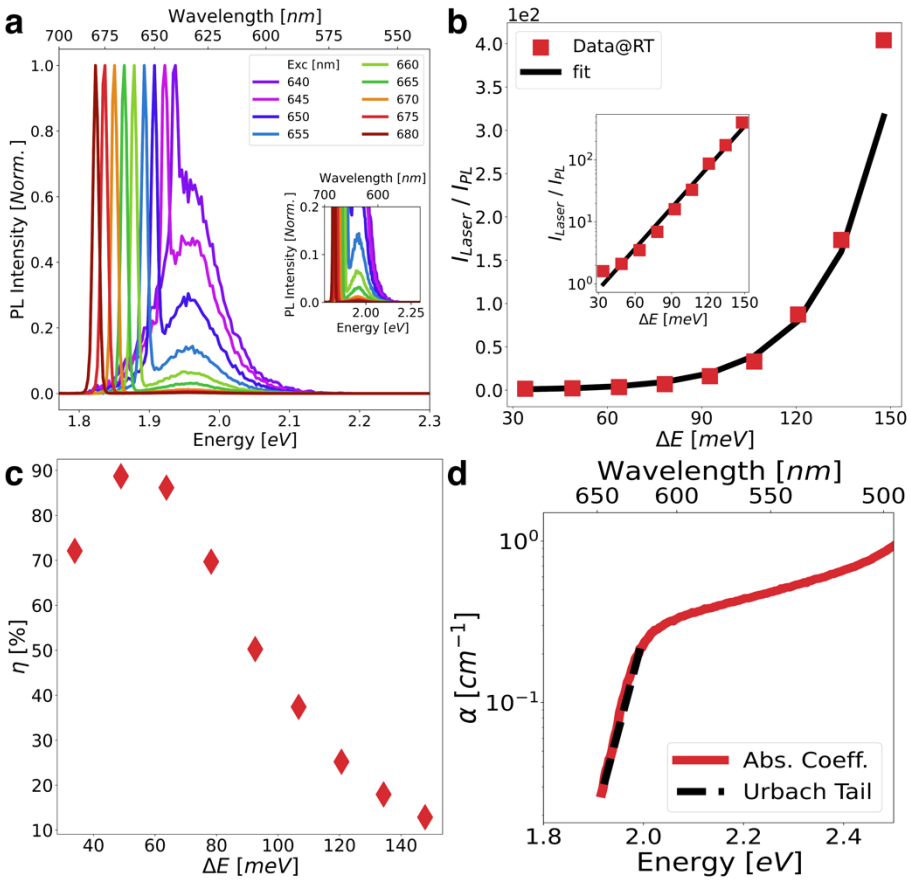


Figure C7: Below gap photoexcitation of $CsPbBr_{0.75}I_{2.25}$ nanocrystals. (a) Photoexcitations with energies detuned within the band gap exhibit a distinct band edge emission. (b) The plot of laser intensity to band edge emission ratio reveals an exponential trend that is modeled with Arrhenius equation. Inset, shown on a logarithmic scale, confirm the exponential trend. The goodness of fit is $R^2 = 0.9440$. (c) The calculated up-conversion efficiency as a function of detuned energies within the bandgap. (d) Absorption coefficient is plotted, and the band tail is fitted to extract the Urbach energy required for calculating the up-conversion efficiency.

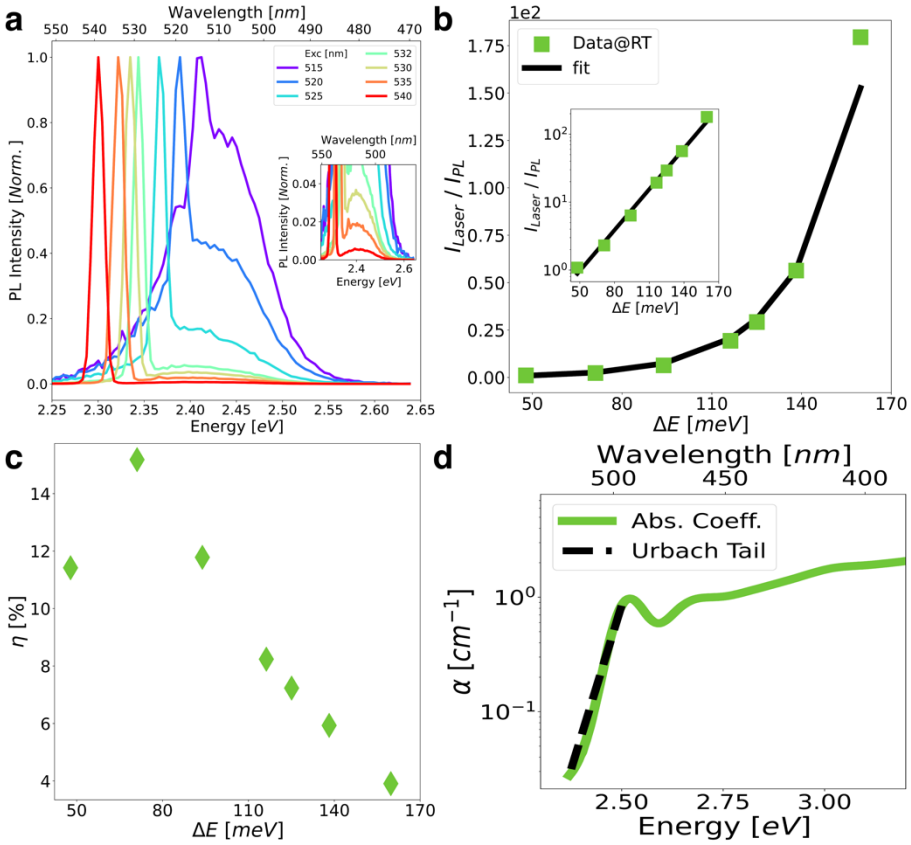


Figure C8: Below gap photoexcitation of strongly confined $CsPbI_{0.75}Br_{2.25}$ nanocrystals. (a) Photoexcitations with energies detuned within the band gap exhibit a distinct band edge emission. (b) The plot of laser intensity to band edge emission ratio reveals an exponential trend that is modeled with Arrhenius equation. Inset, shown on a logarithmic scale, confirm the exponential trend. The goodness of fit is $R^2 = 0.9703$. (c) The calculated up-conversion efficiency as a function of detuned energies within the bandgap. (d) Absorption coefficient is plotted, and the band tail is fitted to extract the Urbach energy required for calculating the up-conversion efficiency.

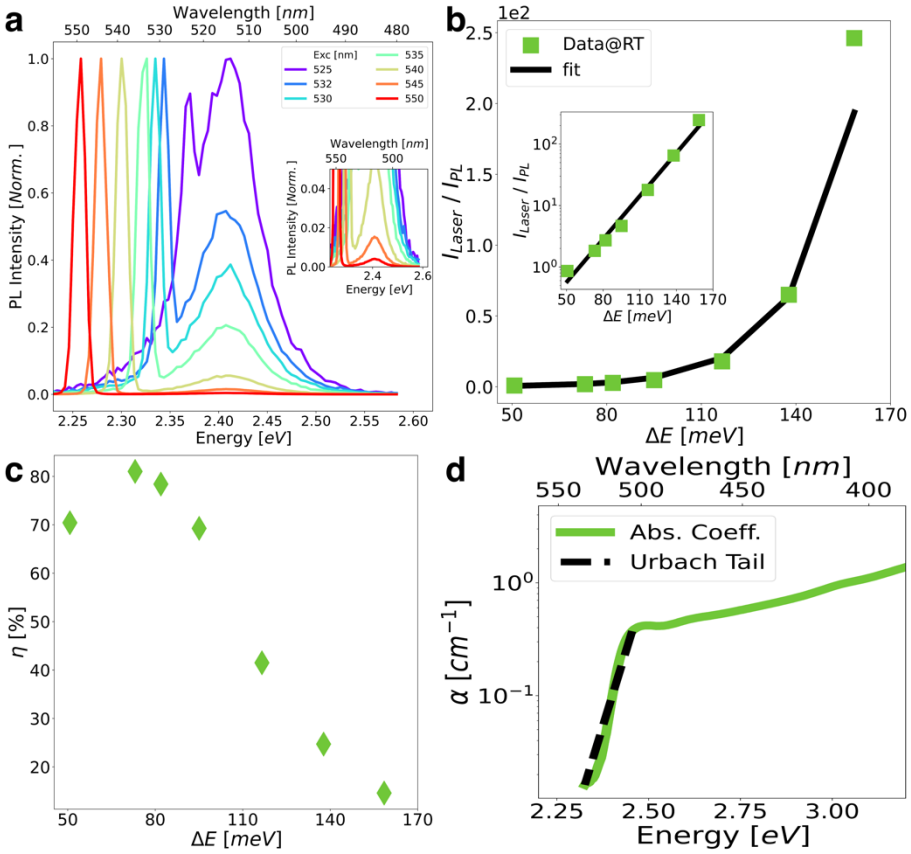


Figure C9: Below gap photoexcitation of intermediately confined $CsPbI_{0.75}Br_{2.25}$ nanocrystals. (a) Photoexcitations with energies detuned within the band gap exhibit a distinct band edge emission. (b) The plot of laser intensity to band edge emission ratio reveals an exponential trend that is modeled with Arrhenius equation. Inset, shown on a logarithmic scale, confirm the exponential trend. The goodness of fit is $R^2 = 0.9432$. (c) The calculated up-conversion efficiency as a function of detuned energies within the bandgap. (d) Absorption coefficient is plotted, and the band tail is fitted to extract the Urbach energy required for calculating the up-conversion efficiency.

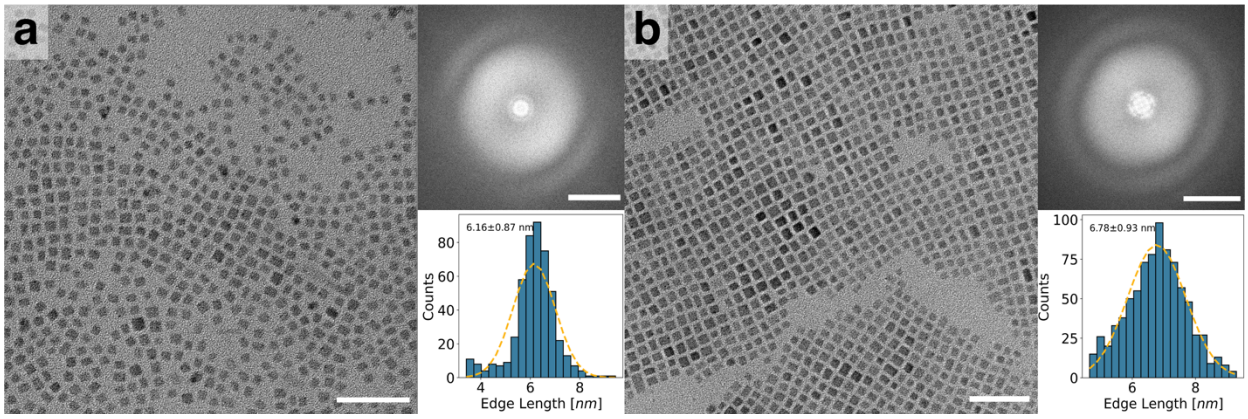


Figure C10: $CsPbI_{0.75}Br_{2.25}$ nanocrystals with varying sizes. Transmission electron microscopy (TEM) images and their corresponding Fast Fourier Transform (FFT) pattern, displaying monodispersed cubic nanocrystals of mixed $CsPbI_{0.75}Br_{2.25}$ perovskites with (a) strongly confined

sized at $6.16 \pm 0.87\ nm$ and (b) intermediately confined nanocrystals sized at $6.78 \pm 0.93\ nm$. Scale bars: main TEM – $50\ nm$, main FFT – $1\ nm^{-1}$.

Appendix D

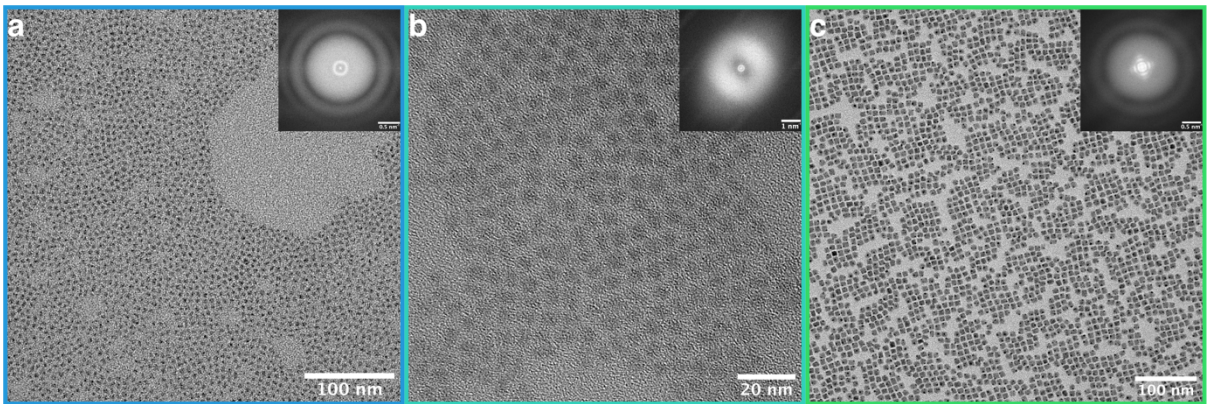


Figure D1: Transmission electron microscopy (TEM) characterization of $CsPbBr_3$ nanocrystals. a,**b**,**c**, TEM images of three selected nanocrystals sizes in (**a**) strong, (**b**) intermediate, and (**c**) weak quantum confinement regime with their corresponding Fast Fourier Transform (FFT).

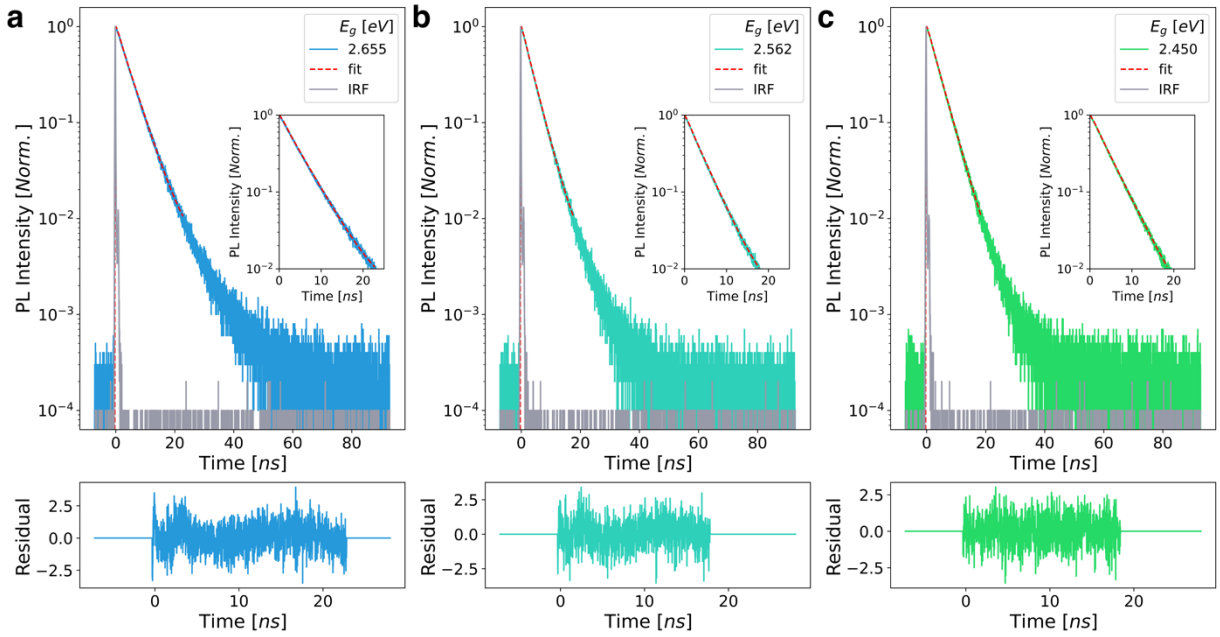


Figure D2: Time-resolved photoluminescence (TRPL) characterization. a,**b**,**c**, depict TRPL decays, deconvoluted with instrument response function (IRF), with the initial two decades fitted to a monoexponenital function for nanocrystal sizes within (**a**) strong, (**b**) intermediate, and (**c**) weak quantum confinement regime. Each plot includes the residuals showing the goodness of the fit.

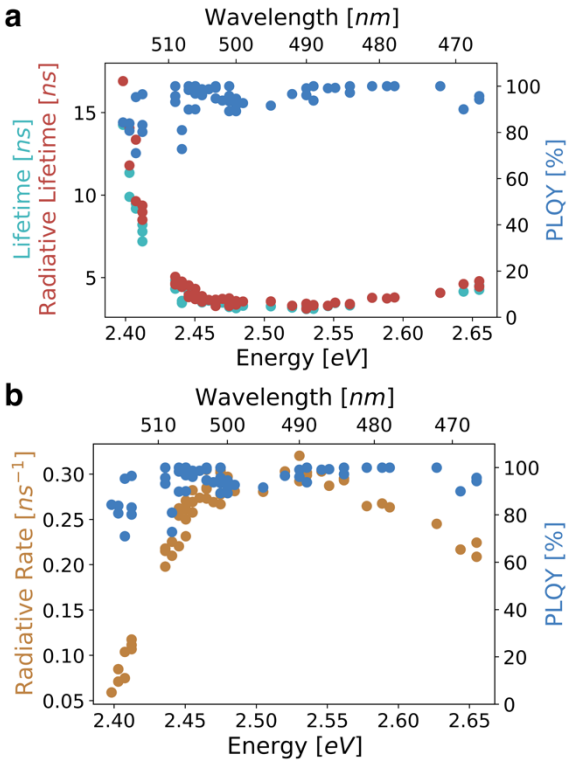


Figure D3: Size-dependent radiative lifetimes and rates of $CsPbBr_3$ nanocrystals. a,**b**, Varying nanocrystals spanning further in the weak confinement regime illustrating extended (**a**) radiative lifetimes and reduced (**b**) radiative rates.

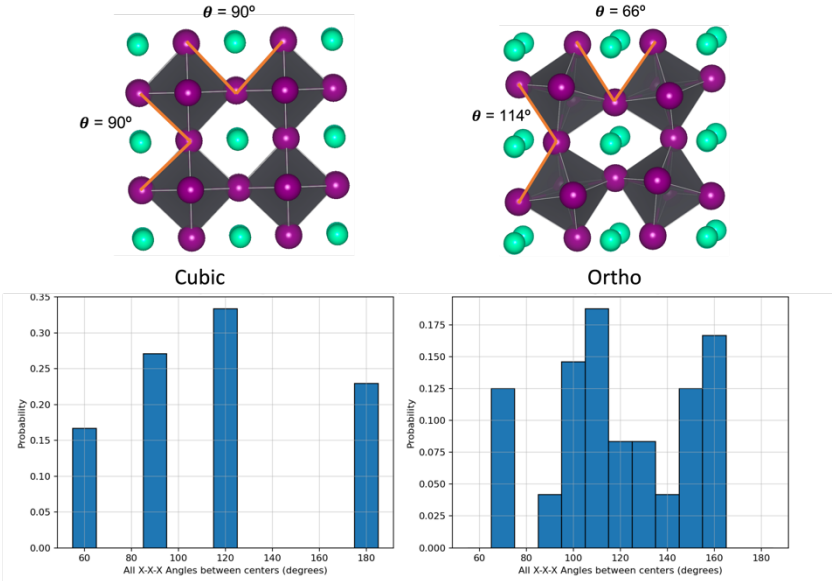


Figure D4: Cubic vs orthorhombic $CsPbBr_3$ structure. a,**b**, Probability distribution of X-X-X angles in ideal (**a**) cubic and (**b**) orthorhombic $CsPbBr_3$ structure. In the cubic symmetry, the 60º angle is distinctly prominent, while 160º angle occurs only in the orthorhombic symmetry.

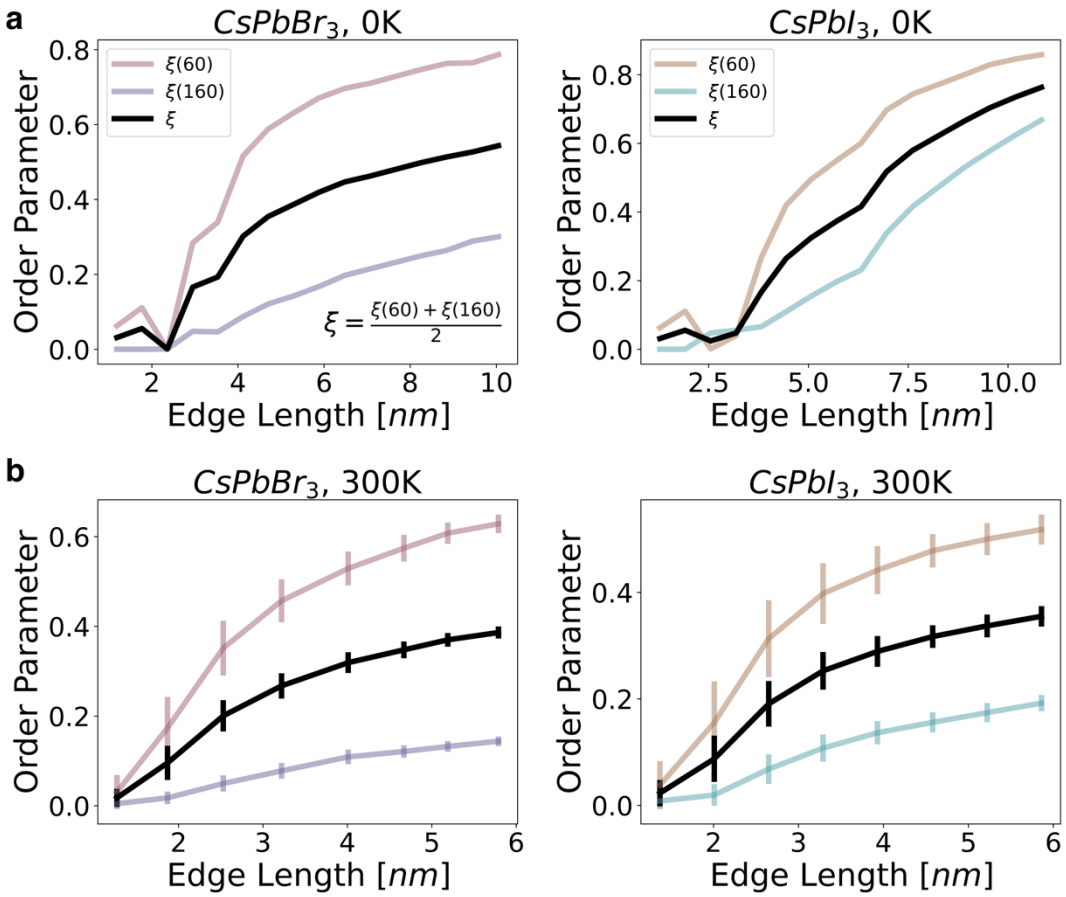


Figure D5: Order parameter. a,**b**, Comparison of order parameter for $CsPbBr_3$ and $CsPbI_3$ nanocrystals with varying sizes at (**a**) 0 K and (**b**) 300 K. Both perovskites initially exhibit cubic symmetry in smaller sizes, then transition into orthorhombic symmetry as the nanocrystal size increases.

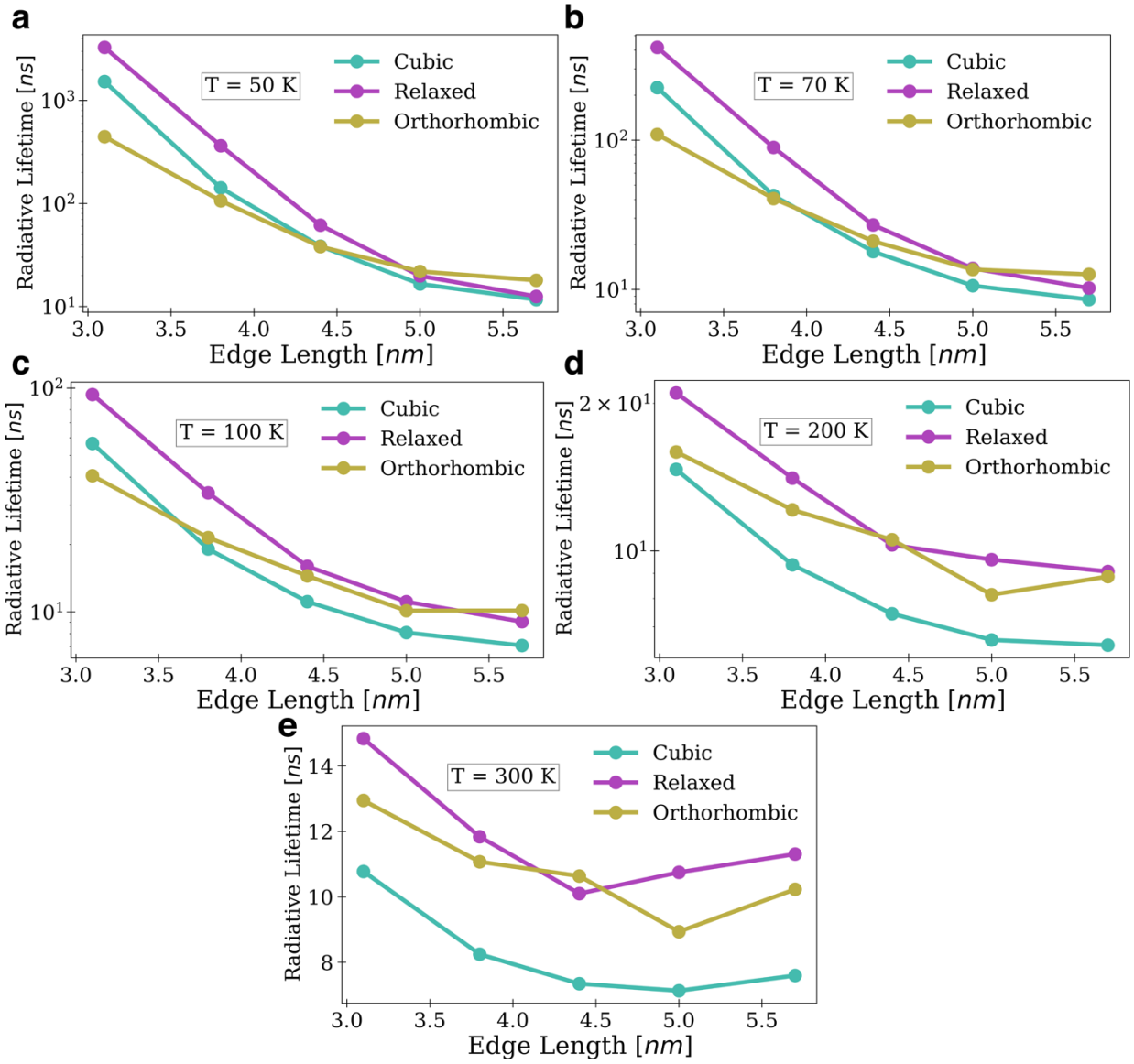


Figure D6: Size Dependent Radiative Lifetime Across Different Temperatures. a,**b**,**c**,**d**,**e**, Radiative lifetimes of halide perovskites as a function of temperature calculated at (a) 50 K, (b) 70 K, (c) 100 K, (d) 200, and (e) 300 K, demonstrating a transition from an exponential trend observed for low temperatures to a non-monotonic trend for higher temperatures, indicating that the dim states became thermally accessible.

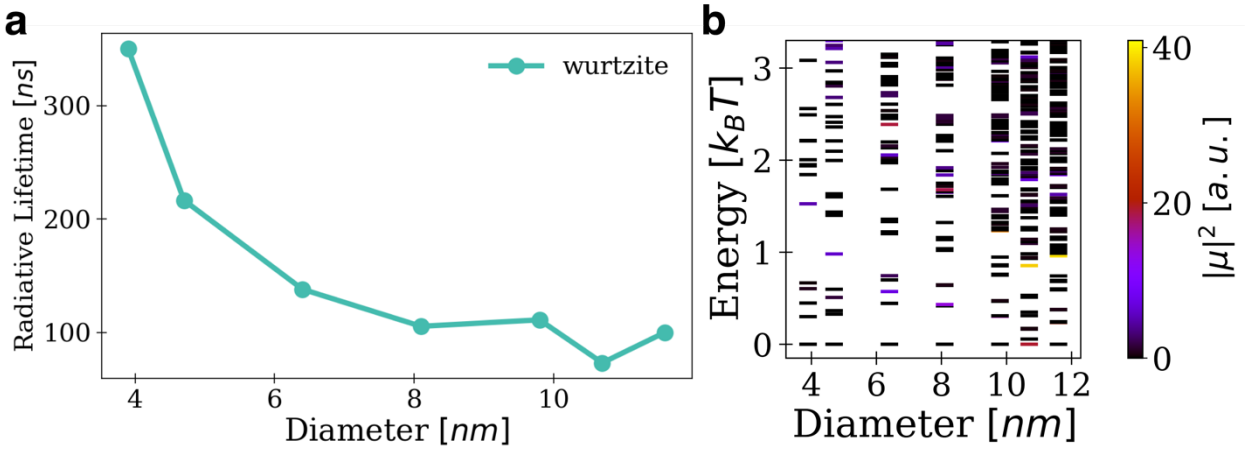


Figure D7: Size-dependent radiative lifetimes calculation of wurtzite CdSe nanocrystals. a,**b**, (**a**) calculated radiative lifetimes as a function of CdSe nanocrystal size, revealing a decreasing trend with increasing nanocrystal size due to mixing of bright states with thermally accessible dim states plotted in (**b**) for different sizes within $3\kappa_B T$. We also see the inflection point as we approach the intermediate quantum confinement regime (CdSe Bohr radius is 5.6 nm). This trend was computationally observed in CdSe nanocrystals previously[70].

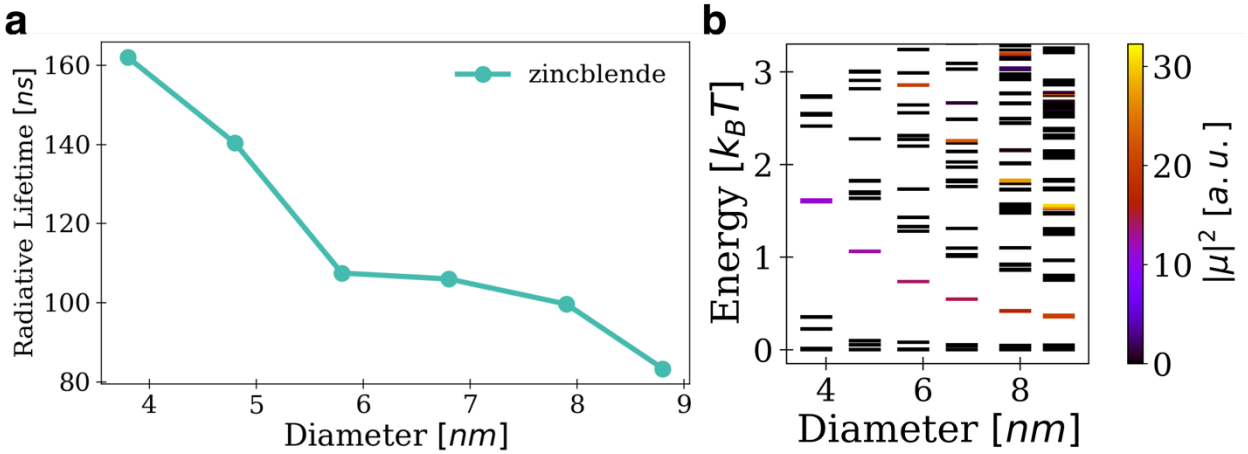


Figure D8: Size-dependent radiative lifetimes calculation of zincblende InP nanocrystals. a,**b**, (**a**) calculated radiative lifetimes as a function of InP nanocrystal size, revealing a decreasing trend with increasing nanocrystal size due to mixing of bright states with thermally accessible dim states plotted in (**b**) for different sizes within $3\kappa_B T$. Bohr radius of InP is 10 nm.

References

(1) Pringsheim, P. Zwei Bemerkungen Über Den Unterschied von Lumineszenz- Und Temperaturstrahlung. *Zeitschrift für Phys.* **1929**, *57* (11–12), 739–746.

(2) T.W. Hansch and A.L. Schawlow. Cooling Of Gases By Laser Radiation. *Opt. Commun.* **1975**, *13* (I), 68–69.

(3) Wineland, D. J.; Dehmelt, H. G. Proposed 1014 Δν < ν Laser Fluorescence Spectroscopy on Tl+ Ion Mono-Oscillator. *Bulletin of the American Physical Society*. 1975, p 637.

(4) Zhang, J.; Li, D.; Chen, R.; Xiong, Q. Laser Cooling of a Semiconductor by 40 Kelvin. *Nature* **2013**, *493* (7433), 504–508.

(5) Zhang, S.; Zhukovskyi, M.; Jankó, B.; Kuno, M. Progress in Laser Cooling Semiconductor Nanocrystals and Nanostructures. *NPG Asia Mater.* **2019**, *11* (54).

(6) Ivády, V.; Simon, T.; Maze, J. R.; Abrikosov, I. A.; Gali, A. Pressure and Temperature Dependence of the Zero-Field Splitting in the Ground State of NV Centers in Diamond: A First-Principles Study. *Phys. Rev. B* **2014**, *90* (23), 1–8.

(7) Bowman, S. R. Lasers without Internal Heat Generation. *IEEE J. Quantum Electron.* **1999**, *35* (1), 115–122.

(8) Epstein, R. I.; Buchwald, M. I.; Edwards, B. C.; Gosnellt, T. R.; Mungant, C. E. Observation of Laser-Induced Fluorescent Cooling of a Solid. *Nature* **1995**, *377* (October), 500.

(9) Melgaard, S. D.; Albrecht, A. R.; Hehlen, M. P.; Sheik-Bahae, M. Solid-State Optical Refrigeration to Sub-100 Kelvin Regime. *Sci. Rep.* **2016**, *6*, 2–7.

(10) Sheik-Bahae, M.; Epstein, R. I. Can Laser Light Cool Semiconductors? *Phys. Rev. Lett.* **2004**, *92* (24), 1–4.

(11) Ha, S. T.; Shen, C.; Zhang, J.; Xiong, Q. Laser Cooling of Organic-Inorganic Lead Halide Perovskites. *Nat. Photonics* **2016**, *10* (2), 115–121.

(12) Gauck, H.; Gfroerer, T. H.; Renn, M. J.; Cornell, E. A.; Bertness, K. A. External Radiative Quantum Efficiency of 96% from a GaAs/GaInP Heterostructure. *Appl. Phys. A Mater. Sci. Process.* **1997**, *64* (2), 143–147.

(13) Bender, D. A.; Cederberg, J. G.; Wang, C.; Sheik-Bahae, M. Development of High Quantum Efficiency GaAs/GaInP Double Heterostructures for Laser Cooling. *Appl. Phys. Lett.* **2013**, *102* (25), 252102.

(14) Morozov, Y. V.; Zhang, S.; Pant, A.; Jankó, B.; Melgaard, S. D.; Bender, D. A.; Pauzauskie, P. J.; Kuno, M. Can Lasers Really Refrigerate CdS Nanobelts? *Nature* **2019**, *570* (7762), E60–E61.

(15) Protesescu, L.; Yakunin, S.; Bodnarchuk, M. I.; Krieg, F.; Caputo, R.; Hendon, C. H.; Yang, R. X.; Walsh, A.; Kovalenko, M. V. Nanocrystals of Cesium Lead Halide Perovskites (CsPbX3, X = Cl, Br, and I): Novel Optoelectronic Materials Showing Bright Emission with Wide Color Gamut. *Nano Lett.* **2015**, *15* (6), 3692–3696.

(16) Protesescu, L.; Yakunin, S.; Bodnarchuk, M.; Krieg, F. Nanocrystals of Cesium Lead Halide Perovskites (CsPbX3, X= Cl, Br, and I): Novel Optoelectronic Materials Showing Bright Emission with Wide Color Gamut-Supporting Information. *Nano* **2015**, *2* (5 mL), 1–9.

(17) Morozov, Y. V.; Zhang, S.; Brennan, M. C.; Janko, B.; Kuno, M. Photoluminescence Up-Conversion in CsPbBr3 Nanocrystals. *ACS Energy Lett.* **2017**, *2* (10), 2514–2515.

(18) Nenon, D. P.; Pressler, K.; Kang, J.; Koscher, B. A.; Olshansky, J. H.; Osowiecki, W. T.; Koc, M. A.; Wang, L. W.; Alivisatos, A. P. Design Principles for Trap-Free CsPbX 3 Nanocrystals: Enumerating and Eliminating Surface Halide Vacancies with Softer Lewis Bases. *J. Am. Chem. Soc.* **2018**, *140* (50), 17760–17772.
(19) Cahen, D.; Kronik, L.; Hodes, G. Are Defects in Lead-Halide Perovskites Healed, Tolerated, or Both? *ACS Energy Lett.* **2021**, 4108–4114.
(20) Liu, M.; Wan, Q.; Wang, H.; Carulli, F.; Sun, X.; Zheng, W.; Kong, L.; Zhang, Q.; Zhang, C.; Zhang, Q.; Brovelli, S.; Li, L. Suppression of Temperature Quenching in Perovskite Nanocrystals for Efficient and Thermally Stable Light-Emitting Diodes. *Nat. Photonics* **2021**, *15*, 379–385.
(21) Loiudice, A.; Segura Lecina, O.; Bornet, A.; Luther, J. M.; Buonsanti, R. Ligand Locking on Quantum Dot Surfaces via a Mild Reactive Surface Treatment. *J. Am. Chem. Soc.* **2021**, *143* (33), 13418–13427.
(22) Koscher, B. A.; Swabeck, J. K.; Bronstein, N. D.; Alivisatos, A. P. Essentially Trap-Free CsPbBr3 Colloidal Nanocrystals by Postsynthetic Thiocyanate Surface Treatment. *J. Am. Chem. Soc.* **2017**, *139* (19), 6566–6569.
(23) Imran, M.; Caligiuri, V.; Wang, M.; Goldoni, L.; Prato, M.; Krahne, R.; De Trizio, L.; Manna, L. Benzoyl Halides as Alternative Precursors for the Colloidal Synthesis of Lead-Based Halide Perovskite Nanocrystals. *J. Am. Chem. Soc.* **2018**, *140* (7), 2656–2664.
(24) Würth, C.; Grabolle, M.; Pauli, J.; Spieles, M.; Resch-Genger, U. Comparison of Methods and Achievable Uncertainties for the Relative and Absolute Measurement of Photoluminescence Quantum Yields. *Anal. Chem.* **2011**, *83* (9), 3431–3439.
(25) Hanifi, D. A.; Bronstein, N. D.; Koscher, B. A.; Nett, Z.; Swabeck, J. K.; Takano, K.; Schwartzberg, A. M.; Maserati, L. Redefining Near-Unity Luminescence in Quantum Dots with Photothermal Threshold Quantum Yield. *Science (80-.).* **2019**, *363*, 1199–1202.
(26) Becker, M. A.; Vaxenburg, R.; Nedelcu, G.; Sercel, P. C.; Shabaev, A.; Mehl, M. J.; Michopoulos, J. G.; Lambrakos, S. G.; Bernstein, N.; Lyons, J. L.; Stöferle, T.; Mahrt, R. F.; Kovalenko, M. V.; Norris, D. J.; Rainò, G.; Efros, A. L. Bright Triplet Excitons in Caesium Lead Halide Perovskites. *Nature* **2018**, *553* (7687), 189–193.
(27) Miyata, K.; Meggiolaro, D.; Tuan Trinh, M.; Joshi, P. P.; Mosconi, E.; Jones, S. C.; De Angelis, F.; Zhu, X. Y. Large Polarons in Lead Halide Perovskites. *Sci. Adv.* **2017**, *3* (8), e1701217.
(28) Shi, D.; Adinolfi, V.; Comin, R.; Yuan, M.; Alarousu, E.; Buin, A.; Chen, Y.; Hoogland, S.; Rothenberger, A.; Katsiev, K.; Losovyj, Y.; Zhang, X.; Dowben, P. A.; Mohammed, O. F.; Sargent, E. H.; Bakr, O. M. Low Trap-State Density and Long Carrier Diffusion in Organolead Trihalide Perovskite Single Crystals. *Science (80-.).* **2015**, *347* (6221), 519–522.
(29) Kang, J.; Wang, L. W. High Defect Tolerance in Lead Halide Perovskite CsPbBr3. *J. Phys. Chem. Lett.* **2017**, *8* (2), 489–493.
(30) Guo, P.; Xia, Y.; Gong, J.; Cao, D. H.; Li, X.; Li, X.; Zhang, Q.; Stoumpos, C. C.; Kirschner, M. S.; Wen, H.; Prakapenka, V. B.; Ketterson, J. B.; Martinson, A. B. F.; Xu, T.; Kanatzidis, M. G.; Chan, M. K. Y.; Schaller, R. D. Direct Observation of Bandgap Oscillations Induced by Optical Phonons in Hybrid Lead Iodide Perovskites. *Adv. Funct. Mater.* **2020**, *30* (22), 1907982.
(31) Quan, L. N.; Park, Y.; Guo, P.; Gao, M.; Jin, J.; Huang, J.; Copper, J. K.; Schwartzberg,

A.; Schaller, R.; Limmer, D. T.; Yang, P. Vibrational Relaxation Dynamics in Layered Perovskite Quantum Wells. *PNAS* **2021**, *118* (25), e2104425118.
(32) Wu, B.; Wang, A.; Fu, J.; Zhang, Y.; Yang, C.; Gong, Y.; Jiang, C.; Long, M.; Zhou, G.; Yue, S.; Ma, W.; Liu, X. Uncovering the Mechanisms of Efficient Upconversion in Two-Dimensional Perovskites with Anti-Stokes Shift up to 220 MeV. *Sci. Adv.* **2023**, *9* (39), eadi9347.
(33) Zhao, W.; Qin, Z.; Zhang, C.; Wang, G.; Dai, X.; Xiao, M. Coherent Exciton-Phonon Coupling in Perovskite Semiconductor Nanocrystals Studied by Two-Dimensional Electronic Spectroscopy. *Appl. Phys. Lett.* **2019**, *115* (24).
(34) Quarti, C.; Grancini, G.; Mosconi, E.; Bruno, P.; Ball, J. M.; Lee, M. M.; Snaith, H. J.; Petrozza, A.; Angelis, F. De. The Raman Spectrum of the CH3NH3PbI3 Hybrid Perovskite: Interplay of Theory and Experiment. *J. Phys. Chem. Lett.* **2014**, *5* (2), 279–284.
(35) Cha, J. H.; Han, J. H.; Yin, W.; Park, C.; Park, Y.; Ahn, T. K.; Cho, J. H.; Jung, D. Y. Photoresponse of CsPbBr3 and Cs4PbBr6 Perovskite Single Crystals. *J. Phys. Chem. Lett.* **2017**, *8* (3), 565–570.
(36) Roman, B. J.; Sheldon, M. The Role of Mid-Gap States in All-Inorganic CsPbBr3 Nanoparticle One Photon up-Conversion. *Chem. Commun.* **2018**, *54* (50), 6851–6854.
(37) Dutta, A.; Behera, R. K.; Pal, P.; Baitalik, S.; Pradhan, N. Near-Unity Photoluminescence Quantum Efficiency for All CsPbX 3 (X=Cl, Br, and I) Perovskite Nanocrystals: A Generic Synthesis Approach. *Angew. Chemie - Int. Ed.* **2019**, *58* (17), 5552–5556.
(38) Momma, K.; Izumi, F. VESTA 3 for Three-Dimensional Visualization of Crystal, Volumetric and Morphology Data. *J. Appl. Crystallogr.* **2011**, *44* (6), 1272–1276.
(39) Zhao, W.; Qin, Z.; Zhang, C.; Wang, G.; Dai, X.; Xiao, M. Coherent Exciton-Phonon Coupling in Perovskite Semiconductor Nanocrystals Studied by Two-Dimensional Electronic Spectroscopy. *Appl. Phys. Lett.* **2019**, *115* (24), 243101.
(40) Ma, X.; Shen, P.; Wang, Y. N.; Pan, F.; Chen, G.; Xu, S.; Ye, H. Local Phonon Modes Concerned with the Self-Trapped Exciton State in CsPbBr3Nanocrystals. *J. Phys. Chem. C* **2020**, *124* (49), 27130–27135.
(41) Xue, J.; Yang, D.; Cai, B.; Xu, X.; Wang, J.; Ma, H.; Yu, X.; Yuan, G.; Zou, Y.; Song, J.; Zeng, H. Photon-Induced Reversible Phase Transition in CsPbBr 3 Perovskite. *Adv. Funct. Mater.* **2019**, *29* (13), 1807922.
(42) Wani, T. A.; Shamsi, J.; Bai, X.; Arora, N.; Dar, M. I. Advances in All-Inorganic Perovskite Nanocrystal-Based White Light Emitting Devices. *ACS Omega* **2023**, *8,* 17337−17349.
(43) Kumar, V.; Nagal, V.; Kumar, R.; Srivastava, S.; Gupta, B. K.; Kumar, M.; Hafiz, A. K.; Singh, K. Influence of the Rate of Radiation Energy on the Charge-Carrier Kinetics Application of All-Inorganic CsPbBr3perovskite Nanocrystals. *RSC Adv.* **2020**, *10* (57), 34651–34657.
(44) Kambhampati, P. Hot Exciton Relaxation Dynamics in Semiconductor Quantum Dots: Radiationless Transitions on the Nanoscale. *J. Phys. Chem. C* **2011**, *115* (45), 22089–22109.
(45) Yu, B.; Zhang, C.; Chen, L.; Qin, Z.; Huang, X.; Wang, X.; Xiao, M. Ultrafast Dynamics of Photoexcited Carriers in Perovskite Semiconductor Nanocrystals. *Nanophotonics* **2021**, *10* (8), 1943–1965.
(46) Aneesh, J.; Swarnkar, A.; Kumar Ravi, V.; Sharma, R.; Nag, A.; Adarsh, K. V. Ultrafast

Exciton Dynamics in Colloidal CsPbBr3 Perovskite Nanocrystals: Biexciton Effect and Auger Recombination. *J. Phys. Chem. C* **2017**, *121* (8), 4734–4739.
(47) Rossi, D.; Wang, H.; Dong, Y.; Qiao, T.; Qian, X.; Son, D. H. Light-Induced Activation of Forbidden Exciton Transition in Strongly Confined Perovskite Quantum Dots. *ACS Nano* **2018**, *12* (12), 12436–12443.
(48) Seiler, H.; Zahn, D.; Taylor, V. C. A.; Bodnarchuk, M. I.; Windsor, Y. W.; Kovalenko, M. V.; Ernstorfer, R. Direct Observation of Ultrafast Lattice Distortions during Exciton-Polaron Formation in Lead Halide Perovskite Nanocrystals. *ACS Nano* **2023**, *17* (3), 1979–1988.
(49) Huang, H.; Bodnarchuk, M. I.; Kershaw, S. V.; Kovalenko, M. V.; Rogach, A. L. Lead Halide Perovskite Nanocrystals in the Research Spotlight: Stability and Defect Tolerance. *ACS Energy Lett.* **2017**, *2* (9), 2071–2083.
(50) Manser, J. S.; Christians, J. A.; Kamat, P. V. Intriguing Optoelectronic Properties of Metal Halide Perovskites. *Chem. Rev.* **2016**, *116* (21), 12956–13008.
(51) Kovalenko, M. V.; Protesescu, L.; Bodnarchuk, M. I. Properties and Potential Optoelectronic Applications of Lead Halide Perovskite Nanocrystals. *Science (80-.).* **2017**, *358* (6364), 745–750.
(52) Han, Q.; Wu, W.; Liu, W.; Yang, Q.; Yang, Y. Two-Photon Absorption and Upconversion Luminescence of Colloidal CsPbX3 Quantum Dots. *Opt. Mater. (Amst).* **2018**, *75*, 880–886.
(53) Ye, S.; Yu, M.; Zhao, M.; Song, J.; Qu, J. Low Temperature Synthesis of High-Quality All-Inorganic Cesium Lead Halide Perovskite Nanocrystals in Open Air and Their Upconversion Luminescence. *J. Alloys Compd.* **2018**, *730*, 62–70.
(54) Zhang, Z.; Ghonge, S.; Ding, Y.; Zhang, S.; Berciu, M.; Schaller, R. D.; Jankó, B.; Kuno, M. Resonant Multiple-Phonon Absorption Causes Efficient Anti-Stokes Photoluminescence in CsPbBr3 Nanocrystals. *ACS Nano* **2024**, *18*, 6438−6444.
(55) Calistru, D. M.; Mihut, L.; Lefrant, S.; Baltog, I. Identification of the Symmetry of Phonon Modes in CsPbCl3 in Phase IV by Raman and Resonance-Raman Scattering. *J. Appl. Phys.* **1997**, *82* (11), 5391–5395.
(56) Liao, M.; Shan, B.; Li, M. In Situ Raman Spectroscopic Studies of Thermal Stability of All-Inorganic Cesium Lead Halide (CsPbX 3 , X = Cl, Br, I) Perovskite Nanocrystals. *J. Phys. Chem. Lett.* **2019**, *10* (6), 1217–1225.
(57) Satta, J.; Melis, C.; Carbonaro, C. M.; Pinna, A.; Salado, M.; Salazar, D.; Ricci, P. C. Raman Spectra and Vibrational Analysis of CsPbI3: A Fast and Reliable Technique to Identify Lead Halide Perovskite Polymorphs. *J. Mater.* **2021**, *7* (1), 127–135.
(58) Seiler, H.; Palato, S.; Sonnichsen, C.; Baker, H.; Socie, E.; Strandell, D. P.; Kambhampati, P. Two-Dimensional Electronic Spectroscopy Reveals Liquid-like Lineshape Dynamics in CsPbI3 Perovskite Nanocrystals. *Nat. Commun.* **2019**, *10* (1).
(59) Abbas, A. S.; Vargo, E.; Jamali, V.; Ercius, P.; Pieters, P. F.; Brinn, R. M.; Ben-Moshe, A.; Cho, M. G.; Xu, T.; Alivisatos, A. P. Observation of an Orientational Glass in a Superlattice of Elliptically-Faceted CdSe Nanocrystals. *ACS Nano* **2022**, *16* (6), 9339–9347.
(60) Ashner, M. N.; Shulenberger, K. E.; Krieg, F.; Powers, E. R.; Kovalenko, M. V.; Bawendi, M. G.; Tisdale, W. A. Size-Dependent Biexciton Spectrum in Cspbbr3 Perovskite Nanocrystals. *ACS Energy Lett.* **2019**, *4* (11), 2639–2645.
(61) Kambhampati, P. Unraveling the Structure and Dynamics of Excitons in Semiconductor

Quantum Dots. *Acc. Chem. Res.* **2011**, *44* (1), 1–13.
(62) Dey, A.; Ye, J.; De, A.; Debroye, E.; Ha, S. K.; Bladt, E.; Kshirsagar, A. S.; Wang, Z.; Yin, J.; Wang, Y.; Quan, L. N.; Yan, F.; Gao, M.; Li, X.; Shamsi, J.; Debnath, T.; Cao, M.; Scheel, M. A.; Kumar, S.; Steele, J. A.; Gerhard, M.; Chouhan, L.; Xu, K.; Wu, X. G.; Li, Y.; Zhang, Y.; Dutta, A.; Han, C.; Vincon, I.; Rogach, A. L.; Nag, A.; Samanta, A.; Korgel, B. A.; Shih, C. J.; Gamelin, D. R.; Son, D. H.; Zeng, H.; Zhong, H.; Sun, H.; Demir, H. V.; Scheblykin, I. G.; Mora-Seró, I.; Stolarczyk, J. K.; Zhang, J. Z.; Feldmann, J.; Hofkens, J.; Luther, J. M.; Pérez-Prieto, J.; Li, L.; Manna, L.; Bodnarchuk, M. I.; Kovalenko, M. V.; Roeffaers, M. B. J.; Pradhan, N.; Mohammed, O. F.; Bakr, O. M.; Yang, P.; Müller-Buschbaum, P.; Kamat, P. V.; Bao, Q.; Zhang, Q.; Krahne, R.; Galian, R. E.; Stranks, S. D.; Bals, S.; Biju, V.; Tisdale, W. A.; Yan, Y.; Hoye, R. L. Z.; Polavarapu, L. State of the Art and Prospects for Halide Perovskite Nanocrystals. *ACS Nano* **2021**, *15* (7), 10775–10981.
(63) Akkerman, Q. A.; Rainò, G.; Kovalenko, M. V.; Manna, L. Genesis, Challenges and Opportunities for Colloidal Lead Halide Perovskite Nanocrystals. *Nat. Mater.* **2018**, *17* (May), 1–12.
(64) Kovalenko, M. V; Protesescu, L.; Bodnarchuk, M. I. Properties and Potential Optoelectronic Applications of Lead Halide Perovskite Nanocrystals. **2017**, *750* (November), 745–750.
(65) Ye, S.; Yu, M.; Zhao, M.; Song, J.; Qu, J. Low Temperature Synthesis of High-Quality All-Inorganic Cesium Lead Halide Perovskite Nanocrystals in Open Air and Their Upconversion Luminescence. *J. Alloys Compd.* **2018**, *730*, 62–70.
(66) A. P. Alivisatos. Semiconductor Clusters, Nanocrystals, and Quantum Dots. *Science (80-.).* **1996**, *271* (5251), 933–937.
(67) Murray, C. B.; Norris, D. J.; Bawendi, M. G. Synthesis and Characterization of Nearly Monodisperse CdE (E = S, Se, Te) Semiconductor Nanocrystallites. *J. Am. Chem. Soc.* **1993**, *115* (19), 8706–8715.
(68) Huang, H.; Polavarapu, L.; Sichert, J. A.; Susha, A. S.; Urban, A. S.; Rogach, A. L. Colloidal Lead Halide Perovskite Nanocrystals: Synthesis, Optical Properties and Applications. *NPG Asia Mater.* **2016**, *8* (11), e328.
(69) Makarov, N. S.; Guo, S.; Isaienko, O.; Liu, W.; Robel, I.; Klimov, V. I. Spectral and Dynamical Properties of Single Excitons, Biexcitons, and Trions in Cesium-Lead-Halide Perovskite Quantum Dots. *Nano Lett.* **2016**, *16* (4), 2349–2362.
(70) Ji, Z.; Song, Z. Exciton Radiative Lifetime in CdSe Quantum Dots. *J. Semicond.* **2023**, *44* (3).
(71) Hendrik Utzat, Weiwei Sun, Alexander E. K. Kaplan, Franziska Krieg, Matthias Ginterseder, Boris Spokoyny, Nathan D. Klein, Katherine E. Shulenberger, Collin F. Perkinson, Maksym V. Kovalenko, M. G. B. Coherent Single-Photon Emission from Colloidal Lead Halide Perovskite Quantum Dots. *Science (80-.).* **2019**, *363*, 1068–1072.
(72) Zhu, C.; Boehme, S. C.; Feld, L. G.; Moskalenko, A.; Dirin, D. N.; Mahrt, R. F.; Stöferle, T.; Bodnarchuk, M. I.; Efros, A. L.; Sercel, P. C.; Kovalenko, M. V.; Rainò, G. Single-Photon Superradiance in Individual Caesium Lead Halide Quantum Dots. *Nature* **2024**.
(73) Krieg, F.; Sercel, P. C.; Burian, M.; Andrusiv, H.; Bodnarchuk, M. I.; Stöferle, T.; Mahrt, R. F.; Naumenko, D.; Amenitsch, H.; Rainò, G.; Kovalenko, M. V. Monodisperse Long-Chain Sulfobetaine-Capped CsPbBr3Nanocrystals and Their Superfluorescent Assemblies. *ACS Cent. Sci.* **2021**, *7* (1), 135–144.

(74) Brennan, M. C.; Kuno, M.; Rouvimov, S. Crystal Structure of Individual CsPbBr 3 Perovskite Nanocubes. *Inorg. Chem.* **2019**, *58* (2), 1555–1560.
(75) Beimborn, J. C.; Walther, L. R.; Wilson, K. D.; Weber, J. M. Size-Dependent Pressure-Response of the Photoluminescence of CsPbBr3 Nanocrystals. *J. Phys. Chem. Lett.* **2020**, *11* (5), 1975–1980.
(76) Cottingham, P.; Brutchey, R. L. On the Crystal Structure of Colloidally Prepared CsPbBr3 Quantum Dots. *Chem. Commun.* **2016**, *52* (30), 5246–5249.
(77) Yang, R. X.; Tan, L. Z. Understanding Size Dependence of Phase Stability and Band Gap in CsPbI3 Perovskite Nanocrystals. *J. Chem. Phys.* **2020**, *152* (3).
(78) Zhao, Q.; Hazarika, A.; Schelhas, L. T.; Liu, J.; Gaulding, E. A.; Li, G.; Zhang, M.; Toney, M. F.; Sercel, P. C.; Luther, J. M. Size-Dependent Lattice Structure and Confinement Properties in CsPbI3 Perovskite Nanocrystals: Negative Surface Energy for Stabilization. *ACS Energy Lett.* **2020**, *5* (1), 238–247.
(79) Donegá, C. D. M.; Koole, R. Size Dependence of the Spontaneous Emission Rate and Absorption Cross Section of CdSe and CdTe Quantum Dots. *J. Phys. Chem. C* **2009**, *113* (16), 6511–6520.
(80) Califano, M.; Franceschetti, A.; Zunger, A. Temperature Dependence of Excitonic Radiative Decay in CdSe Quantum Dots: The Role of Surface Hole Traps. *Nano Lett.* **2005**, *5* (12), 2360–2364.
(81) Leistikow, M. D.; Johansen, J.; Kettelarij, A. J.; Lodahl, P.; Vos, W. L. Size-Dependent Oscillator Strength and Quantum Efficiency of CdSe Quantum Dots Controlled via the Local Density of States. *Phys. Rev. B - Condens. Matter Mater. Phys.* **2009**, *79* (4), 1–9.
(82) Brennan, M. C.; Herr, J. E.; Nguyen-Beck, T. S.; Zinna, J.; Draguta, S.; Rouvimov, S.; Parkhill, J.; Kuno, M. Origin of the Size-Dependent Stokes Shift in CsPbBr3 Perovskite Nanocrystals. *J. Am. Chem. Soc.* **2017**, *139* (35), 12201–12208.
(83) Jasrasaria, D.; Rabani, E. Interplay of Surface and Interior Modes in Exciton-Phonon Coupling at the Nanoscale. *Nano Lett.* **2021**, *21* (20), 8741–8748.
(84) Rainò, G.; Yazdani, N.; Boehme, S. C.; Kober-Czerny, M.; Zhu, C.; Krieg, F.; Rossell, M. D.; Erni, R.; Wood, V.; Infante, I.; Kovalenko, M. V. Ultra-Narrow Room-Temperature Emission from Single CsPbBr3 Perovskite Quantum Dots. *Nat. Commun.* **2022**, *13* (1), 2587.
(85) Lin, K.; Jasrasaria, D.; Yoo, J. J.; Bawendi, M.; Utzat, H.; Rabani, E. Theory of Photoluminescence Spectral Line Shapes of Semiconductor Nanocrystals. *J. Phys. Chem. Lett.* **2023**, *14* (32), 7241–7248.
(86) Bischak, C. G.; Lai, M.; Fan, Z.; Lu, D.; David, P.; Dong, D.; Chen, H.; Etman, A. S.; Lei, T.; Sun, J.; Grünwald, M.; Limmer, D. T.; Yang, P.; Ginsberg, N. S. Liquid-like Interfaces Mediate Structural Phase Transitions in Lead Halide Perovskites. *Matter* **2020**, *3* (2), 534–545.
(87) Weinberg, D.; Park, Y.; Limmer, D. T.; Rabani, E. Size-Dependent Lattice Symmetry Breaking Determines the Exciton Fine Structure of Perovskite Nanocrystals. *Nano Lett.* **2023**, *23* (11), 4997–5003.
(88) Yang, Z.; Surrente, A.; Galkowski, K.; Miyata, A.; Portugall, O.; Sutton, R. J.; Haghighirad, A. A.; Snaith, H. J.; Maude, D. K.; Plochocka, P.; Nicholas, R. J. Impact of the Halide Cage on the Electronic Properties of Fully Inorganic Cesium Lead Halide Perovskites. *ACS Energy Lett.* **2017**, *2* (7), 1621–1627.
(89) Roman, B. J.; Villegas, N. M.; Lytle, K.; Sheldon, M. Optically Cooling Cesium Lead

Tribromide Nanocrystals. *Nano Lett.* **2020**, *20* (12), 8874–8879.
(90) Zhang, J.; Li, D.; Xiong, Q. Reply to: Can Lasers Really Refrigerate CdS Nanobelts? *Nature* **2019**, *570* (7762), E62–E64.
(91) Kanjanaboos, P.; Lin, X. M.; Sader, J. E.; Rupich, S. M.; Jaeger, H. M.; Guest, J. R. Self-Assembled Nanoparticle Drumhead Resonators. *Nano Lett.* **2013**, *13* (5), 2158–2162.
(92) Jain, A.; Ong, S. P.; Hautier, G.; Chen, W.; Richards, W. D.; Dacek, S.; Cholia, S.; Gunter, D.; Skinner, D.; Ceder, G.; Persson, K. A. Commentary: The Materials Project: A Materials Genome Approach to Accelerating Materials Innovation. *APL Mater.* **2013**, *1* (011002), 1–11.